

This item was submitted to [Loughborough's Research Repository](#) by the author.  
Items in Figshare are protected by copyright, with all rights reserved, unless otherwise indicated.

## Mathematical modelling of droplets and bubbles on surfaces

PLEASE CITE THE PUBLISHED VERSION

PUBLISHER

Loughborough University

LICENCE

CC BY-NC-ND 4.0

REPOSITORY RECORD

Yin, Han. 2020. "Mathematical Modelling of Droplets and Bubbles on Surfaces". Loughborough University.  
<https://doi.org/10.26174/thesis.lboro.12129231.v1>.

# Mathematical Modelling of Droplets and Bubbles on Surfaces

Hanyu Yin

Submitted in partial fulfilment of the requirements for the award of Doctor of  
Philosophy of Loughborough University

August 2019

©Hanyu Yin 2019

### **Certificate of Originality**

This is to certify that I am responsible for the work submitted in this thesis, that the original work is my own except as specified in acknowledgements or in footnotes, and that neither the thesis nor the original work therein has been submitted to this or any other institution for a degree.

## **Abstract**

In this thesis we focus on calculating the shape of small bubbles and droplets near surfaces, in regimes where intermolecular forces are significant. In the first part of this thesis we focus on vapour nanobubbles where we use classical density functional theory (DFT) to determine the interfacial free energy (the binding potential) of simple model fluids in contact with a planar surface. This is done by calculating sequences of constrained density profiles for varying amounts of vapour adsorbed between the wall and the bulk liquid. This allows us to determine multi-scale properties of fluids at interfaces, and thereby determine the structure and the thermodynamics of vapour adsorption at solvophobic interfaces and how these depend on the microscopic properties of the fluid. We then use the binding potentials obtained as an input to the interfacial Hamiltonian (IH) model and study the properties of vapour nanobubbles at equilibrium.

In the second part of this thesis, we focus on liquids at interfaces forming droplets and in particular on the systems where there are strong packing and molecular layering effects in the liquid near the wall. These phenomena leads to oscillatory binding potentials. We discuss the influence of the layering on the spreading behaviour of liquid drops and the shape of steady drops. In order to describe the dynamic behaviour, we use the thin-film equation which is derived from the Navier-Stokes and continuity equation for an incompressible fluid. In addition, we developed a modified thin-film equation that incorporates both the effects of surface diffusion and advective flow over the surface.

*To my family:*

*Mum, Dad, Grandpa and Hanzhe.*

## Acknowledgement

First, and foremost, I would like to express my deepest gratitude to my amazing supervisors, Professor Andrew Archer and Dr David Sibley, for all their remarkable patience, unfailing support and continuous guidance throughout the last three years. There are not enough genuine words, in which I can describe my appreciation. I have been extremely fortunate to have supervisors who cared so much about my work, my life and believed in my ability along this journey. Thank you, Andy for taking the confused and frightened me as a student. Your enthusiasm and deep approach about science, has motivated me and kept me going, even in the moments when I doubted myself. Thank you David for always responding to my questions so promptly, your valuable insight and expertise helped me immeasurably in the development of the thesis as it now stands.

I would also like to take this great opportunity to thank all the friends that I have met at Loughborough, for sharing their smiles and making life here a lot of fun. Jinrong, thank you for always listening to me, laughing so hard at my jokes and always saving me in my moments of desperation and stress. A special thank you goes to Yiru, for not only being a good friend, but also for helping me at the most unsociable hours, when I needed academic discussions. Wenhao and Yi, thank you for those happy nights out, wherever and whenever needed, that made my PhD studies an enjoyable experience.

Very important to me, is my awesome family. I would like to thank my Mom, Dad and brother. From long phone calls to FaceTime sessions, without your unconditional love, unwavering support and constant encouragement over the years, none of this would indeed be possible. To my grandfather, who is also a scientist and always had confidence in me: sorry that I could not come back home more often. I hope that I can make up for the lost time.

Lastly, but no means least, I would like to thank my caring, loving, and supportive boyfriend, Minghao Liu, who stood by my side from day one and was there for me. Always has been, and, I believe, always will be.

This thesis is based partly on the following publications:

## **Chapter 5**

H. Yin, D.N. Sibley, U. Thiele, and A. J. Archer.

*Films, layers, and droplets: The effect of near-wall fluid structure on spreading dynamics.*

Phys. Rev. E, **95**, 023104, (2017).

## **Chapter 6**

H. Yin, D.N. Sibley, and A. J. Archer.

*Binding potentials for vapour nanobubbles on surfaces using density functional theory.*

J. Phys.: Condens. Matter, **31**, 315102, (2019)

# Contents

<b>1</b>	<b>Introduction</b>	<b>1</b>
1.1	Surface tension . . . . .	3
1.2	Wetting behaviour and Young's equation . . . . .	5
1.3	Macroscopic to mesoscopic . . . . .	7
<b>2</b>	<b>Statistical Mechanics</b>	<b>13</b>
2.1	Ensembles and thermodynamics . . . . .	15
2.2	Partition function in the canonical ensemble . . . . .	19
2.3	Partition function in the grand canonical ensemble . . . . .	24
2.4	Thermodynamic foundations of classical density functional theory (DFT)	26
2.5	Particle densities . . . . .	28
2.6	Density functional theory . . . . .	33
<b>3</b>	<b>Approximations Used in Density Functional Theory</b>	<b>38</b>
3.1	Hard spheres . . . . .	38
3.2	Fundamental measure theory . . . . .	40
3.3	Mean field approximation for the attraction . . . . .	43
3.4	Bulk fluid phase diagram . . . . .	46
3.5	Fluids at interfaces . . . . .	50



3.6	Binding potential . . . . .	52
<b>4</b>	<b>Thin Film Equation</b>	<b>59</b>
<b>5</b>	<b>Binding Potentials for Bubbles Using DFT</b>	<b>65</b>
5.1	Introduction and background . . . . .	66
5.2	DFT approach to calculate $g(\Gamma)$ . . . . .	68
5.3	Model fluid . . . . .	71
5.4	External potential due to the wall . . . . .	72
5.5	Results for the binding potential . . . . .	74
5.6	Vapour nanobubble profiles . . . . .	82
5.7	Concluding remarks . . . . .	93
<b>6</b>	<b>Modelling Spreading of a Droplet</b>	<b>96</b>
6.1	Introduction . . . . .	97
6.2	The form of the binding potential . . . . .	100
6.3	Thin film equation . . . . .	105
6.4	Incorporating the effects of diffusion into the mobility . . . . .	108
6.5	Spreading on a non-zero background adsorption . . . . .	111
6.6	Spreading versus dewetting towards equilibrium . . . . .	124
6.7	Including diffusion . . . . .	128
6.8	Concluding remarks . . . . .	130
<b>7</b>	<b>Final Remarks</b>	<b>135</b>
<b>A</b>	<b>Convergence Test</b>	<b>138</b>
<b>B</b>	<b>Parameter Values for the Binding Potential Fit Functions</b>	<b>141</b>

# List of Figures

1.1	A schematic diagram of interactions acting on molecules in a liquid . . .	4
1.2	Wetting behaviours of a liquid droplet on a solid substrate . . . . .	6
1.3	Sketch of the two systems to be modelled . . . . .	11
2.1	Thermodynamic ensembles . . . . .	16
2.2	Radial distribution function $g(r)$ for a Lennard-Jones fluid using Ornstein-Zernike equation with the Percus-Yevic closure relation . . . . .	32
3.1	Yukawa pair potential . . . . .	47
3.2	Phase diagram of Yukawa fluid . . . . .	49
3.3	Equilibrium density profile calculated at liquid vapour coexistence without the presence of an external field $V_{ext}$ . . . . .	51
3.4	Schematic diagram of the two systems . . . . .	53
5.1	Density profiles and binding potential $g(\Gamma)$ for a film of vapour adsorbed at a hard wall . . . . .	70
5.2	Binding potentials $g(\Gamma)$ with varied Yukawa wall attraction strength $\beta\epsilon_w^{(Y)}$	75
5.3	Binding potentials $g(\Gamma)$ with varied LJ-like wall attraction strength $\beta\epsilon_w^{(LJ)}$	76

5.4	A comparison of the binding potentials $g(\Gamma)$ for the four different external potentials $V_{ext}^{(i)}$ with the wall potential attraction strength parameters $\beta\epsilon_w^{(i)}$ chosen so that they all have the same minimal value of $g(\Gamma_0)$ . . .	78
5.5	As for Fig. 5.4 but on log scale . . . . .	79
5.6	Binding potentials for the exponential wall potential $V_{ext}^{(E)}$ with varying $\lambda_w^{(E)}$ . . . . .	82
5.7	As for Fig. 5.6 but on log scale . . . . .	83
5.8	Equilibrium vapour nanobubble height profiles calculated from interfacial Hamiltonian (IH) model . . . . .	84
5.9	Disjoining pressure and the curvature contributions to the excess pressure as a function of position through a nanobubble, for the case where $\beta\epsilon_w^{(Y)} = 1.5$ . . . . .	86
5.10	A comparison of two equilibrium vapour nanobubble profiles on a heterogeneous surface with position dependent binding potential . . . . .	87
5.11	Free energy $F$ as a function of the vapour nanobubble volume $V$ , for a heterogeneous system . . . . .	89
5.12	The excess pressure due to the presence of the nanobubble for a range of different values of the wall attraction strength parameter $\beta\epsilon_w^{(Y)}$ . . .	92
6.1	A sketch of the molecular configurations in a cross section through the contact line region of a drop of liquid which exhibits strong layering effects. . . . .	98
6.2	Oscillatory binding potential $g_2(h)$ for liquid in contact with a hard wall as a function of the film height $h$ . . . . .	102
6.3	Oscillatory binding potential $g_3(h)$ . . . . .	103
6.4	Oscillatory binding potential $g_4(h)$ . . . . .	104

6.5	Phase plane diagram for the binding potential $g_2(h)$ . . . . .	107
6.6	Time sequence of drop profiles for a liquid drop spreading on a substrate already covered by an equilibrium background film, with binding potentials $g_1$ and $g_2$ . . . . .	113
6.7	A comparison of the final equilibrium droplets with binding potentials $g_1$ and $g_2$ . . . . .	115
6.8	The time evolution of the free energy $F$ as a droplet spreads to equilibrium with binding potentials $g_1$ and $g_2$ . . . . .	116
6.9	Equilibrium drop profiles with binding potential $g_3$ . . . . .	117
6.10	The normalised free energy difference for droplet spreading under the influence of binding potential $g_3$ . . . . .	118
6.11	A time sequence of drop profiles for a liquid drop spreading on a substrate, with binding potential $g_3$ . . . . .	119
6.12	Equilibrium droplet profiles, free energy difference and binding potentials for $g_3(h)$ with varied parameter $a$ . . . . .	120
6.13	Equilibrium drop profiles with the binding potential $g_4$ and the corresponding normalised free energy difference . . . . .	123
6.14	Equilibrium droplet profiles, the corresponding free energy difference and binding potentials with $g_4$ and varying $a$ . . . . .	125
6.15	Final equilibrium state obtained for the same volume of liquid on the surface undergoing both spreading and dewetting on a background film $h = h_0$ . . . . .	127
6.16	The free energy over time during droplet spreading with binding potential $g_2(h)$ for various values of the diffusion coefficient $\bar{\alpha}_0$ . . . . .	128

6.17	The free energy over time during droplet spreading on a totally dry substrate with binding potential $g_3(h)$ and $g_4(h)$ , for various values of the diffusion coefficient $\bar{\alpha}_0$ . . . . .	130
6.18	A time sequence of drop profiles for a liquid drop spreading on a totally dry substrate, with binding potential $g_3$ and diffusion coefficient $\bar{\alpha}_0 = 1$	131
A.1	Convergence test . . . . .	139

# Chapter 1

## Introduction

The behaviour of fluids on solid substrates is important in nature, industry and everyday life. Just think about blinking your eyes and you realise this. Many of these phenomena depend on the motion of individual atoms or molecules (particles) from which the liquid and the surface are made. For example, the movement of rain drops on windows, the sliding of oil on a Teflon coated frying pan, or a spilled drink drying to form a coffee stain on the table. Understanding the microscopic properties and arrangements of the particles, and how these give rise to the macroscopic behaviour of non-uniform fluids is not only important in different areas of physics and chemistry, but there are a wide range of applications such as in the design of microdevices and ink jet technology that depend on the behaviour of fluids on surfaces. In this thesis we demonstrate the influences of the nature of the microscopic particle interactions of fluids on the macro scale properties.

To effectively model the statics and dynamics of nanoscale droplets and bubbles, a variety of scientific disciplines need to be combined. Classical fluid mechanics, statistical mechanics and thermodynamics all play important roles in this thesis, and are

discussed individually and collectively at various points. Fluid mechanics describes the governing equations of fluid flow at the continuum mechanics scales, based, for instance, on the Navier-Stokes equations which conserve properties such as mass and momentum of a continuous fluid and are parametrised by coarse-grained transport coefficients such as surface tension and viscosity. Statistical mechanics, in contrast, explores the smallest scales at a particle level, and the theory allows us to capture particle interactions and collisions in an averaged sense. Here we use a formulation of statistical mechanics known as classical density functional theory (DFT) to compute heterogeneous nanoscale fluid density profiles. Thermodynamics provides the framework within which these two fields combine, and explores fundamental relationships between concepts such as the energy, temperature and entropy of systems in a variety of ensembles. Thermodynamics is central to our understanding of how matter organises itself. For example, it tells us that in a closed system at fixed temperature  $T$ , the equilibrium state is that which minimises the Helmholtz free energy,  $F = U - TS$ , where  $U$  is the internal energy and  $S$  is the entropy. This fundamental equation neatly showcases how the vapour and solid phases differ. At equilibrium the free energy  $F$  must be minimised, and hence at high temperature  $T$  (where the contribution  $-TS$  dominates), the entropy must be maximised and so a highly disordered gaseous state is formed in which the particles are spread out within the container. In contrast, at low temperature the contribution  $-TS$  is small and so the contribution from the internal energy  $U$  dominates. Thus the particles order based on their interactions into a solid state. The liquid state is particularly fascinating because it occurs when the two terms,  $U$  and  $-TS$  are comparable in magnitude and so in a liquid the particles gather to lower  $U$ , but remain somewhat disordered in order to make the entropy  $S$  larger. The particle interactions are fundamental in giving rise to many macroscopic phenomena such as the interfaces between the phases, determining the corresponding surface tensions, and the wetting behaviour of fluids in contact with

solid surfaces. The following subsections explore this in more depth.

## 1.1 Surface tension

The interactions between the molecules in a fluid give rise to a variety of macroscopically observed quantities, an important one being the surface tension. The existence of surface tension plays a crucial role in the behaviour of systems containing interfaces. Although commonly we may think the thickness of a surface is negligible, on the molecular level, the thickness of the interfacial region is actually significant [1].

Consider the situation where a liquid is in contact with its gas phase. Fig. 1.1 illustrates the interactions with neighbouring molecules experienced by molecules in different positions. The potential energy between pairs of molecules has a minimum as a function of the distance between the centres of the molecules. Deep in the liquid, each molecule sits at roughly this minimum energy distance from its nearest neighbours, so as to lower its total potential energy,  $U$ . One can think of each of those pair interactions as forming a ‘bond’ (equivalent to a release of energy) between neighbouring molecules. Molecule A, fully in the bulk liquid, forms bonds with molecules all around it and stays closely to the minimum energy distance from its nearest neighbours. In contrast, molecule B, which is at the surface, is not able to form as many bonds because there is nearly no attraction acting from above, which results in an inward force and also molecule B has a higher potential energy than molecule A. Molecule C in the gas phase rarely has any neighbours nearby and so its potential energy is close to zero and higher than that of A or B. Since the system tries to evolve towards a minimum free energy state, it will seek to have as few as possible higher energy molecules at the surface, thus the tendency is to reduce the surface area and the liquid surface will be forced to find its minimum area.



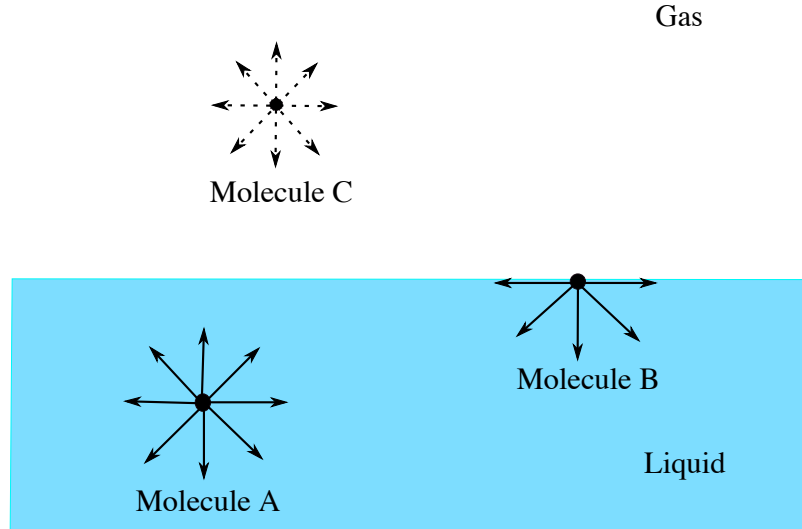


Figure 1.1: A sketch illustrating the interactions of particles in a liquid (Molecule A), a gas (Molecule C) and at the interface between the two (Molecule B). Molecule A is deep in the liquid, it forms bonds with molecules all around it and thus is staying close to the minimum energy distance from its nearest neighbours; Molecule B is at the surface and is not able to form as many bonds and has higher energy; Molecule C is in the gas and has no near neighbours thus its potential energy is roughly zero [1].

Note that since the gas and the liquid are in phase coexistence, they must have the same free energy (we say more on this in Chapter 3). The gas of course, has a larger entropy than the liquid. The molecules in the interface neither have low potential energy nor large entropy, therefore there is a free energy penalty due to the interface.

It is well known that supplying energy is necessary to create a surface. Suppose one wants to distort a liquid to increase the surface area by a certain amount, work needs to be done to pull the molecules in the liquid against the attractions of neighbouring molecules back to the surface. This work done can be represented in the following

equation

$$dW = \gamma dA, \tag{1.1.1}$$

where the surface tension  $\gamma$  is given in units of energy per unit area and is the extra energy required to increase the surface area by one unit [1] and  $dA$  is the area increased. This work done  $dW$  is stored as potential energy.

Since the liquid will evolve in order to minimise the surface area, the liquid surface will reach the minimum area eventually, resulting in the familiar fact that drops of liquid surrounded by the vapour are spherical, since a sphere has the minimum surface area compared to other shapes with the same volume. Another example is that when we separate an oil drop into smaller ones, the little droplets subsequently move back together and form the original drop to minimise the surface area.

## 1.2 Wetting behaviour and Young's equation

When a liquid drop is placed onto a solid dry substrate, it spreads on the surface to a certain extent, until equilibrium is reached and the free energy of the system is minimised. The extent of the spreading is determined by the equilibrium contact angle  $\theta$ . It is obtained from a balance of interfacial tensions, which is given by Young's equation [2]

$$\gamma_{lv} \cos \theta = \gamma_{sv} - \gamma_{sl}, \tag{1.2.1}$$

where  $\gamma_{sv}$ ,  $\gamma_{sl}$ , and  $\gamma_{lv}$  represent the interfacial tensions (excess free energy per unit area) of the solid/vapour, solid/liquid, and liquid/vapour interfaces, respectively. These are defined when three phases are in equilibrium with each other<sup>1</sup>. For large enough

---

<sup>1</sup>Note that as discussed in Ref. [3],  $\gamma_{sv}$  is distinct from  $\gamma_{so}$ , the interfacial energy of the completely dry interface.

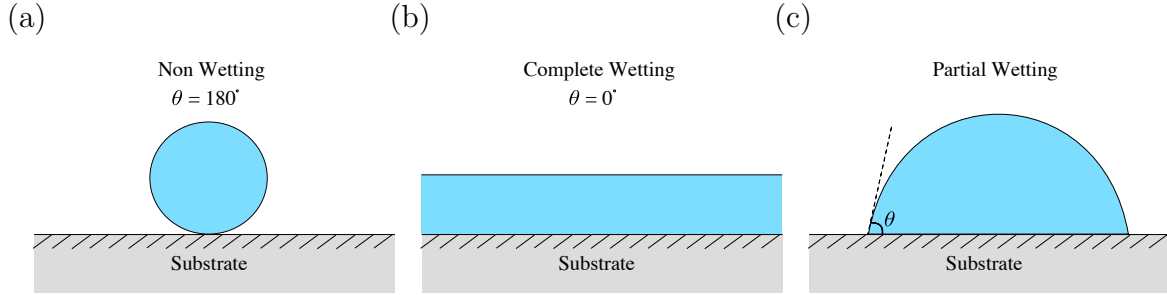


Figure 1.2: When a small droplet is in equilibrium on a horizontal substrate, the three different possible wetting regimes that may exist in any three phase system according to Young's equation. Case (a) is almost spherical and this ideal substrate can be considered even less wetting than e.g. a non-stick teflon surface. Case (b) has a macroscopically thick film; the droplet fully spreads out over the surface. This could be e.g. metal surface. Case (c) is a spherical cap with contact angle  $\theta$ . A typical example of this is water on a plastic surface.

droplets (a few hundred nm or  $\mu\text{m}$ , depending on the situation),  $\theta$  is the inner angle the liquid-vapour interface makes with the substrate.

If the three surface tension energies are known, the wetting regime of the fluid can be calculated directly. Fig. 1.2 shows the different possible wetting behaviours of a droplet on solid substrate. Complete wetting occurs when  $\theta = 0^\circ$ . The system is in equilibrium when a uniform macroscopically thick liquid layer covers the whole solid surface. Partial wetting occurs when  $0^\circ < \theta < 180^\circ$ . In this case, small droplets form a spherical cap due to the liquid volume constraint and the dominant capillary effects. Deviations from a spherical cap shape occur if the radius of the drop is larger than the capillary length  $\kappa^{-1} = \sqrt{\frac{\gamma_{lv}}{m\rho_l G}}$ , where  $\rho_l$  is the number density of liquid,  $m$  is the mass of a molecule and  $G$  is the acceleration due to gravity. Above this size, gravity can no longer be neglected. Unless the vapour pressure of the liquid is zero, at equilibrium the substrate surrounding the drop is covered by a microscopically thin film layer of

thickness  $h_0$  adsorbed on the substrate. This adsorbed layer is generally submonolayer, so the popular terminology ‘precursor film’ is potentially misleading [4, 5, 6]. For non-wetting to occur,  $\theta = 180^\circ$ .

### 1.3 Macroscopic to mesoscopic

For very small drops and for length scales below a few hundred nm, the wetting behaviour is determined by the molecular interactions, e.g. the van der Waals and electrostatic forces. For such droplets these interactions become important and can extend across the thickness of the film and contribute extra forces that determine the shape of the drop and how it spreads. For a film of thickness  $h$  in contact with a solid wall, surface tension energies alone are not sufficient to describe the free energy of the system anymore. Particle interactions lead to an effective interaction between the two interfaces, i.e. there is an additional contribution to the free energy  $g(h)$ , often referred to as the binding potential, which must be included. It can be expressed in terms of the Derjaguin, or disjoining (or conjoining) pressure [7, 8],

$$\Pi(h) = -\frac{\partial g(h)}{\partial h}. \quad (1.3.1)$$

The interaction between the two interfaces can also be discussed in terms of this pressure. The total excess free energy per unit area of a system with a film of liquid with uniform thickness  $h$  is:

$$\frac{\Delta F}{A} = \gamma_{lv} + \gamma_{sl} + g(h), \quad (1.3.2)$$

where  $A$  is the area covered by the film. Thus,  $g(h)$  gives the contribution to the free energy from the interactions between two interfaces, and has the limiting values

$g(\infty) = 0$  and [1]

$$g(h_0) = \gamma_{sv} - (\gamma_{lv} + \gamma_{sl}), \quad (1.3.3)$$

where  $h_0$  is the height of the flat film at equilibrium.

The disjoining pressure is an important thermodynamic function and it plays a key role in studying thin films. It is a function of film height  $h$  and is responsible for the equilibrium thickness of wetting films. It gives the difference between the pressure  $P(h)$  in a thin liquid layer and  $P(\infty)$ , the pressure when the liquid film is macroscopically thick. Thus,

$$\Pi(h) = P(h) - P(\infty). \quad (1.3.4)$$

In general, three main contributions to the disjoining pressure  $\Pi$  are identified [9, 10, 11, 12]:

- (i) a long-range van der Waals contribution due to the interaction between dipoles (either permanent or induced) of the liquid molecules and the substrate molecules. It can be either attractive or repulsive;
- (ii) long-range electrostatic forces, from charge double layers overlapping during thinning. The like charged surfaces of the film repel each other;
- (iii) short-range steric forces, which stem from the repulsive interactions between molecules when they are pushed close together.

The van der Waals force is characterised by the Hamaker constant  $H$  [10, 11, 12], originating from the attractive (London) potential between individual pairs of molecules which at large  $r$  is often modelled as proportional to  $\sim r^{-6}$ , where  $r$  is the distance between molecules. It gives the longest range contribution to  $\Pi$ . The leading order term that dominates for large  $h$  is [12]

$$\Pi \approx -\frac{H}{6\pi h^3}, \quad (1.3.5)$$

which is obtained by summing (averaging) over all the interactions between the fluid and the particles forming the wall [13]. If  $H > 0$ , it means the two interfaces attract each other and the film pinches; on the other hand if  $H < 0$ , the two interfaces repel each other. Thus, the van der Waals force often determines the wetting behaviour. In the case  $H > 0$ , one must include additional terms in  $\Pi$ .

A commonly used expression that describes a partially wetting situation and allows for a stable precursor film is

$$\Pi_1(h) = \frac{5a}{h^6} - \frac{2b}{h^3}, \quad (1.3.6)$$

where  $b = H/12\pi$  and  $a$  is a positive constant. The corresponding binding potential is

$$g_1(h) = \frac{a}{h^5} - \frac{b}{h^2}. \quad (1.3.7)$$

The positive term represents the short range repulsive forces, while the second term describes the longer range van der Waals forces contribution. This form has been frequently used in thin-film models, e.g., in Refs. [14, 15, 16]. However, as can be deduced from considering the  $h \rightarrow 0$  limit, where  $g_1(h)$  is infinite, it is clear that this expression is really only valid for large film thickness, since we expect a finite value of  $g(h = 0)$ . Similarly, for model systems with only short range forces one finds that for large  $h$  the binding potential decays exponentially,

$$g(h) \sim a_1 \exp(-h/\xi) + a_2 \exp(-2h/\xi) + \dots, \quad (1.3.8)$$

where  $\xi$  is the bulk correlation length (a measure of how quickly the correlations between particles decays with distance) in the liquid phase wetting the wall and the coefficients  $a_i$  depend on the temperature [17, 18] as well as on the form of the interactions. The progress made in Refs. [4, 5, 6] was to develop a DFT based method for calculating

$g(h)$ , or strictly speaking  $g(\Gamma)$ , where  $\Gamma$  is the adsorption, that is valid over the whole range of values of  $h$ .

The physics of vapour bubbles on surfaces shares many similarities with the more commonly studied system of liquid droplets on a surface, surrounded by the vapour (see Fig. 1.3). In both cases, the two main contributions to the excess free energy  $F[h]$  of the system due to the interface are the binding potential contribution (i.e. due to the molecular interactions), and the surface tension contribution (proportional to the area of the liquid-vapour interface), which gives [17, 19, 1]

$$F_{\text{IH}}[h] = \iint \left[ g(h) + \gamma_{lv} \sqrt{1 + (\nabla h)^2} \right] dx dy, \quad (1.3.9)$$

where  $h(x, y)$  is the thickness of the fluid film at some point  $(x, y)$  above the substrate as shown in Fig. 1.3. This free energy is often termed an interfacial Hamiltonian (IH). Note that in Eq. (1.3.9) we have omitted terms independent of  $h$ .

This thesis is structured as follows: In the next chapter, we present some necessary background theory on statistical mechanics and the relevant interfacial thermodynamics for studying fluids at the microscopic level. Following this, in Chapter 3, we introduce classical density functional theory (DFT), which is a statistical mechanical theory and is used to calculate the binding potential  $g(\Gamma)$ . Then, in Chapter 4, the mathematical (fluid mechanics) description of steady and spreading drops or bubbles is formulated.

The following two chapters then present the principal original work contained in this thesis, each describing a different situation relating to fluids at interfaces. Even though a large number of studies with calculations on liquids in contact with a solid surface have been done using DFT [20], much less has been published for a vapour film surrounded by a liquid, with the vapour in contact with the wall. In Chapter 5, we develop a model for stable nanobubbles at equilibrium, that is based on calculating the

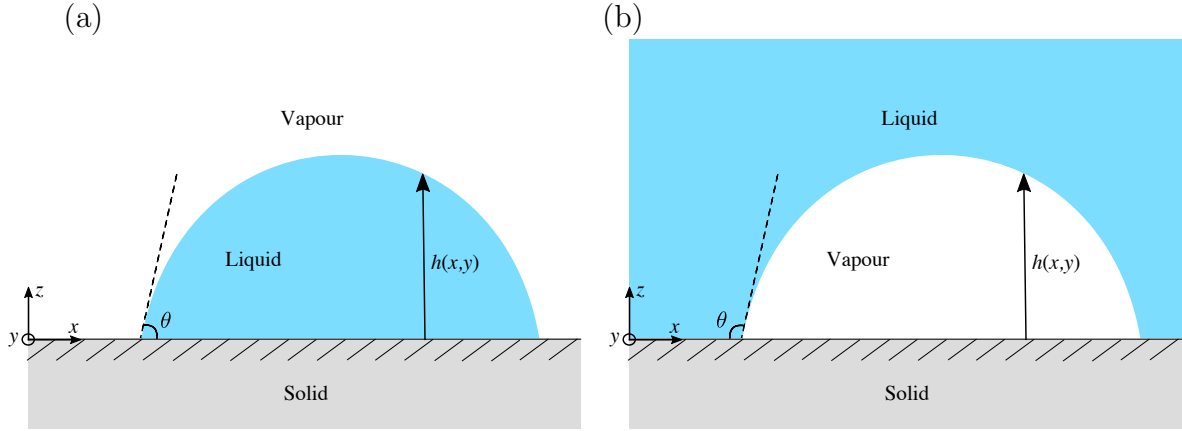


Figure 1.3: (a) Sketch of a liquid drop with height profile  $z = h(x, y)$ , surrounded by vapour, on top of a solid planar wall that exerts an external potential  $V_{ext}(z)$  on the fluid. The coordinate direction  $z$  is perpendicular to the solid surface and the  $x$ - and  $y$ -axes are parallel to the surface. The contact angle of the liquid with the wall is  $\theta$ . (b) Sketch of a vapour bubble in contact with the solid wall.

binding potential  $g(h)$  as a function of thickness  $h$  (including in the small  $h$  regime) using DFT. We do this for various different wall potentials to investigate how the decay form of these (as we move away from the wall) influences the decay form of the binding potential, that can then be used as an input into the interfacial Hamiltonian (1.3.9) model, in order to determine vapour nanobubbles height profiles and their free energies. A sketch of the system of interest here is shown in Fig. 1.3(b). It presents a cross section through a nanometre scaled vapour bubble adhered to the solid wall. A vapour layer is in contact with the solid surface which we define to be at  $z = 0$ .

In Chapter 6, building on the previous work of Hughes et al. in 2015 [4, 5, 6], who considered the wall-liquid-vapour system and computed using DFT an oscillatory binding potential in a particular case of a fluid close to the freezing temperature, here we determine the influence of such an oscillatory binding potential on the shape of steady



drops and also the dynamics of drop spreading. A sketch of a typical droplet profile that would be obtained using the IH model is displayed in Fig. 1.3(a). The established thin film models describe the advective motion<sup>2</sup> of the liquid over the substrate, sometimes also incorporating slip [21, 22]. However, normally, such models do not include the diffusive particle-hopping dynamics that one should expect when the adsorption is low [23, 24]. Thus, we also develop here an augmented thin-film equation that incorporates this effect, with the principal aims of this work being to (a) incorporate well-founded structural disjoining pressures into thin-film modelling, and (b) to propose and probe a model that switches between diffusion and hydrodynamics.

Finally, the conclusions which can be drawn from this thesis and the possible improvements which could be made to the model are discussed in Chapter 7.

---

<sup>2</sup>Note that here by ‘advective’ motion, we refer to classical hydrodynamic motion of the film—principally using the term to contrast with the diffusive dynamics added in Sec. 6.4

# Chapter 2

## Statistical Mechanics

The aim of statistical mechanics is to determine the collective average behaviour of a large number of interacting particles. At the microscopic level, the particles are in constant motion, but on mesoscopic and macroscopic scales they can be in a well-defined configuration, such as one observes for a drop of liquid on a surface.

We start by considering a classical fluid system that is made of  $N$  identical, spherical particles in three dimensions (3D), where each particle has mass  $m$  and velocity  $\mathbf{v}_i$ . Then the state of the particles can be characterised by the set of all the position and momenta variables

$$(\mathbf{r}^N, \mathbf{p}^N) = (\mathbf{r}_1, \mathbf{r}_2, \dots, \mathbf{r}_N, \mathbf{p}_1, \mathbf{p}_2, \dots, \mathbf{p}_N), \quad (2.0.1)$$

where  $\mathbf{r}_i = (r_x, r_y, r_z)_i$  is the position and  $\mathbf{p}_i = (p_x, p_y, p_z)_i$  is the momentum of the  $i$ th particle. Thus the system is in a  $6N$  dimensional phase space which is a space that contains all possible microstates of the system. Each microstate is defined by its value of  $(\mathbf{r}^N, \mathbf{p}^N)$ , and as time changes, the system changes from one microstate to another and can be represented by different points in the phase space. The equations of motion for these coupled particles are almost impossible to solve exactly. For example, there

are approximately  $2.5 \times 10^{25}$  gas molecules in a cubic metre of air, which means we have a total of  $1.5 \times 10^{26}$  coupled first order differential equations to solve simultaneously to find the position and momentum over time of every gas molecule. Hence, instead of solving the equations of each individual particle, we focus our interest instead on a small number of macroscopic variables such as the total energy of the system.

The total energy at any given time of such a system is given by the Hamiltonian  $\mathcal{H}$ , which consists of a sum of three terms and can be written as

$$\mathcal{H}(\mathbf{r}^N, \mathbf{p}^N) = K(\mathbf{p}^N) + \mathcal{V}(\mathbf{r}^N) + \Phi(\mathbf{r}^N), \quad (2.0.2)$$

where

$$K(\mathbf{p}^N) = \sum_{i=1}^N \frac{1}{2} m \mathbf{v}_i^2 = \sum_{i=1}^N \frac{\mathbf{p}_i^2}{2m}, \quad (2.0.3)$$

is the total kinetic energy contribution,

$$\mathcal{V}(\mathbf{r}^N) = \sum_{i=1}^N V_{ext}(\mathbf{r}_i), \quad (2.0.4)$$

is the one-body external potential energy contribution, with  $V_{ext}(\mathbf{r}_i)$  being the external potential felt by a single particle at position  $\mathbf{r}_i$ .  $\Phi(\mathbf{r}^N)$  is the contribution to the potential energy from interactions between the particles. In our work, as is common in the literature, we neglect three and higher body contributions for simplicity, hence the total potential energy is just the sum of all two body particle interactions in the system and is given as

$$\Phi(\mathbf{r}^N) = \frac{1}{2} \sum_{i=1}^N \sum_{j \neq i}^N v(\mathbf{r}_i - \mathbf{r}_j). \quad (2.0.5)$$

The ensemble average (i.e. the mean value over many realisations, or copies, of the system, see next section) of this Hamiltonian gives rise to the macroscopic thermody-

namic variable  $U$ , the total internal energy of the system at equilibrium

$$\langle \mathcal{H} \rangle = U, \quad (2.0.6)$$

where  $\langle \cdot \rangle$  denotes the ensemble average of the quantity between the angular brackets. Other thermodynamic quantities, such as pressure  $P$ , density  $\rho$  and chemical potential  $\mu$ , can all be calculated by performing an ensemble average for the system, and a principal aim is to relate the microscopic behaviour of particles to macroscopic thermodynamic quantities.

## 2.1 Ensembles and thermodynamics

In statistical mechanics and thermodynamics, a system can be classified according to whether it is an isolated, closed or an open system. To determine the average properties of a system one can perform a time average or, if the system is ergodic, one can equivalently average over an ensemble of copies of the system. A statistical ensemble is a collection of a large number of many copies of a system which are subjected to the same given macroscopic conditions, such as temperature  $T$ , volume  $V$ , pressure  $P$ , entropy  $S$ , or internal energy  $U$ , however, each copy is in a different microstate. In general there exist a huge number of microstates that are all consistent with the same macrostate.

Consider an isolated system with  $U$ ,  $V$ ,  $N$  fixed and with no work being done on it, as shown in Fig. 2.1(a). The hashed lines indicate that the system is isolated and is unable to exchange either energy or particles with its surrounding environment. By the first law of thermodynamics, which states that the change in the internal energy  $dU$  of a system has to be equal to the sum of the heat that is supplied to the system  $dQ$  and

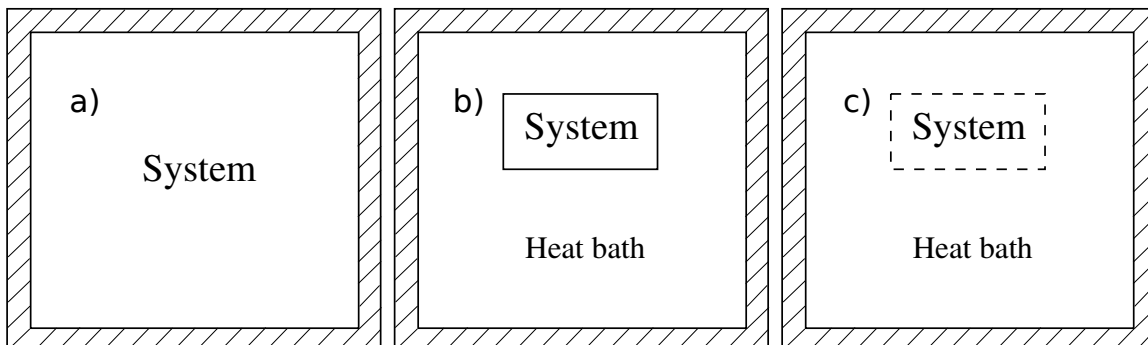


Figure 2.1: Sketches of three different thermodynamic ensembles: (a) micro-canonical ensemble where the internal energy  $U$ , volume  $V$  and the number of particles  $N$  are fixed because the system is isolated by an insulating container. (b) The canonical ensemble, where the temperature  $T$ , volume  $V$  and the number of particles  $N$  are fixed ( $T$  is fixed by the surrounding bath). (c) The grand canonical ensemble where the temperature  $T$ , volume  $V$  and the chemical potential  $\mu$  are fixed ( $T$ ,  $\mu$  are fixed by the bath).

the work being done on the system  $dW$ , therefore  $dU$  can be expressed as

$$dU = dQ + dW, \quad (2.1.1)$$

where  $dW = -PdV$ ,  $dV$  is the change in volume. We also know that heat will flow from a hotter system to a colder system. Thus, by introducing another quantity, the entropy  $S(U, V, N)$ , which is a measure of the amount of disorder within a system, we have

$$TdS \geq dQ, \quad (2.1.2)$$

where  $T$  is the temperature of the system. The inequality in the above equation becomes an equality if the changes take place sufficiently slowly and are reversible. Hence by

combining the first and second laws we can rewrite Eq. (2.1.1) as

$$dU \leq TdS - PdV. \quad (2.1.3)$$

Since for the system in Fig. 2.1(a) the volume  $V$  is fixed, then

$$dV = 0 \implies dW = 0. \quad (2.1.4)$$

Since  $U$  is also fixed, there can be no change in internal energy

$$dU = 0 \implies dQ = 0, \quad (2.1.5)$$

we therefore have

$$dS \geq 0, \quad (2.1.6)$$

which means the statistical equilibrium of this system must maximise the entropy  $S$ . In other words, the equilibrium state of the system is that with the maximum entropy. This type of system with fixed  $U$ ,  $V$  and  $N$  is called the microcanonical ensemble.

The canonical ensemble is shown in Fig. 2.1(b). It consists of a closed system with a thermal conducting boundary in contact with a heat bath which is at some fixed temperature  $T$ . By allowing exchange of heat, the system will eventually have the same temperature as the bath, however the total number of particles remains constant. In this case, we fix  $V$ ,  $N$ ,  $T$  (so in comparison to the microcanonical ensemble, we fix  $T$  but  $U$  is allowed to vary) and get

$$dW = 0 \implies dU - TdS \leq 0, \quad (2.1.7)$$

which we can write as

$$dF \leq 0, \quad (2.1.8)$$

where  $F = U - TS$  is the Helmholtz free energy. This tells us that any spontaneous change in the system leads to the Helmholtz free energy decreasing and that at equilibrium, the Helmholtz free energy  $F$  is minimised.

The canonical ensemble [Fig. 2.1(b)] can be modified by also allowing the system exchange particles with the heat bath. To describe this open system thermodynamically, we need to consider the chemical potential  $\mu$ , which is the energy required to insert one particle from the bath into the system. Thus, the change in the energy of the system when the number of particles in the system changes from  $N$  to  $N + dN$  is  $\mu dN$  and this term now needs to be added to the right hand side of Eq. (2.1.1). In this ensemble then  $T$ ,  $V$  and  $\mu$  are fixed, with internal energy  $U$  and number of particles  $N$  allowed to vary. Therefore Eq.(2.1.3) becomes

$$dU = TdS - PdV + \mu dN. \quad (2.1.9)$$

Since the volume of the system is fixed, this becomes

$$dU - TdS - \mu dN = 0, \quad (2.1.10)$$

which implies that at equilibrium

$$d\Omega = 0, \quad (2.1.11)$$

where  $d\Omega$  is the change in the grand potential  $\Omega$ , which is defined as

$$\Omega = U - TS - \mu N = F - \mu N. \quad (2.1.12)$$

Or, using the inequality in Eq.(2.1.1) we have  $d\Omega \leq 0$ . Thus in this system the grand potential is minimised at equilibrium. This system is called the grand canonical ensemble and is shown in Fig. 2.1(c). The dashed lines around the system indicate particles are free to move in and out of the system. Similar to the canonical ensemble, the equilibrium is reached when there are no more changes at constant  $T$  and  $\mu$  and the grand potential  $\Omega$  is at a minimum.

Recall that the Helmholtz free energy is given as

$$F = U - TS. \quad (2.1.13)$$

By considering the differential of this and also using Eq. (2.1.9), we obtain

$$dF = dU - SdT - TdS = -SdT - PdV + \mu dN. \quad (2.1.14)$$

Therefore, by knowing  $F = F(T, V, N)$ , many central thermodynamic variables can be found as a derivative of  $F$

$$P = - \left( \frac{\partial F}{\partial V} \right)_{T, N}, \quad \mu = \left( \frac{\partial F}{\partial N} \right)_{T, V}, \quad S = - \left( \frac{\partial F}{\partial T} \right)_{V, N}. \quad (2.1.15)$$

## 2.2 Partition function in the canonical ensemble

In a canonical ensemble, where we allow the exchange of heat and fix  $V$ ,  $N$  and  $T$ , the ensemble average of the energy can be calculated as

$$\langle \mathcal{H} \rangle = \iint \mathcal{H}(\mathbf{r}^N, \mathbf{p}^N) f(\mathbf{r}^N, \mathbf{p}^N) d\mathbf{r}^N d\mathbf{p}^N, \quad (2.2.1)$$



where  $\mathcal{H}$  is the Hamiltonian in Eq. (2.0.2) and  $\int d\mathbf{r}^N = \int d\mathbf{r}_1 \int d\mathbf{r}_2 \dots \int d\mathbf{r}_N$ ,  $\int d\mathbf{p}^N = \int d\mathbf{p}_1 \int d\mathbf{p}_2 \dots \int d\mathbf{p}_N$ . Here,  $f(\mathbf{r}^N, \mathbf{p}^N)$  is the probability density that the system is in a particular state and is normalised so that the integral of the probability density function over all of the phase space is

$$\iint f(\mathbf{r}^N, \mathbf{p}^N) d\mathbf{r}^N d\mathbf{p}^N = 1. \quad (2.2.2)$$

At equilibrium, the probability density  $f(\mathbf{r}^N, \mathbf{p}^N)$  is given by the (Gibbs) Boltzmann distribution [25]:

$$f(\mathbf{r}^N, \mathbf{p}^N) = \frac{1}{N!h^{3N}} \frac{\exp[-\mathcal{H}(\mathbf{r}^N, \mathbf{p}^N)/(k_B T)]}{Z_N}. \quad (2.2.3)$$

This has the division by  $N!$  to prevent the over counting of states due to the fact that particles are indistinguishable,  $h$  is Plank's constant and it appears in the denominator to make sure that the probability density function is correctly non-dimensionalised. We use  $(k_B T)^{-1} = \beta$ , which is known as Boltzmann's factor, with  $k_B$  being Boltzmann's constant,  $T$  is the temperature, and  $Z_N$  is the partition function.

The partition function is an important quantity in statistical mechanics because it determines all thermodynamic properties of the system being studied, as well as ensuring that  $f(\mathbf{r}^N, \mathbf{p}^N)$  is correctly normalised. It is defined as

$$Z_N = \frac{1}{N!h^{3N}} \iint \exp[-\beta \mathcal{H}(\mathbf{r}^N, \mathbf{p}^N)] d\mathbf{r}^N d\mathbf{p}^N, \quad (2.2.4)$$

where we can see the normalisation from Eqs. (2.2.2) and (2.2.3) holds. Since the momentum only appears in the kinetic energy term in the Hamiltonian, Eq. (2.2.4) can

be rewritten as

$$Z_N = \frac{1}{N!h^{3N}} \int \exp [-\beta (\Phi (\mathbf{r}^N) + \mathcal{V} (\mathbf{r}^N))] d\mathbf{r}^N \int \exp [-\beta K(\mathbf{p}^N)] d\mathbf{p}^N. \quad (2.2.5)$$

The integral over all the momenta  $\mathbf{p}^N$  is straightforward, thus by using Eq. (2.0.3) and the relation  $\int_{-\infty}^{\infty} \exp(-ax^2) dx = \sqrt{\pi/a}$ , the second integral can be expressed as

$$\begin{aligned} \int \exp [-\beta K (\mathbf{p}^N)] d\mathbf{p}^N &= \int \exp \left( -\beta \sum_{i=1}^N \frac{\mathbf{p}_i^2}{2m} \right) d\mathbf{p}^N \\ &= \prod_{i=1}^N \int \exp \left( -\beta \frac{\mathbf{p}_i^2}{2m} \right) d\mathbf{p}^i \\ &= \prod_{i=1}^N \left( \sqrt{\frac{2\pi m}{\beta}} \right)^3 = \left( \sqrt{\frac{2\pi m}{\beta}} \right)^{3N}. \end{aligned} \quad (2.2.6)$$

We simplify this by writing

$$\frac{1}{h^{3N}} \left( \sqrt{\frac{2\pi m}{\beta}} \right)^{3N} = \left( \sqrt{\frac{2\pi m}{\beta h^2}} \right)^{3N} = \Lambda^{-3N}, \quad (2.2.7)$$

where  $\Lambda$  is the thermal de Broglie wavelength. Therefore the partition function can be reduced to

$$Z_N = \frac{\Lambda^{-3N}}{N!} \int \exp [-\beta (\Phi (\mathbf{r}^N) + \mathcal{V} (\mathbf{r}^N))] d\mathbf{r}^N. \quad (2.2.8)$$

We also note that the average energy can be written as

$$\begin{aligned} U = \langle \mathcal{H} \rangle &= \iint \mathcal{H} (\mathbf{r}^N, \mathbf{p}^N) f (\mathbf{r}^N, \mathbf{p}^N) d\mathbf{r}^N d\mathbf{p}^N \\ &= \frac{1}{Z_N h^{3N} N!} \iint \mathcal{H} (\mathbf{r}^N, \mathbf{p}^N) \exp [-\beta \mathcal{H} (\mathbf{r}^N, \mathbf{p}^N)] d\mathbf{r}^N d\mathbf{p}^N \\ &= -\frac{1}{Z_N} \frac{\partial Z_N}{\partial \beta} = -\frac{\partial}{\partial \beta} \ln (Z_N). \end{aligned} \quad (2.2.9)$$

Note that in Eq. (2.2.9) we have a relationship between the internal energy of the system (a thermodynamic quantity) and the partition function (a statistical mechanics quantity). We can also show the relation

$$F = -k_B T \ln(Z_N) \quad (2.2.10)$$

is consistent with our definition of the Helmholtz free energy in Eq. (2.1.13). Since  $\beta = (k_B T)^{-1}$ , rearranging Eq. (2.2.10), we get

$$\beta F = -\ln(Z_N). \quad (2.2.11)$$

Taking derivatives with respect to  $\beta$  on both sides yields

$$\frac{\partial}{\partial \beta} (\beta F) = -\frac{\partial}{\partial \beta} (\ln Z_N) = U \quad (2.2.12)$$

by Eq. (2.2.9), which implies that

$$\frac{\partial}{\partial \beta} (\beta F) = \left( \frac{\partial \beta}{\partial \beta} \right) (F) + \beta \frac{\partial F}{\partial \beta} = F + \beta \frac{\partial F}{\partial \beta} = U. \quad (2.2.13)$$

Now

$$\beta \frac{\partial F}{\partial \beta} = \frac{1}{k_B T} \frac{\partial F}{\partial \left( \frac{1}{k_B T} \right)} = \frac{1}{T} \frac{\partial F}{\partial (T^{-1})} = \frac{-T^2}{T} \frac{\partial F}{\partial T} = -T \frac{\partial F}{\partial T}, \quad (2.2.14)$$

and thus from Eq. (2.2.13),

$$F - T \frac{\partial F}{\partial T} = U. \quad (2.2.15)$$

From Eq. (2.1.15), we have  $\frac{\partial F}{\partial T} = -S$  for fixed  $V$  and  $N$  in our canonical ensemble, and thus

$$F = U - TS. \quad (2.2.16)$$

If we assume the system is homogeneous, which means there is no external potential, then the partition function of an ideal gas, where  $\Phi = 0$  and  $\mathcal{V} = 0$ , is

$$Z_N^{id} = \frac{\Lambda^{-3N}}{N!} V^N, \quad (2.2.17)$$

where  $V^N = \int d\mathbf{r}^N$  is the volume of the system. Thus,

$$\ln(Z_N^{id}) = \ln(\Lambda^{-3N} V^N) - \ln(N!). \quad (2.2.18)$$

As  $N$  is large, by applying Stirling's formula ( $\ln y! \approx y \ln y - y$  for large  $y$ ), we get

$$\begin{aligned} \ln(Z_N^{id}) &= N \ln(\Lambda^{-3} V) - N \ln N + N \\ &= N \left[ \ln \left( \frac{\Lambda^{-3} V}{N} \right) + 1 \right], \end{aligned} \quad (2.2.19)$$

and since the number density in the system is  $\rho = N/V$ , substituting  $\ln(Z_N^{id})$  back into Eq. (2.2.10) and rearranging we obtain

$$\frac{F_{id}}{N} = k_B T [\ln(\Lambda^3 \rho) - 1]. \quad (2.2.20)$$

Since the chemical potential can be obtained by differentiation of  $F$  from Eq. (2.1.15), we have the following expression for the ideal gas chemical potential

$$\mu^{id} = \left( \frac{\partial F}{\partial N} \right)_{T,V} = k_B T \ln(\Lambda^3 \rho), \quad (2.2.21)$$

where  $\rho = N/V$  is again used. The partition function can now be written in the form

$$Z_N = \frac{Z_N^{id}}{V_N} \int \exp[-\beta(\Phi + \mathcal{V})] d\mathbf{r}^N. \quad (2.2.22)$$

Substituting back to Eq. (2.2.10) again gives

$$\begin{aligned} F &= -k_B T \ln(Z_N^{id}) - k_B T \ln \left[ \int \frac{\exp[-\beta(\Phi + \mathcal{V})]}{V^N} d\mathbf{r}^N \right] \\ &= F_{id} + F_{ex}, \end{aligned} \tag{2.2.23}$$

where  $F_{ex}$  is the excess Helmholtz free energy which includes contributions from both the molecular interactions and the external potential energy for inhomogeneous systems and  $F_{id}$  is the free energy of an ideal gas. To evaluate it,  $F_{ex}$  must almost always be approximated, although in one case it is known exactly, namely, for a 1D system of hard rods. As we show below, for inhomogeneous systems, where  $\rho$  becomes  $\rho(\mathbf{r})$ , these quantities can be written as functionals of the density profile  $\rho(\mathbf{r})$ . A particular approximation that is commonly used for molecular or colloidal systems is that referred to as ‘fundamental measure theory’, is discussed in Sec. 3.2.

## 2.3 Partition function in the grand canonical ensemble

In the grand canonical ensemble, as discussed above, we allow for an exchange of particles between the system and reservoir and therefore fix  $T$ ,  $V$ ,  $\mu$ . The appropriate free energy is the grand potential energy  $\Omega(T, V, \mu)$  and is given by

$$\Omega = F - \mu N, \tag{2.3.1}$$

and the differential of the grand potential energy is therefore [c.f. Eq. (2.1.14)]

$$d\Omega = dF - \mu dN - Nd\mu = -SdT - PdV - Nd\mu. \tag{2.3.2}$$

Thus, thermodynamic quantities can be expressed as the derivatives of the grand potential energy  $\Omega(T, V, \mu)$  with respect to an appropriate variable, such as

$$S = - \left( \frac{\partial \Omega}{\partial T} \right)_{V, \mu}, \quad P = - \left( \frac{\partial \Omega}{\partial V} \right)_{\mu, T}, \quad N = - \left( \frac{\partial \Omega}{\partial \mu} \right)_{V, T}. \quad (2.3.3)$$

In the grand canonical ensemble, the probability density function is expressed as

$$f(\mathbf{r}^N, \mathbf{p}^N) = \frac{\exp[-\beta(\mathcal{H} - \mu N)]}{\Xi}, \quad (2.3.4)$$

where the normalising factor  $\Xi$  is the grand canonical partition function

$$\begin{aligned} \Xi &= \sum_{N=0}^{\infty} \frac{1}{h^{3N} N!} \iint \exp(-\beta(\mathcal{H} - \mu N)) d\mathbf{r}^N d\mathbf{p}^N \\ &= \text{Tr} [\exp[-\beta(\mathcal{H} - \mu N)]] , \end{aligned} \quad (2.3.5)$$

where  $\text{Tr}$  is the trace operator [26], which is used as a shorthand notation for the integral over all possible position, momenta and the sum over all possible numbers of particles, and is

$$\text{Tr}(x) = \sum_{N=0}^{\infty} \frac{1}{h^{3N} N!} \iint x d\mathbf{r}^N d\mathbf{p}^N. \quad (2.3.6)$$

Thus the internal energy  $U = \langle \mathcal{H} \rangle$ , i.e. the ensemble average of  $\mathcal{H}$  in the grand canonical ensemble, is expressed as

$$\begin{aligned} \langle \mathcal{H} \rangle &= \sum_{N=0}^{\infty} \frac{1}{h^{3N} N!} \iint \mathcal{H}(\mathbf{r}^N, \mathbf{p}^N) f(\mathbf{r}^N, \mathbf{p}^N) d\mathbf{r}^N d\mathbf{p}^N \\ &= \text{Tr} (\mathcal{H} f). \end{aligned} \quad (2.3.7)$$

Moreover, the grand partition function can also be related to the grand potential in a manner analogous to that in the canonical ensemble [see Eq. (2.2.10)] via

$$\Omega = -k_B T \ln(\Xi). \quad (2.3.8)$$

## 2.4 Thermodynamic foundations of classical density functional theory (DFT)

Classical density functional theory (DFT) is a hugely powerful and widely used microscopic statistical mechanical theory for calculating the density profile  $\rho(\mathbf{r})$  for inhomogeneous systems of interacting particles, where  $\mathbf{r} = (x, y, z)$ . An advantage of DFT is that it gives a molecular-level detail description (as do, e.g. molecular dynamics computer simulations), but the computer time taken to solve DFT is typically small, particularly when the fluid average density profile only varies in one direction (e.g. perpendicular to the wall). DFT is especially suitable for determining excess thermodynamic quantities, arising from inhomogeneities in the fluid density distribution due to the presence of interfaces. There are numerous works applying DFT to study the wetting and drying interfacial phase behaviour of liquids – see for example Refs. [17, 20, 27, 28, 29, 30, 31, 32, 33, 34, 35, 36].

Now that we have a relationship between the thermodynamic grand potential and the statistical mechanical partition function for a grand canonical system, we can give an outline of the proof that minimising the grand potential gives an equilibrium state of the system.

Firstly, we can express the grand potential as a functional of the probability density

function  $f(\mathbf{r}^N, \mathbf{p}^N)$ , as suggested in [37],

$$\Omega[f] = \text{Tr}[f(\mathcal{H} - \mu N + k_B T \ln f)]. \quad (2.4.1)$$

If  $f = f^*$  is the equilibrium probability density in Eq. (2.3.4), which is a functional of the Hamiltonian  $\mathcal{H}$  and is independent of time  $t$ , then we have

$$\begin{aligned} \Omega[f^*] &= \text{Tr}[f^*(\mathcal{H} - \mu N + k_B T \ln f^*)] \\ &= \text{Tr}\left\{\frac{\exp[-\beta(\mathcal{H} - \mu N)]}{\Xi} \left[\mathcal{H} - \mu N + k_B T \left(-\frac{1}{k_B T}(\mathcal{H} - \mu N) - \ln \Xi\right)\right]\right\} \\ &= \text{Tr}\left[\frac{\exp[-\beta(\mathcal{H} - \mu N)]}{\Xi} (-k_B T \ln \Xi)\right] \\ &= -k_B T \ln \Xi \\ &= \Omega, \end{aligned} \quad (2.4.2)$$

which tells us that at equilibrium, the functional  $\Omega[f]$  in Eq. (2.4.1) equals the thermodynamic grand potential  $\Omega$  of the system. On the other hand, if  $f$  is some other arbitrarily chosen probability density function that is not the one at equilibrium, then by using

$$\mathcal{H} - \mu N = -k_B T \ln \exp[-\beta(\mathcal{H} - \mu N)] = -k_B T \ln(f^* \Xi) \quad (2.4.3)$$

together with Eq. (2.4.1) we find that

$$\begin{aligned} \Omega[f] &= \text{Tr}[f(-k_B T \ln(f^* \Xi) + k_B T \ln(f))] \\ &= \text{Tr}[f(-k_B T \ln(f^*) - k_B T \ln(\Xi) + k_B T \ln(f))] \\ &= \Omega + k_B T \text{Tr}[f \ln(f) - f \ln(f^*)] \end{aligned} \quad (2.4.4)$$

which by the Gibbs inequality, we can prove that the term  $\text{Tr}[f(\ln(f) - \ln(f^*))] \geq 0$



for all  $f$ , which further implies that

$$\Omega[f] \geq \Omega[f^*] = \Omega. \quad (2.4.5)$$

The equality only holds if  $f = f^*$ . Further details of this proof can be found in [37]. This result shows that the equilibrium state of the system always has the lowest grand potential energy. We will come back to this subject in Sec. 2.6 after we introduce the particle densities.

Returning to Eq. (2.3.5) as in the canonical ensemble, the momentum term in the grand partition function can be integrated out which gives [c.f. Eq. (2.2.6)]

$$\Xi = \sum_{N=0}^{\infty} \frac{1}{\Lambda^{3N} N!} \int \exp[-\beta(V + \Phi - \mu N)] d\mathbf{r}^N. \quad (2.4.6)$$

## 2.5 Particle densities

Our aim now is to express the grand potential free energy  $\Omega$  as a functional of the average one body density profile  $\rho(\mathbf{r})$ . This is the probability density for finding a particle located at position  $\mathbf{r}$  in space [c.f. Eq. (2.2.20)]. Firstly, we introduce the particle density operator

$$\hat{\rho}(\mathbf{r}) = \sum_{i=1}^N \delta(\mathbf{r} - \mathbf{r}_i), \quad (2.5.1)$$

where the  $\delta(\mathbf{r} - \mathbf{r}_i)$  is the Dirac  $\delta$ -function. Note also that the total number of particles  $N$  in the system can be expressed as

$$N = \int \hat{\rho}(\mathbf{r}) d\mathbf{r}. \quad (2.5.2)$$

Similarly, we may rewrite the total contribution to Hamiltonian  $\mathcal{H}$  due to the one body external potential as

$$\mathcal{V}(\mathbf{r}^N) = \sum_{i=1}^N V_{ext}(\mathbf{r}_i) = \int \hat{\rho}(\mathbf{r}) V_{ext}(\mathbf{r}) d\mathbf{r}. \quad (2.5.3)$$

Analogous to Eq. (2.3.7), the average density  $\rho(\mathbf{r})$  can be calculated as the ensemble average of the density operator:

$$\begin{aligned} \rho(\mathbf{r}) &= \langle \hat{\rho}(\mathbf{r}) \rangle = \text{Tr} [\hat{\rho}(\mathbf{r}) f(\mathbf{r})] \\ &= \sum_{N=0}^{\infty} \frac{1}{\Lambda^{3N} N!} \int \hat{\rho}(\mathbf{r}) f(\mathbf{r}) d\mathbf{r}^N \\ &= \frac{1}{\Xi} \sum_{N=0}^{\infty} \frac{1}{\Lambda^{3N} N!} \int \sum_{i=1}^N \delta(\mathbf{r} - \mathbf{r}_i) \exp[-\beta(\Phi + \mathcal{V} - \mu N)] d\mathbf{r}^N \\ &= \frac{1}{\Xi} \sum_{N=1}^{\infty} \frac{1}{\Lambda^{3N} (N-1)!} \int \exp[-\beta(\Phi + \mathcal{V} - \mu N)] d\mathbf{r}^{N-1} \\ &= \rho^{(1)}(\mathbf{r}). \end{aligned} \quad (2.5.4)$$

This is the single (or one body) particle density, for an inhomogeneous fluid. Note that it takes the form of an integral over all except one of the particle coordinates. When the external potential  $\mathcal{V} = 0$  and the pair potential  $\Phi = 0$ , then  $\rho^{(1)}(\mathbf{r}) = \rho = N/V$ , i.e. a constant. To obtain the probability density distribution function with particle number  $n < N$ , we have

$$\rho^{(n)}(\mathbf{r}_1, \mathbf{r}_2, \dots, \mathbf{r}_n) = \frac{1}{\Xi} \sum_{N=n}^{\infty} \frac{1}{\Lambda^{3N} (N-n)!} \int \exp[-\beta(\Phi + \mathcal{V} - \mu N)] d\mathbf{r}_{n+1}, d\mathbf{r}_{n+2}, \dots, d\mathbf{r}_N, \quad (2.5.5)$$

which is an integral over  $N - n$  of the particle coordinates. This arises from the fact that  $n$ -point particle density distribution functions are expressible in terms averages over products of Dirac  $\delta$ -functions. For example, when  $n = 2$ , the pair density is

$$\rho^{(2)}(\mathbf{r}_1, \mathbf{r}_2) = \left\langle \sum_{i=1}^N \sum_{\substack{j=1 \\ j \neq i}}^N \delta(\mathbf{r}_1 - \mathbf{r}_i) \delta(\mathbf{r}_2 - \mathbf{r}_j) \right\rangle, \quad (2.5.6)$$

which tells us the probability of finding a pair of particles within the volume  $d\mathbf{r}_1$  centred at the point  $\mathbf{r}_1$ , and another particle in the volume  $d\mathbf{r}_2$  centred at the point  $\mathbf{r}_2$  (the remaining  $N - 2$  particles could be anywhere).

The pair distribution function is closely related to the radial distribution function  $g(r)$ , which describes how particles at a distance of  $r = |\mathbf{r}|$  away from a given particle are related to this reference particle, and for general  $n$ , is defined as

$$g^{(n)}(\mathbf{r}_1, \mathbf{r}_2, \dots, \mathbf{r}_n) = \frac{\rho^{(n)}(\mathbf{r}_1, \mathbf{r}_2, \dots, \mathbf{r}_n)}{\prod_{i=1}^n \rho^{(1)}(\mathbf{r}_i)}. \quad (2.5.7)$$

For a bulk fluid, this simply reduces to

$$\rho^n g^{(n)}(\mathbf{r}_1, \mathbf{r}_2, \dots, \mathbf{r}_n) = \rho^{(n)}(\mathbf{r}_1, \mathbf{r}_2, \dots, \mathbf{r}_n). \quad (2.5.8)$$

Hence, for the pair distribution function, where  $n = 2$ , we have

$$\rho^2 g^{(2)}(\mathbf{r}_1, \mathbf{r}_2) = \rho^{(2)}(\mathbf{r}_1, \mathbf{r}_2) = \rho^{(2)}(|\mathbf{r}_1 - \mathbf{r}_2|) = \rho^{(2)}(r_{12}) = \rho^2 g(r_{12}), \quad (2.5.9)$$

where the above defines the bulk radial distribution function  $g(r)$ . This is of particular

importance as it relates to the total pair correlation function  $h^{(2)}(\mathbf{r}_1, \mathbf{r}_2)$  via [38]

$$h^{(2)}(\mathbf{r}_1, \mathbf{r}_2) = g^{(2)}(\mathbf{r}_1, \mathbf{r}_2) - 1, \quad (2.5.10)$$

which describes the total correlation in position between particle 1 and particle 2 at a distance  $r_{12}$  away from each other. It is also related to the static structure factor of the system via a Fourier transform, and hence can in principle be determined experimentally through X-ray or neutron scattering [39].

For all fluids that are composed of spherical particles, when the particles are far apart, i.e. when  $|\mathbf{r}_1 - \mathbf{r}_2| = r_{12} \rightarrow \infty$ , the particles' position become uncorrelated like in an ideal gas, and  $g(r_{12}) \rightarrow 1$ . However, when the separation between particles are less than the particle diameter, the radial distribution  $g(r_{12}) \approx 0$  due to the strong repulsive force. Between these two limits, a highly oscillating  $g(r_{12})$  could occur due to the packing of particles. In Fig. 2.2, we plotted the radial distribution function  $g(r)$  obtained using the Ornstein-Zernike equation and the Percus-Yevik closure relation [38] for the Lennard Jones pair potential (defined later). At  $r \approx \sigma$ , the radial distribution is at its maximum which indicates that it is most likely to find two particles at this separation. In contrast, at  $r \approx 1.5\sigma$ ,  $g(r) < 1$ , indicating a much lower probability of finding particles separated at this distance from one another, due to packing.

To calculate  $h^{(2)}(\mathbf{r}_1, \mathbf{r}_2)$ , we can use the generalisation of the Ornstein and Zernike (OZ) equation, which splits the total correlation function into a 'direct' part and an 'indirect' part [38]:

$$h^{(2)}(\mathbf{r}_1, \mathbf{r}_2) = c^{(2)}(\mathbf{r}_1, \mathbf{r}_2) + \int c^{(2)}(\mathbf{r}_1, \mathbf{r}_3) \rho^{(1)}(\mathbf{r}_3) h^{(2)}(\mathbf{r}_3, \mathbf{r}_2) d\mathbf{r}_3 \quad (2.5.11)$$

where  $c^{(2)}(\mathbf{r}_1, \mathbf{r}_2)$  is the pair direct correlation function and the rest is the indirect

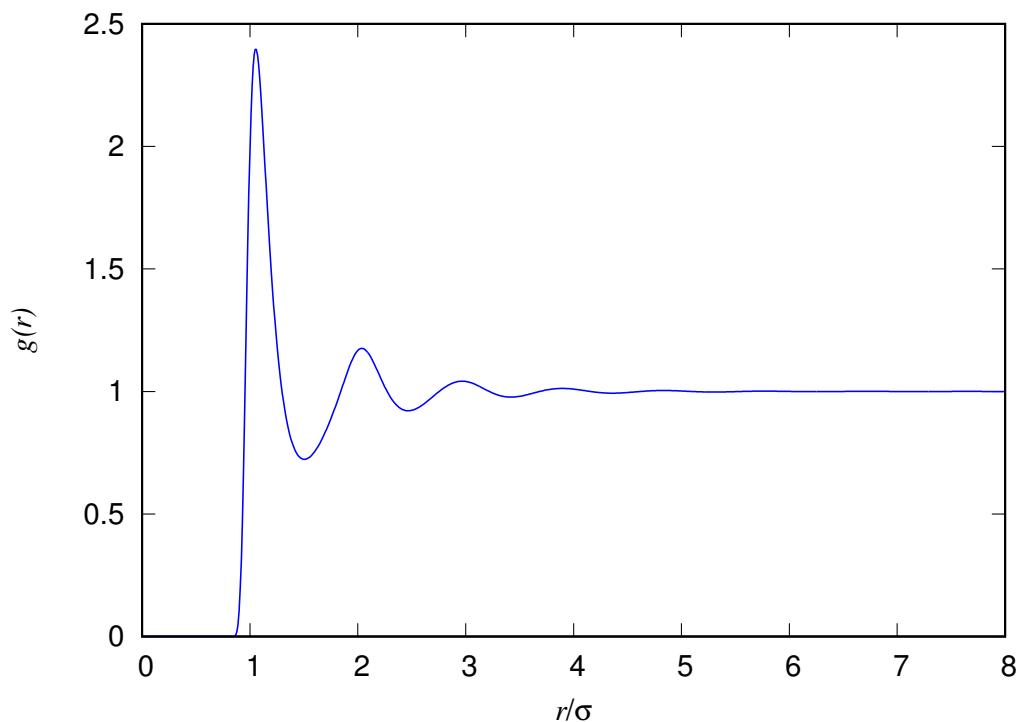


Figure 2.2: The radial distribution function  $g(r)$  as a function of  $r/\sigma$ , based on the Lennard-Jones pair potential, calculated using the Ornstein-Zernike equation, together with the Percus-Yevick closure relation, for the density  $\rho\sigma^3 = 0.8$ .

contribution, which includes all effects of a particle 1 at  $\mathbf{r}_1$ , on another particle 2 at  $\mathbf{r}_2$  via all the other particles in the system. Since at this stage  $c^{(2)}(\mathbf{r}_1, \mathbf{r}_2)$  is not defined, we need an additional equation, the ‘closure relation’, which relates  $c^{(2)}(\mathbf{r}_1, \mathbf{r}_2)$  to  $h^{(2)}(\mathbf{r}_1, \mathbf{r}_2)$  and can be used together with the OZ equation in order to solve for the total pair correlation function. The exact closure relation is given as [38]

$$c^{(2)}(r) = h^{(2)}(r) - \ln [g^{(2)}(r)] - \beta v(r) + B(r), \quad (2.5.12)$$

where  $v(r)$  is the pair potential [see Eq. (2.0.5)],  $B(r)$  is the bridge function and is in

general not known exactly and therefore must be approximated [38, 40]. An example of a well known approximation which is particularly good for hard spheres is the Percus-Yevick closure relation [38], which is defined as

$$c_{\text{PY}}^{(2)}(r) = (1 - \exp[-\beta v(r)])(h^{(2)}(r) + 1). \quad (2.5.13)$$

For purely repulsive and slowly varying pair potentials, another good approximation is called the hypernetted chain closure relation (HNC), where the bridge function  $B(r)$  is set to be zero:

$$c_{\text{HNC}}^{(2)}(r) = h^{(2)}(r) - \ln[g^{(2)}(r)] - \beta v(r). \quad (2.5.14)$$

## 2.6 Density functional theory

From Eq. (2.3.4), we can see that the equilibrium probability  $f^*$  is a functional of the external potential  $V_{\text{ext}}(\mathbf{r})$  through  $\mathcal{H} = \mathcal{K} + \mathcal{V} + \Phi$ , and from Eq. (2.5.4), we also see that the equilibrium density  $\rho^*(\mathbf{r})$  is also a functional of  $V_{\text{ext}}(\mathbf{r})$ . We can then make a proof by contradiction (see Ref. [37]) to conclude that two different density profiles can not arise from the same external potential  $V_{\text{ext}}(\mathbf{r})$ . In other words,  $V_{\text{ext}}(\mathbf{r})$  is uniquely determined by  $\rho^*(\mathbf{r})$ . Therefore, the equilibrium probability  $f^*$  is a unique functional of the equilibrium density  $\rho^*(\mathbf{r})$ , and

$$f^* = f^*[\rho^*(\mathbf{r})]. \quad (2.6.1)$$

Moreover,

$$\Omega[f^*] = \Omega[\rho^*(\mathbf{r})], \quad (2.6.2)$$

which implies that the grand potential is minimised when the density profile is that corresponding to

$$\Omega[\rho(\mathbf{r})] \geq \Omega[\rho^*(\mathbf{r})] = \Omega. \quad (2.6.3)$$

We can also rewrite the total grand potential functional  $\Omega[f]$  as a functional of the one body fluid density  $\rho(\mathbf{r})$ , as follows

$$\begin{aligned} \Omega[f] &= \Omega[\rho(\mathbf{r})] = \text{Tr}[f(\mathcal{K} + \Phi + \mathcal{V} - \mu N + k_B T \ln f)] \\ &= \text{Tr}[f(\mathcal{K} + \Phi + k_B T \ln f)] + \langle \mathcal{V}(\mathbf{r}) \rangle - \langle \mu N \rangle \\ &= \mathcal{F}[\rho(\mathbf{r})] + \int \rho(\mathbf{r}) V_{ext}(\mathbf{r}) d\mathbf{r} - \mu \int \rho(\mathbf{r}) d\mathbf{r}, \end{aligned} \quad (2.6.4)$$

where  $\mathcal{F}[\rho]$  is the intrinsic Helmholtz free energy functional and where  $\mathcal{F}[\rho] = F - \int \rho(\mathbf{r}) V_{ext}(\mathbf{r}) d\mathbf{r}$  and where  $F$  is the Helmholtz free energy. This quantity is normally not known exactly because the multiple integrals in the trace operator  $\text{Tr}$  cannot be evaluated exactly and therefore approximations must be made. As mentioned above, the equilibrium state of a system in the grand canonical ensemble occurs when  $\Omega$  is minimised. Therefore the equilibrium density profile  $\rho(\mathbf{r}) = \rho^*(\mathbf{r})$  must satisfy the Euler Lagrange equation

$$\left. \frac{\delta \Omega}{\delta \rho(\mathbf{r})} \right|_{\rho=\rho^*} = 0. \quad (2.6.5)$$

For an ideal gas, the intrinsic Helmholtz free energy functional is [see Eq. (2.2.20)]

$$\mathcal{F}_{id}[\rho(\mathbf{r})] = \int k_B T \rho(\mathbf{r}) (\ln[\Lambda^3 \rho(\mathbf{r})] - 1) d\mathbf{r}. \quad (2.6.6)$$

Therefore the intrinsic Helmholtz free energy can also be split into two parts, i.e.  $\mathcal{F} = \mathcal{F}_{id} + \mathcal{F}_{ex}$ , where  $\mathcal{F}_{id}$  is the exact free energy contribution of an ideal gas and the excess

part  $\mathcal{F}_{ex}$  contains all the information about the particle interactions. Thus,

$$\mathcal{F}[\rho(\mathbf{r})] = k_B T \int \rho(\mathbf{r}) [\ln(\Lambda^3 \rho(\mathbf{r}) - 1)] d\mathbf{r} + \mathcal{F}_{ex}[\rho(\mathbf{r})]. \quad (2.6.7)$$

Inserting Eq. (2.6.7) into Eq. (2.6.4) we obtain

$$\Omega[\rho(\mathbf{r})] = k_B T \int \rho(\mathbf{r}) [\ln(\Lambda^3 \rho(\mathbf{r}) - 1)] d\mathbf{r} + \mathcal{F}_{ex}[\rho(\mathbf{r})] + \int \rho(\mathbf{r}) (V_{ext}(\mathbf{r}) - \mu) d\mathbf{r}. \quad (2.6.8)$$

To be able to find the equilibrium state, the functional  $\Omega[\rho(\mathbf{r})]$  must be minimised with respect to the density profiles  $\rho(\mathbf{r})$ , giving

$$\frac{\delta \Omega}{\delta \rho(\mathbf{r})} = k_B T \ln(\Lambda^3 \rho(\mathbf{r})) + \frac{\delta \mathcal{F}_{ex}}{\delta \rho} + V_{ext}(\mathbf{r}) - \mu = 0. \quad (2.6.9)$$

The solution of this Euler-Lagrange equation gives the equilibrium density profile. It may be rearranged to obtain

$$\rho(\mathbf{r}) = \Lambda^{-3} \exp \left( \beta \left[ -\frac{\delta \mathcal{F}_{ex}}{\delta \rho} - V_{ext}(\mathbf{r}) + \mu \right] \right). \quad (2.6.10)$$

In general, this does not solve the problem, since  $\mathcal{F}_{ex}$  depends on  $\rho(\mathbf{r})$ . However, for an ideal gas, where  $\mathcal{F}_{ex} = 0$ , and also with  $V_{ext} = 0$ , so that the density is a constant,  $\rho(r) = \rho_b$ , we have  $\mu_{id} = k_B T \ln(\Lambda^3 \rho_b)$ , or equivalently

$$\rho_b = \Lambda^{-3} \exp(\beta \mu_{id}). \quad (2.6.11)$$

We can also define the one body direct correlation function as

$$c^{(1)}(\mathbf{r}) = -\beta \frac{\delta \mathcal{F}_{ex}[\rho(\mathbf{r})]}{\delta \rho(\mathbf{r})}. \quad (2.6.12)$$



Taking a further functional derivative of the excess part of the intrinsic free energy  $\mathcal{F}_{ex}$  with respect to the density generates the two body direct correlation function

$$c^{(2)}(\mathbf{r}_1, \mathbf{r}_2) = \frac{\delta c^{(1)}(\mathbf{r}_1)}{\delta \rho(\mathbf{r}_2)} = -\beta \frac{\delta^2 \mathcal{F}_{ex}[\rho(\mathbf{r}_1)]}{\delta \rho(\mathbf{r}_1) \delta \rho(\mathbf{r}_2)}. \quad (2.6.13)$$

If we evaluate  $c^{(2)}(\mathbf{r}_1, \mathbf{r}_2)$  for the equilibrium fluid profile,  $\rho(\mathbf{r})$ , then this is the inhomogeneous direct correlation function in the Ornstein-Zernike equation in Eq. (2.5.11) (see Ref. [26] for proof). Also, when we set  $\rho(\mathbf{r}) = \rho_b$  and  $V_{ext} = 0$  in Eq. (2.6.10) corresponding to a uniform bulk fluid, we obtain

$$\mu = k_B T \ln(\Lambda^3 \rho_b) - k_B T c^{(1)}[\rho_b]. \quad (2.6.14)$$

Hence, we see that  $c^{(1)}[\rho_b] = -\beta \mu_{ex}$ , where  $\mu_{ex}$  is the excess (over ideal gas Eq. (2.2.21)) contribution to the chemical potential. Substituting this into Eq. (2.6.14), we obtain

$$\rho(\mathbf{r}) = \rho_b \exp \left( \beta \left[ -\frac{\delta \mathcal{F}_{ex}}{\delta \rho}(\mathbf{r}) - V_{ext}(\mathbf{r}) + \mu_{ex} \right] \right). \quad (2.6.15)$$

This is the form usually used for solving DFT numerically using a Picard iterative algorithm. The Picard iterative process consists of constructing a sequence of approximate solutions, indexed by the integer  $k$ , such that the  $(k+1)$ th approximation is obtained from the previous  $k$ th approximation, and with each successively closer to the true density profile. We start by guessing an initial density profile (for example the ideal gas result), and calculate a new profile  $\rho_{rhs}$  from the right hand side of Eq. (2.6.15). Then, a small fraction of this new profile,  $\rho_{rhs}$  is mixed with the previous approximation for the profile  $\rho_k$ , to compute the new approximation  $\rho_{k+1}$  [41]:

$$\rho_{k+1} = \alpha \rho_{rhs} + (1 - \alpha) \rho_k. \quad (2.6.16)$$

The process is then iterated until it converges and a desired tolerance is achieved. Here,  $\alpha$  is the mixing parameter, which typically is chosen in the range  $0.1 > \alpha > 0.01$ . It often needs to be small for the first few iterations (small  $k$ ) where the density profiles are far from the equilibrium profile, to prevent the iterative algorithm becoming unstable, e.g. leading to too large a value of the density. Often the value of  $\alpha$  can subsequently be increased to a larger number at a later stage to enable faster convergence. See Ref. [41] for further information on choosing the value of  $\alpha$  in Picard iteration.

## Chapter 3

# Approximations Used in Density Functional Theory

The excess intrinsic Helmholtz free energy functional  $\mathcal{F}_{ex}$  is still unknown since the trace operator  $\text{Tr}$  in (2.6.4) cannot be in general evaluated exactly. To treat a system using DFT, we must develop an approximation for  $\mathcal{F}_{ex}$ . Here,  $\mathcal{F}_{ex}[\rho(\mathbf{r})]$  is approximated using a standard mean field DFT functional, which treats the attractive parts of the inter-particle potential via a simple van der Waals mean field theory [26, 38, 31, 32, 41, 42], and the repulsive part of the interactions via a functional developed for fluids of hard spheres.

### 3.1 Hard spheres

One of the main challenges in DFT is to obtain an accurate approximation for the excess Helmholtz free energy  $\mathcal{F}_{ex}$  functional. The form of this functional depends on the nature of the interactions between the particles. These typically consist of strong

repulsion at a short distance between the centres of the particles and a weak attraction at longer distances. There are various assumptions that are made concerning the form of the particle interactions and the simplest model of a fluid is to assume a system consisting of hard spheres. Suppose the fluid is composed of particles interacting via the pair potential

$$v_{hs}(r) = \begin{cases} \infty & \text{if } 0 < r \leq \sigma, \\ 0 & \text{if } \sigma < r. \end{cases} \quad (3.1.1)$$

where  $r := |\mathbf{r}_i - \mathbf{r}_j|$  is the separation distance between centres of a pair of particles  $i$  and  $j$ , and where  $\sigma$  is the hard sphere diameter. It is also the closest distance two particles can approach one another. For particles interacting solely via the potential Eq. (3.1.1), there are no interactions between the particles when they are separated by a distance that is greater than  $\sigma$ .

For hard-spheres in 1D (i.e. a fluid of hard rods), with only nearest neighbour interactions, the excess intrinsic Helmholtz free energy functional  $\mathcal{F}_{hr}$  is known exactly and is given by [43, 44]

$$\mathcal{F}_{ex}[\rho] \equiv \mathcal{F}_{hr} = -\frac{1}{\beta} \int n_0^{(1D)}(z) \ln[1 - n_1^{(1D)}(z)] dz, \quad (3.1.2)$$

where  $n_\alpha^{(1D)}(z)$  is a set of weighted density and is defined as

$$n_\alpha^{(1D)}(z) = \int \rho(z') \omega_\alpha^{(1D)}(z - z') dz', \quad (3.1.3)$$

with  $\alpha = 0, 1$  and  $\omega_\alpha^{(1D)}$  being weight functions, where the first is

$$\omega_0^{(1D)}(z) = \frac{1}{2} (\delta(z - R) + \delta(z + R)), \quad (3.1.4)$$

which corresponds to Dirac delta functions on the ends of the hard rods, which geometrically is the surface of the 1D particle, and the second weight function is

$$\omega_1^{(1D)}(z) = \Theta(R - |z|), \quad (3.1.5)$$

where  $\Theta(z)$  is the Heaviside step function and  $R = \sigma/2$  is half the length of the rod. This weight function geometrically corresponds to the 1D ‘volume’ of the rod.

## 3.2 Fundamental measure theory

To give a good approximation for the excess intrinsic Helmholtz energy for a 3D system of hard spheres  $\mathcal{F}_{hs}$ , we use fundamental measure theory (FMT) [41, 31, 42, 38] which is arguably the most successful weighted density approximation (WDA). As a starting point, Rosenfeld considered the excess free energy functional which is valid at low density limit (where only lower order terms in the density contribute) and is expressed as

$$\beta\mathcal{F}_{hs} = -\frac{1}{2} \iint \rho(\mathbf{r})\rho(\mathbf{r}')f(|\mathbf{r} - \mathbf{r}'|)d\mathbf{r}d\mathbf{r}' + \mathcal{O}(\rho^3) \quad (3.2.1)$$

where  $f(|\mathbf{r} - \mathbf{r}'|)$  is the Mayer function. For a system with particles interacting via the pair potential  $v(r)$ , we have

$$f(r) = \exp(-\beta v(r)) - 1. \quad (3.2.2)$$

If the particles interacts via the hard sphere potential, defined in Eq. (3.1.1), we have

$$f(r) = \begin{cases} -1 & \text{if } 0 < r \leq \sigma, \\ 0 & \text{if } \sigma < r. \end{cases} \quad (3.2.3)$$

### CHAPTER 3. APPROXIMATIONS USED IN DENSITY FUNCTIONAL THEORY

---

This Mayer function can be decomposed as follows

$$-f(r) = \omega_3 \otimes \omega_0 + \omega_0 \otimes \omega_3 + \omega_2 \otimes \omega_1 + \omega_1 \otimes \omega_2 - \mathbf{w}_2 \otimes \mathbf{w}_1 - \mathbf{w}_1 \otimes \mathbf{w}_2 \quad (3.2.4)$$

are weight functions which have a similar structure to the weight functions found in 1D, Eqs. (3.1.4) and (3.1.5), but extended to 3D. Together theses are [42, 45]

$$\begin{aligned} \omega_3(\mathbf{r}) &= \Theta(R - r), \\ \omega_2(\mathbf{r}) &= \delta(R - r), \\ \omega_1(\mathbf{r}) &= \frac{\omega_2(\mathbf{r})}{4\pi R}, \\ \omega_0(\mathbf{r}) &= \frac{\omega_2(\mathbf{r})}{4\pi R^2}, \\ \mathbf{w}_2(\mathbf{r}) &= \frac{\mathbf{r}}{r} \delta(R - r), \\ \mathbf{w}_1(\mathbf{r}) &= \frac{\mathbf{w}_2(\mathbf{r})}{4\pi R}, \end{aligned}$$

where  $\Theta(r)$  and  $\delta(r)$  denote the Heaviside step function and the Dirac  $\delta$ -function function respectively, and  $R = \sigma/2$  is the radius of the hard sphere. The symbol  $\otimes$  denotes the convolution, such as

$$\omega_\alpha \otimes \omega_\beta(\mathbf{r}) = \int \omega_\alpha(\mathbf{r}') \omega_\beta(\mathbf{r} - \mathbf{r}') d\mathbf{r}' \quad (3.2.5)$$

with  $\alpha, \beta = 0, 1, 2, 3$ . Here we have four scalar weight functions  $\omega_\alpha(\mathbf{r})$ , which correspond to four fundamental measures for the sphere and are known as: volume  $V$  ( $\alpha=3$ ), surface area  $S$  ( $\alpha=2$ ), radius  $R$  ( $\alpha=1$ ), and the Euler characteristic ( $\alpha=0$ ). There are also two vector weight functions  $\mathbf{w}_\alpha(\mathbf{r})$ . The convolution of the density profile  $\rho(\mathbf{r})$  with different

### CHAPTER 3. APPROXIMATIONS USED IN DENSITY FUNCTIONAL THEORY

---

weight functions generates a set of weighted densities  $\{n_\alpha(\mathbf{r})\}$ , i.e.

$$n_\alpha(\mathbf{r}) = \int \rho(\mathbf{r}') \omega_\alpha(\mathbf{r} - \mathbf{r}') d\mathbf{r}'. \quad (3.2.6)$$

For 1D rods, the exact excess free energy functional can be expressed as a function of a single weighted density. Following the structure of this exact model, Rosenfeld defined  $\mathcal{F}_{ex}$  by

$$\mathcal{F}_{hs} = \int \Phi(\{n_\alpha\}) d\mathbf{r}, \quad (3.2.7)$$

where  $\Phi(\{n_\alpha\})$  is a function of the set of weighted densities  $\{n_\alpha(\mathbf{r})\}$  and is constructed as

$$\Phi = \phi_1(n_3)n_0 + \phi_2(n_3)(n_1n_2 - \mathbf{n}_1 \cdot \mathbf{n}_2) + \phi_4(n_3)(n_2^3 - 3n_2\mathbf{n}_2 \cdot \mathbf{n}_2) \quad (3.2.8)$$

where the  $\phi_i$  functions are calculated such that the exact low density limit in Eq. (3.2.1) is recovered and also recovers the Percus-Yevick compressibility equation of state [46] and are given as

$$\phi_1(n_3) = -\ln(1 - n_3), \quad (3.2.9)$$

$$\phi_2(n_3) = \frac{1}{1 - n_3}, \quad (3.2.10)$$

$$\phi_4(n_3) = \frac{1}{24\pi(1 - n_3)^2}. \quad (3.2.11)$$

Hence, the Rosenfeld version of FMT [42] which uses both scalar and vectorial weighted densities and is given by

$$\Phi(n_\alpha) = -n_0 \ln(1 - n_3) + \frac{n_1n_2 - \mathbf{n}_1 \cdot \mathbf{n}_2}{1 - n_3} + \frac{(n_2^3 - 3n_2\mathbf{n}_2 \cdot \mathbf{n}_2)}{24\pi(1 - n_3)^2}. \quad (3.2.12)$$

In bulk, the vector weighted densities vanish and the scalar weighted densities are just the convolution of the bulk density and the weight function [41]. Note that if

the weighted density  $n_3(\mathbf{r}) > 1$ , Eq. (3.2.12) becomes undefined. Of course, this is impossible physically, since  $n_3$  is the local packing fraction. One draw back of the original version of Rosenfeld's FMT is that it does not describe the freezing transition. There are other modified versions such as the White-Bear of FMT [47] and the 2D FMT for hard disks [41]. However, for the situation to which we apply the DFT here, Rosenfeld's original version is sufficiently accurate.

### 3.3 Mean field approximation for the attraction

In the previous subsection we described the approximation for the excess Helmholtz free energy functional  $\mathcal{F}_{hs}$  for hard spheres. However, the hard sphere model is not very realistic for most systems since in this model there are only repulsive forces but no attractive forces present, which means there is only a single fluid phase with no distinction between a liquid and gas [38]. In reality, fluids are not composed of purely repulsive particles. An alternative model contains both the short ranged repulsion and the longer ranged attractive interaction and can be split as follows

$$v(\mathbf{r}, \mathbf{r}') = v_0(\mathbf{r}, \mathbf{r}') + \tilde{\lambda} v_1(\mathbf{r}, \mathbf{r}'), \quad (3.3.1)$$

where  $v_0(\mathbf{r}, \mathbf{r}')$  is the the repulsive part of the pair potential, which is treated via the hard sphere potential, and  $v_1(\mathbf{r}, \mathbf{r}')$  is the perturbation and is the attractive part. The parameter  $\tilde{\lambda}$  can be varied continuously from 0 to 1, when  $\tilde{\lambda} = 0$  the perturbation vanishes and corresponds to purely repulsive interactions, and with  $\tilde{\lambda} = 1$  the perturbation is added and corresponds to the full system with attractive interactions.

For a system with pairwise additive interactions between particles as defined in Eq. (2.0.5), we can write the partition function Eq. (2.4.6) in the grand canonical



ensemble as

$$\begin{aligned} \Xi &= \sum_{N=0}^{\infty} \frac{1}{\Lambda^{3N} N!} \int \exp(-\beta(\mathcal{V} - \mu N)) \\ &\times \exp\left(-\frac{\beta}{2} \iint \sum_{i=1}^N \sum_{\substack{j=1 \\ j \neq i}}^N \delta(\mathbf{r} - \mathbf{r}_i) \delta(\mathbf{r}' - \mathbf{r}_j) v(\mathbf{r}, \mathbf{r}') d\mathbf{r} d\mathbf{r}'\right) d\mathbf{r}^N. \end{aligned} \quad (3.3.2)$$

Inserting the above equation back into Eq. (2.3.8) and taking the derivative with respect to the pair potential  $v_1(\mathbf{r}, \mathbf{r}')$  yields [c.f. Eq. (2.5.5)]:

$$\begin{aligned} \frac{\delta \Omega}{\delta v(\mathbf{r}, \mathbf{r}')} &= -k_B T \frac{\delta \ln \Xi}{\delta v(\mathbf{r}, \mathbf{r}')} \\ &= \frac{1}{2} \left\langle \sum_{i=1}^N \sum_{\substack{j=1 \\ j \neq i}}^N \delta(\mathbf{r} - \mathbf{r}_i) \delta(\mathbf{r}' - \mathbf{r}_j) \right\rangle \\ &= \frac{1}{2} \rho^{(2)}(\mathbf{r}, \mathbf{r}') = \frac{\delta \mathcal{F}_{ex}}{\delta v(\mathbf{r}, \mathbf{r}')} \end{aligned} \quad (3.3.3)$$

Integrating<sup>1</sup> this we get

$$\mathcal{F}_{ex}[\rho(\mathbf{r})] = \mathcal{F}_0[\rho(\mathbf{r})] + \frac{1}{2} \int_0^1 d\tilde{\lambda} \iint \rho^{(2)}(\mathbf{r}, \mathbf{r}'; \tilde{\lambda}) v_1(\mathbf{r}, \mathbf{r}') d\mathbf{r} d\mathbf{r}'. \quad (3.3.4)$$

where  $\mathcal{F}_0 \approx \mathcal{F}_{hs}[\rho(\mathbf{r})]$  is the free energy functional contribution from the repulsive part of the pair potential, which in our model is the excess Helmholtz free energy functional for the hard sphere fluid  $\mathcal{F}_{hs}$  (where  $\tilde{\lambda} = 0$ ). If we make another approximation, by

---

<sup>1</sup>This is done using the differential version of Eq. (3.3.3)

$$\delta F = \frac{1}{2} \iint \rho^{(2)}(\mathbf{r}, \mathbf{r}') \delta v(\mathbf{r}, \mathbf{r}') d\mathbf{r} d\mathbf{r}'$$

and also noting from Eq. (3.3.1) that  $\delta v = v_1 d\tilde{\lambda}$ .

### CHAPTER 3. APPROXIMATIONS USED IN DENSITY FUNCTIONAL THEORY

---

neglecting in Eq. (3.3.4) correlations between the fluid particles so that  $g(\mathbf{r}, \mathbf{r}') \approx 1$ , the two body density distribution function is just the product of one body densities, i.e.

$$\rho^{(2)}(\mathbf{r}, \mathbf{r}'; \tilde{\lambda}) \approx \rho(\mathbf{r})\rho(\mathbf{r}'). \quad (3.3.5)$$

Hence Eq. (3.3.4) reduces to

$$\mathcal{F}_{ex}[\rho(\mathbf{r})] = \mathcal{F}_{hs} + \frac{1}{2} \iint \rho(\mathbf{r})\rho(\mathbf{r}')v_1(|\mathbf{r} - \mathbf{r}'|)d\mathbf{r}d\mathbf{r}', \quad (3.3.6)$$

where  $v_1(|\mathbf{r} - \mathbf{r}'|)$  is the attractive part of the pair potential, which is negative and depends continuously on the distance  $|\mathbf{r} - \mathbf{r}'|$ . This approximation is called a mean-field or van der Waals approximation [31, 38]. So, although it appears that we have made the ideal-gas approximation for  $g(r)$  in Eq. (3.3.6), actually recent work has shown this approximation is actually better than might be suggested by Eq. (3.3.5), meaning that the correlation function obtained from calculating  $g(r)$  in the so called test particle limit (where one fixes a particle and calculates the density distribution around it), is very different from the ideal gas result and is actually rather accurate [48].

There are two forms for the attractive pair potential  $v_1(\mathbf{r}, \mathbf{r}')$  that are considered in this thesis. A simple but commonly used model form is the 12 – 6 Lennard-Jones potential [12, 38, 49], which gives good approximations for the potential between a pair of molecules and is

$$v_1^{LJ}(r) = \epsilon \left[ \left( \frac{\sigma}{r} \right)^{12} - \left( \frac{\sigma}{r} \right)^6 \right], \quad (3.3.7)$$

where the parameter  $\epsilon$  determines the depth of the attractive well in this interaction potential. The Pauli-repulsion between the cores of atoms is described by the repulsive term  $r^{-12}$  at short range. The weaker, longer ranged attraction that arises from induced dipole-induced dipole interactions between molecule is modelled by the term  $\sim r^{-6}$ .

Another commonly used model for the attractive part of the potential  $v_1(\mathbf{r}, \mathbf{r}')$  is the following Yukawa potential

$$v_1^Y(r) = \begin{cases} -\epsilon & \text{if } 0 < r \leq \sigma, \\ -\epsilon \frac{\exp(-(r-\sigma)/\lambda)}{r/\sigma} & \text{if } \sigma < r, \end{cases} \quad (3.3.8)$$

where the range of the potential is defined by the length parameter  $\lambda$  and the strength of the attraction is determined by the interaction energy parameter  $\epsilon$ . A plot of the pair potential (3.3.8) is displayed in Fig. 3.1 for  $\lambda = \sigma$ , the value used throughout this thesis. We use this Yukawa model potential because it is a widely studied model fluid in DFT, see e.g. Refs. [50, 51, 28, 52, 53] for a few examples from over the years, providing a good model for simple liquids [38].

### 3.4 Bulk fluid phase diagram

For two different phases (e.g. the liquid and the vapour) to coexist in thermodynamic equilibrium, the following conditions need to be satisfied:

$$T_l = T_v,$$

$$P_l = P_v,$$

$$\mu_l = \mu_v,$$

where the subscripts  $l$  and  $v$  corresponds to liquid phase and vapour phase, and  $T$ ,  $P$  and  $\mu$  are the temperature, pressure and chemical potential respectively. If we set the external potential to be zero, i.e.  $V_{ext} = 0$ , then the fluid density  $\rho(\mathbf{r}) = \rho = N/V$  is a constant (uniform density), where  $N$  is the average number of particles in the

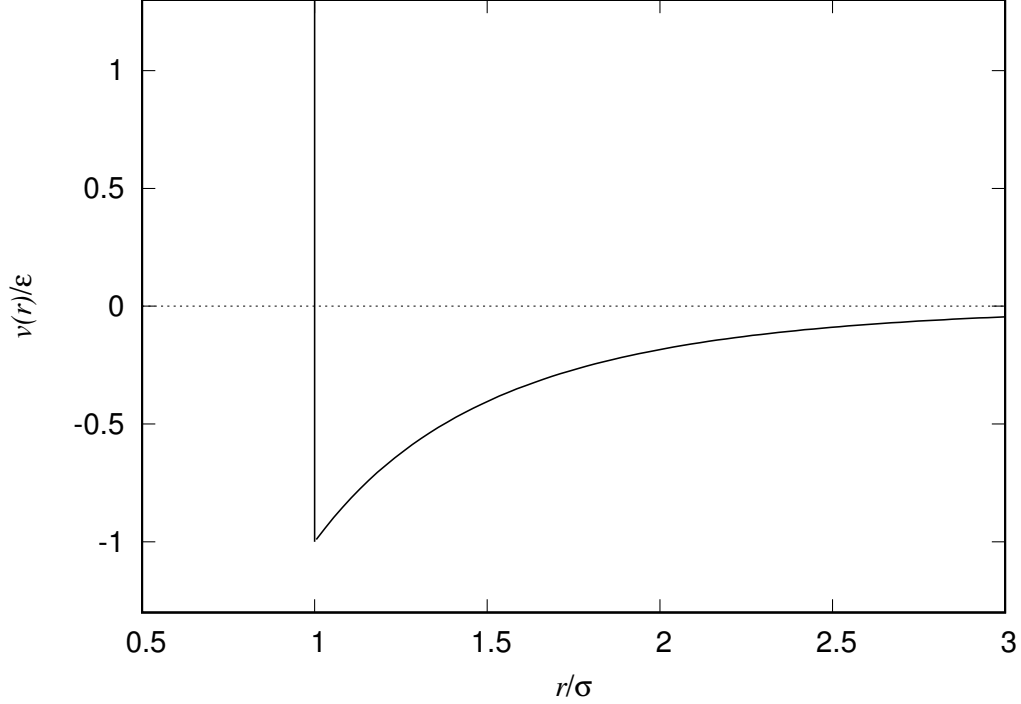


Figure 3.1: The hard-sphere plus Yukawa tail pair potential, i.e. (3.1.1) + (3.3.8), with  $\lambda = \sigma$ , which is the interaction potential between the fluid particles in our system, plotted as a function of  $r$ , the distance between the centres of the particles. The parameter  $\epsilon$  determines the strength of the attraction for  $r > \sigma$ , where  $\sigma$  is the diameter of the (hard) cores of the particles.

system and  $V$  is the volume. Substituting this into Eqs. (2.6.7) and (3.3.6) to obtain the Helmholtz free energy per volume  $f$  as

$$f = \frac{F}{V} = k_B T \rho (\ln \rho - 1) + \mathcal{F}_{hs}(\rho) + \frac{1}{2} \rho^2 \int v_1(r) d\mathbf{r}. \quad (3.4.1)$$

### CHAPTER 3. APPROXIMATIONS USED IN DENSITY FUNCTIONAL THEORY

---

With the Rosenfeld version of FMT and the Yukawa pair potential, we can write  $f$  as

$$f = \frac{F}{V} = k_B T \rho (\ln \rho - 1) - \rho \ln(1 - \eta_p) + \frac{\pi \sigma^3 \rho^2}{2(1 - \eta_p)} + \frac{\pi^2 \sigma^6 \rho^3}{24(1 - \eta_p)^2} - \frac{2\pi \epsilon \rho^2(1 + z)}{z^2} - \frac{2\pi \epsilon \rho^2}{6}. \quad (3.4.2)$$

where  $\eta_p = \frac{1}{6}\pi\sigma^3\rho$  is the packing fraction. Recalling that Eq. (2.1.14) is for the pressure, we obtain

$$P(\rho) = - \left( \frac{\partial F}{\partial V} \right)_{N,T} = \rho \frac{\partial f}{\partial \rho} - f, \quad (3.4.3)$$

and the chemical potential

$$\mu(\rho) = \left( \frac{\partial F}{\partial N} \right)_{V,T} = \frac{\partial f}{\partial \rho}. \quad (3.4.4)$$

Thus the coexisting liquid and vapour densities can be found as the solution to the equations

$$P(\rho_l) = P(\rho_v), \quad (3.4.5)$$

$$\mu(\rho_l) = \mu(\rho_v), \quad (3.4.6)$$

which is equivalent to solving

$$\left. \frac{\partial f}{\partial \rho} \right|_{\rho=\rho_l} = \left. \frac{\partial f}{\partial \rho} \right|_{\rho=\rho_v}, \quad (3.4.7)$$

$$\left[ \rho \frac{\partial f}{\partial \rho} - f \right]_{\rho=\rho_l} = \left[ \rho \frac{\partial f}{\partial \rho} - f \right]_{\rho=\rho_v}. \quad (3.4.8)$$

From these two relations, we can then write down a set of simultaneous equations for the coexisting vapour and liquid densities,  $\rho_v$  and  $\rho_l$ , respectively, which are then solved for numerically over a range of temperatures to obtain the bulk fluid binodal [38].

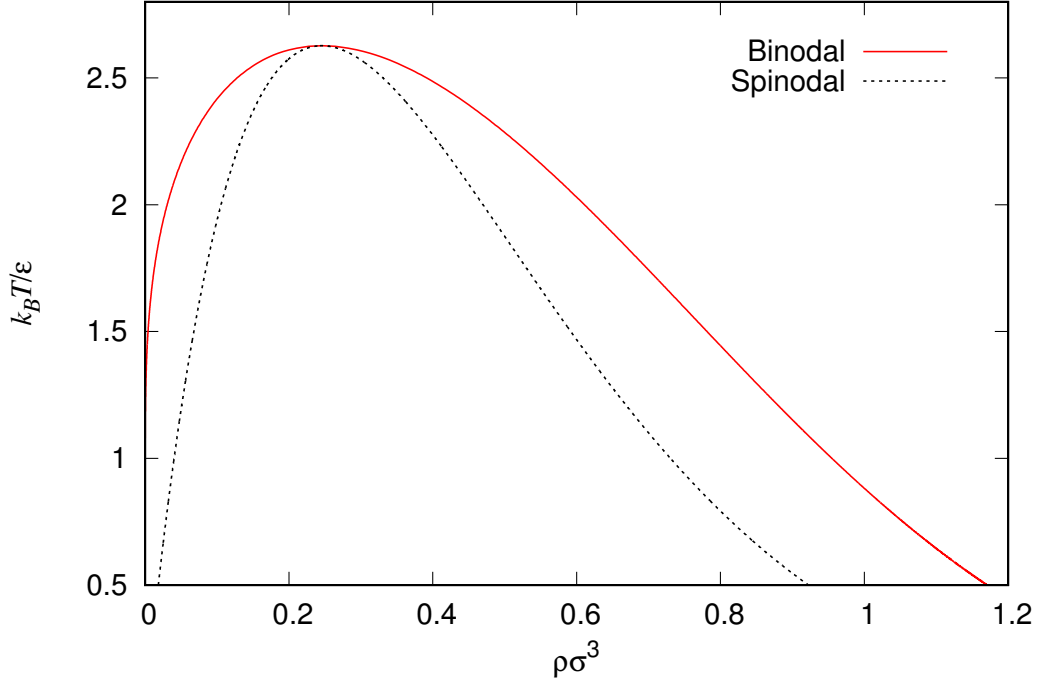


Figure 3.2: Bulk fluid phase diagram of the fluid with hard-sphere plus Yukawa tail pair potential in the temperature versus density plane, for the system with  $\lambda = \sigma$  and  $z = \sigma$ . The solid line corresponds to the binodal curve and the dashed line corresponds to the spinodal curve.

In Fig. 3.2 we display the resulting bulk fluid phase diagram, showing the binodal curve giving the two distinct densities of the vapour and liquid phases at bulk coexistence. As the temperature  $T$  is increased, the density difference between the two coexisting phases decreases and finally becomes zero at the critical temperature  $T_c$ . The fluid in the area of the phase diagram outside the binodal curve is stable and phase separation no longer occurs, this corresponds to the single phase region. The spinodal curve shows the boundary of instability and is determined where the curvature of the

free energy is zero

$$\frac{\partial^2 f}{\partial \rho^2} = 0. \quad (3.4.9)$$

The region inside the spinodal curve (within the region where two phase coexistence occurs) is where a uniform phase with the given density will phase separate spontaneously. In contrast, for densities between the spinodal and the binodal curves, phase separation is a nucleated process, with a free energy barrier that must be surmounted by thermal fluctuations [54].

### 3.5 Fluids at interfaces

For a system at bulk vapour liquid coexistence, we find that the average one body density  $\rho(\mathbf{r})$  takes a constant value in the bulk of the two distinct phases, but varies smoothly through the interfacial region. In this case, the surface makes a contribution to the free energy. Since both the liquid and the vapour density have the same grand potential energy at coexistence, the free energy cost of having such an interface can be defined as the excess grand potential per unit area. A density profile for a system with periodic boundary conditions is shown in Fig. 3.3. Hence we have,

$$\gamma = \frac{\Omega - \Omega_b}{A} = \frac{\Omega_{ex}}{A}, \quad (3.5.1)$$

where  $A$  is the interfacial area,  $\gamma$  is the interfacial tension, the total grand potential  $\Omega$  is divided into a bulk contribution  $\Omega_b$ , i.e. fluid with no interface, and a surface excess contribution  $\Omega_{ex}$ .  $\Omega_b = -PV$  is the grand potential for a bulk system with no interfaces,  $V$  is the volume of the whole system, (it is the length of the system in a 1D calculation) and  $P$  is the pressure of the coexisting bulk phases. In our system, we assume that the fluid density only varies in the  $z$  direction and has periodic boundary

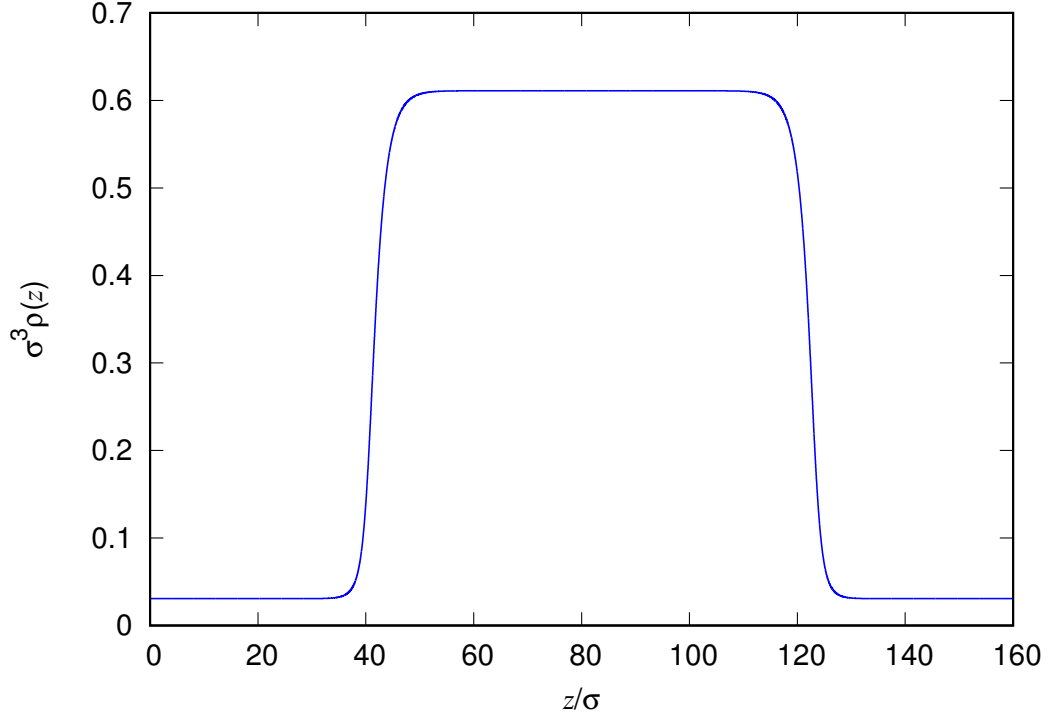


Figure 3.3: Equilibrium density profile calculated at liquid vapour coexistence using DFT, showing two liquid-vapour interfaces. We assume the system only varies in the  $z$ -direction, so the system is a slab of liquid next to a slab of vapour, periodically repeated.

conditions, which leads to there being two vapour liquid interfaces (see Fig. 3.3). Thus, the liquid vapour surface tension  $\gamma_{lv}$  can be calculated as

$$\gamma_{lv} = \frac{\Omega - \Omega_b}{2A} = \frac{\Omega + PV}{2A}. \quad (3.5.2)$$



## 3.6 Binding potential

In the presence of an external field,  $V_{ext}$ , due to the wall, we have another interface in the system, namely that between the wall and the fluid. Moreover, when this interface and the liquid-vapour interface become sufficiently close to one another, they can influence one another. The fluid particles near the solid wall experience attractive van der Waals forces from both the fluid molecules and solid molecules. Depending on the balance of the forces, sometimes the system can lower its free energy by increasing the distance between the two interfaces, which leads to a macroscopically thick layer of fluid in contact with the wall even when the vapour is the equilibrium bulk phase. Similarly, when the bulk phase is the liquid, sometimes a thick film of the vapour is favoured at the wall, this is drying. Hence, minimising the liquid-vapour surface area is no longer necessarily the condition for minimising the free energy of the system. We must also include additional contributions to the grand potential free energy. When there is a film of liquid on the solid surface, there is the excess free energy (interfacial tension) due to this interface, i.e.  $\gamma_{sl}$ . Additionally, when these interfaces are close to one another, there are contributions from interaction between these two interfaces that are included via the so called binding potential  $g(h)$ , where  $h$  is the distance between the interfaces, i.e. the thickness of the liquid film. A schematic diagram is shown in Fig. 3.4. The left hand figure shows a fluid confined in a volume  $V$ , in contact with a planar substrate with area  $A$ . The height of the whole system is  $L$  and with density distribution  $\rho(\mathbf{r})$ . However, due to the surface interactions and the fact that the bulk phase is close to liquid-vapour phase coexistence, a thick layer of vapour, with thickness  $h$ , is adsorbed at the wall. In an analogous fashion, in the right hand panel of Fig. 3.4, the equilibrium consists of a thick film of liquid adsorbed at the wall in coexistence with the bulk vapour phase; the wall is wet by a liquid film of thickness  $h$ .

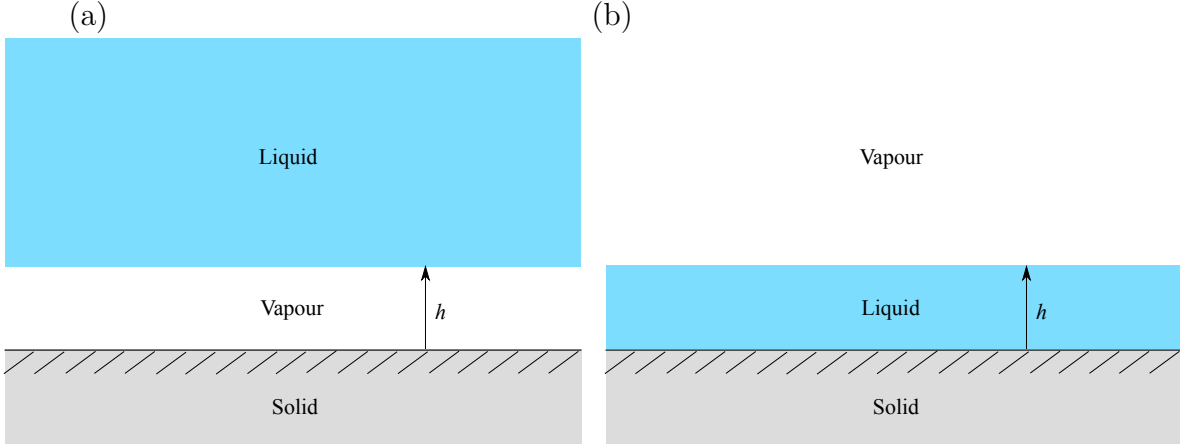


Figure 3.4: A schematic diagram of the system with: (a) a uniform thickness layer of vapour adsorbed at the interface between a planar solid substrate and the bulk liquid. The thickness of the vapour film is  $h$ . This corresponds to considering a bubble. (b) A liquid film layer in contact with the solid substrate, which corresponds to a liquid drop.

Note, however, that from the microscopic (statistical mechanics) viewpoint, the adsorption is a better defined and arguably more useful measure of the amount of a particular phase on the substrate, than the film thickness  $h$  [4]. This is because when the amount of the phase adsorbed on the substrate is small and on microscopic length scales, e.g. when there is sub-monolayer adsorption at an interface [4, 6, 55], then talking about a film height that is a fraction of a molecule does not make physical sense, whilst the adsorption is well-defined. In fact, when the vapour pressure is non-zero, the adsorption on a substrate can in principle even be negative, so in this case, talking about a film height is meaningless. The total adsorption on the substrate is calculated from the fluid density profile as

$$\Gamma = \frac{1}{A} \int_V (\rho(\mathbf{r}) - \rho_b) \, d\mathbf{r}, \quad (3.6.1)$$

where  $\rho_b$  is the bulk fluid density, which in the context of liquids on surfaces with the bulk phase being the gas, then  $\rho_b = \rho_v$ , where  $\rho_v$  is the vapour density at bulk coexistence. However, we also consider bubbles on surfaces here and in this case  $\rho_b = \rho_l$ , the liquid density.

If we assume the  $z$ -axis is perpendicular to the substrate, which has its planar surface corresponding to the  $z = 0$  plane in a Cartesian coordinate system, then we can define the local adsorption as

$$\Gamma(x, y) = \int_0^\infty [\rho(x, y, z) - \rho_b] dz. \quad (3.6.2)$$

The corresponding height  $h(x, y)$ , quantifying the amount of the phase that is on the substrate, may be defined in a number of ways. This lack of a unique definition is another reason why  $\Gamma(x, y)$  is a better measure. For example, one could define  $h(x, y)$  to be the position where the average density  $\rho(x, y, z = h)$  is given as  $(\rho_b + \rho_a)/2$ , i.e. the average of the bulk density and the density of the phase adsorbed on the substrate,  $\rho_a$ .

However, here we prefer to define the film height  $h$  as [4, 6, 55]

$$h(x, y) \equiv \frac{\Gamma(x, y)}{\rho_a - \rho_b}. \quad (3.6.3)$$

In the situation where the bulk phase is the vapour (with density  $\rho_b = \rho_v$ ) and the phase adsorbed on the surface is the liquid (with density  $\rho_a = \rho_l$ ), then this is a widely used definition. Note also that in the case when the liquid is the bulk phase ( $\rho_b = \rho_l$ ) and it is the vapour that is adsorbed at the interface ( $\rho_a = \rho_v$ ), then in general both of the quantities in the numerator and denominator on the right hand side of Eq. (3.6.3) are negative, but of course still giving a positive thickness  $h$ .

Consider the two systems illustrated in Fig. 3.4. Treating them in the grand canon-

ical ensemble, the grand potential  $\Omega$  is the relevant free energy to consider, which is minimised when the system is at equilibrium. To describe the interfacial phase behaviour, we follow the usual procedure [56] and consider surface excess quantities; in this case, as mentioned above, it is the total excess grand potential  $\Omega_{ex}$ , in terms of adsorption is then for a liquid film at the wall with the vapour being the bulk phase we have

$$\Omega_{ex}(\Gamma) = A\gamma_{lv} + A\gamma_{sl} + Ag_l(\Gamma), \quad (3.6.4)$$

and for the vapour adsorbed at the wall with the bulk being the liquid, we have

$$\Omega_{ex}(\Gamma) = A\gamma_{lv} + A\gamma_{sv} + Ag_v(\Gamma). \quad (3.6.5)$$

The interfacial tensions  $\gamma_{sl}$  and  $\gamma_{sv}$  are the solid liquid and solid vapour surface tension respectively, and can be calculated using DFT in a similar approach to  $\gamma_{lv}$  (c.f. Eq. (3.5.2)) [26, 38, 32, 33], except there is only a single interface and hence the result does not need to be divided by 2. Equations (3.6.4) and (3.6.5) assume the system is at bulk liquid vapour phase coexistence.

More generally, for a bulk system having the same volume  $V$  and pressure  $P$ , but with no interface, the grand potential is  $\Omega_b = -PV$ , hence using  $\Omega_{ex} = \Omega - \Omega_b$ , and noting that the volume of the phase adsorbed at the wall is  $Ah$ , the excess grand potential per unit area can be split into the following contributions for the case when the vapour is adsorbed at the wall

$$\frac{\Omega_{ex}}{A} = \frac{\Omega - \Omega_b}{A} = h(P_l - P_v) + \gamma_{lv} + \gamma_{sv} + g_v(\Gamma), \quad (3.6.6)$$

and an analogous formula for the case in Fig. 3.4 (b). Here,  $P_l - P_v = \delta P$  is the pressure difference between the pressure of the bulk liquid and that of the corresponding vapour

at the same chemical potential  $\mu$ . If the system is at bulk vapour-liquid coexistence, then we have  $P_l = P_v$  and Eq. (3.6.6) reduces to Eq. (3.6.5). The above equation may be viewed as defining the binding potential: it is the ‘remainder’ after the other terms have been subtracted, i.e. at bulk vapour-liquid coexistence, with  $\delta P = 0$ , the binding potential can be calculated using [57]

$$g_v(\Gamma) = \frac{\Omega + PV}{A} - \gamma_{lv} - \gamma_{sv}. \quad (3.6.7)$$

Similarly, the binding potential of a system with a film of liquid with adsorption  $\Gamma$  is:

$$g_l(\Gamma) = \frac{\Omega + pV}{A} - \gamma_{lv} - \gamma_{sl}. \quad (3.6.8)$$

Solving the Euler Lagrange equation Eq. (2.6.9) as described at the end of Sec. 2 gives the equilibrium fluid density profile  $\rho^*$  that has an adsorption  $\Gamma_0$ , as determined by Eq. (3.6.2). Using this density profile as an input and substituting into Eq. (2.6.8) we obtain the value of the grand potential energy of our system. Together with Eq. (3.6.7), we can find the minimum value of the binding potential  $g(\Gamma_0)$ , i.e. for bulk vapour, we have [1]

$$g_l(\Gamma_0) = \gamma_{sv} - \gamma_{sl} - \gamma_{lv}, \quad (3.6.9)$$

and for the case where the bulk phase is the liquid

$$g_v(\Gamma_0) = \gamma_{sl} - \gamma_{sv} - \gamma_{lv}. \quad (3.6.10)$$

When  $|\Gamma| \rightarrow \infty$ , the two interfaces are far from one another, so they do not influence each other, and therefore we have  $g_l(\Gamma) \rightarrow 0$  and  $g_v(\Gamma) \rightarrow 0$ .

Using the Young equation [2]  $\gamma_{lv} \cos \theta = \gamma_{sv} - \gamma_{sl}$ , we obtain from (3.6.9) and (3.6.10)

the following two results [1, 58, 59]

$$\cos \theta = 1 + \frac{g_l(\Gamma_0)}{\gamma_{lv}}, \quad (3.6.11)$$

$$\cos \theta = -1 - \frac{g_v(\Gamma_0)}{\gamma_{lv}}, \quad (3.6.12)$$

where  $\theta$  is the equilibrium contact angle, measured as in the usual definition as the angle through the liquid phase. Therefore, this is the outer angle on bubbles and so we have the opposite sign in the second equation compared to when considering liquid drops.

To find the full binding potential curve  $g_l(\Gamma)$  and  $g_v(\Gamma)$  using DFT, one must calculate for a series of constrained density profiles, the constraint being that the adsorption at the wall  $\Gamma$  (rather than the adsorbed film thickness  $h$ ) takes a series of specified values. This can be done by applying the fictitious potential approach proposed in Ref. [60] and further developed by Hughes *et al.* [4, 6]. This method constrains the adsorption of the system to be a desired value by modifying the Picard iteration by replacing  $\rho_{rhs}$  in Eq. (2.6.16) with

$$\rho_{new} = (\rho_{rhs} - \rho_b) \frac{\Gamma_d}{\Gamma_{rhs}} + \rho_b, \quad (3.6.13)$$

where  $\Gamma_{rhs}$  is the adsorption corresponding to the profile  $\rho_{rhs}$  calculated via Eq. (3.6.1) and  $\Gamma_d$  is the desired value of the adsorption.

The required constraint takes the form of a fictitious external potential that can be calculated self-consistently as part of the algorithm for determining the constrained density profile. This desired adsorption is then increased slightly, using the previous calculated density profile as an initial approximation, we find the new constrained

equilibrium density profile that corresponds to the specified value of the adsorption, which gives us the next value of the binding potential. Repeating this procedure we get a series of points with each point being the value of the binding potential for a particular adsorption.

Hughes *et al.* [4, 6] applied the method to determine the binding potential for films of liquid adsorbed on a surface in contact with a bulk vapour. Taking the resulting binding potentials together with the IH results in droplet profiles are in excellent agreement with those obtained from solving the full DFT to determine the droplet profile [4, 6], validating the overall coarse graining approach. Further validation comes from Ref. [61] where two other completely different approaches for obtaining  $g(\Gamma)$  were used that nonetheless produce identical results. These two approaches are: (i) applying the nudged-elastic-band algorithm to connect the sequence of density profiles required to calculate  $g$  and (ii) a method based on an overdamped nonconserved dynamics to explore the underlying free-energy landscape. For liquid droplets, the resulting binding potential can also be incorporated into a thin film hydrodynamic equation to study the dynamics of liquid droplets on surfaces [55], which will be discussed in Chap. 6.

# Chapter 4

## Thin Film Equation

The results from DFT enable us to accurately describe the binding potential allowing to bridge the gap from the microscopic properties of particles to the mesoscopic collective behaviour, e.g. to the wetting behaviour of fluids. In order to investigate how the non-equilibrium dynamics over time and the shape of a drop over time are related to the microscopic interactions between particles, the thin film equation is applied. This equation (originating from hydrodynamics, as we derive below) shows that the time evolution of the thin film of fluid on a solid substrate  $h(x, t)$  is given by

$$\frac{\partial h}{\partial t} = \frac{\partial}{\partial x} \left[ \frac{h^3}{3\eta} \frac{\partial}{\partial x} \frac{\delta F_{\text{IH}}}{\delta h} \right], \quad (4.0.1)$$

where  $h(x, t)$  is the liquid film thickness at time  $t$  and position  $x$  on a solid substrate, i.e. for simplicity we assume that the profile only varies in one direction over the surface,  $\eta$  is the fluid dynamic viscosity and

$$F_{\text{IH}}[h] = \int \left[ g(h) + \gamma_v \sqrt{1 + \left( \frac{\partial h}{\partial x} \right)^2} \right] dx. \quad (4.0.2)$$



is the free energy of the system, which is the form in Eq. (1.3.9) reduces to when the film height profile varies only in one direction.

In the following we derive this equation from Navier-Stokes equation, using what is referred to as the long-wave or lubrication approximation [62, 63]. It reduces the full Navier-Stokes equations to a nonlinear fourth order partial differential equation which is simpler to solve and computationally much more efficient. Consider the particular example of the motion of a thin liquid film over a surface. The movement of this droplet is driven by various properties. Assume the fluid is an incompressible Newtonian viscous fluid of constant density  $\rho$  and dynamic viscosity  $\eta$ . For simplicity in the derivation we assume the system is two dimensional. However, the argument generalises straight forwardly for three dimensions. The fluid free surface is given by  $z = h(x, t)$ .  $P(x, z, t)$  is the pressure in the fluid and the liquid is moving in a positive  $x$ -direction with velocity  $\underline{v} = (u, w)$ , where  $u$  and  $w$  are the velocity components along the  $x$ -direction and the  $z$ -direction. We know from fluid mechanics that the evolution of the fluid and its free surface, in the absence of body forces, obeys the Navier-Stokes equations, which are expressed based on the principle of conservation of mass and momentum. Thus for the  $x$ -component and  $z$ -component momentum equations we have

$$\rho \left( \frac{\partial u}{\partial t} + u \frac{\partial u}{\partial x} + w \frac{\partial u}{\partial z} \right) = -\frac{\partial P}{\partial x} + \eta \left( \frac{\partial^2 u}{\partial x^2} + \frac{\partial^2 u}{\partial z^2} \right) \quad (4.0.3)$$

$$\rho \left( \frac{\partial w}{\partial t} + u \frac{\partial w}{\partial x} + w \frac{\partial w}{\partial z} \right) = -\frac{\partial P}{\partial z} + \eta \left( \frac{\partial^2 w}{\partial x^2} + \frac{\partial^2 w}{\partial z^2} \right), \quad (4.0.4)$$

and the continuity equation is

$$\frac{\partial u}{\partial x} + \frac{\partial w}{\partial z} = 0. \quad (4.0.5)$$

To proceed, the mathematical analysis is most easily understood with dimensionless

variables, so we non-dimensionalise, by scaling

$$x = Lx^*, z = \epsilon Lz^*, h = \epsilon Lh^*, u = Uu^*, w = \epsilon Uw^*, P = \frac{3\eta U}{\epsilon^2 L} P^*, t = \frac{L}{U} t^*,$$

where the ratio of the film height to its characteristic length,  $\epsilon = \frac{H}{L} \ll 1$  is assumed as the film we considered is sufficiently thin so the variations along the horizontal direction are much more important than the one normal to the surface,  $x^*, z^*, u^*, w^*, t^*, P^*$  are dimensionless quantities, the pressure scale is chosen to balance the pressure and viscosity force.  $U$  is the characteristic velocity scale,  $L$  is the characteristic length scale and  $T$  is the characteristic time scale.

By substituting the above non-dimensional expressions into the above governing equations, we obtain

$$\frac{\rho UL}{\eta} \left( \frac{\partial u^*}{\partial t^*} + u^* \frac{\partial u^*}{\partial x^*} + w^* \frac{\partial u^*}{\partial z^*} \right) = -\frac{3}{\epsilon^2} \frac{\partial P^*}{\partial x^*} + \frac{\partial^2 u^*}{\partial x^{*2}} + \frac{1}{\epsilon^2} \frac{\partial^2 u^*}{\partial z^{*2}}, \quad (4.0.6)$$

$$\epsilon \frac{\rho UL}{\eta} \left( \frac{\partial w^*}{\partial t^*} + u^* \frac{\partial w^*}{\partial x^*} + w^* \frac{\partial w^*}{\partial z^*} \right) = -\frac{3}{\epsilon^3} \frac{\partial P^*}{\partial z^*} + \epsilon \frac{\partial^2 w^*}{\partial x^{*2}} + \frac{1}{\epsilon} \frac{\partial^2 w^*}{\partial z^{*2}}, \quad (4.0.7)$$

$$\frac{\partial u^*}{\partial x^*} + \frac{\partial w^*}{\partial z^*} = 0, \quad (4.0.8)$$

where  $Re = \frac{\rho UL}{\eta}$  is the dimensionless Reynolds number that corresponds to the ratio of the velocity and viscosity. Multiplying Eq. (4.0.6) by  $\epsilon^2$  and Eq. (4.0.7) by  $\epsilon^3$  gives

$$\epsilon^2 Re \left( \frac{\partial u^*}{\partial t^*} + u^* \frac{\partial u^*}{\partial x^*} + w^* \frac{\partial u^*}{\partial z^*} \right) = -3 \frac{\partial P^*}{\partial x^*} + \epsilon^2 \frac{\partial^2 u^*}{\partial x^{*2}} + \frac{\partial^2 u^*}{\partial z^{*2}}, \quad (4.0.9)$$

$$\epsilon^4 Re \left( \frac{\partial w^*}{\partial t^*} + u^* \frac{\partial w^*}{\partial x^*} + w^* \frac{\partial w^*}{\partial z^*} \right) = -3 \frac{\partial P^*}{\partial z^*} + \epsilon^4 \frac{\partial^2 w^*}{\partial x^{*2}} + \epsilon^2 \frac{\partial^2 w^*}{\partial z^{*2}}. \quad (4.0.10)$$

Taking the limit as  $\epsilon \rightarrow 0$ , and assuming that  $\epsilon^2 Re \ll 1$ , the Navier-Stokes and

continuity equation can then be reduced to the simplified forms [64]

$$\frac{\partial^2 u^*}{\partial z^{*2}} - 3 \frac{\partial P^*}{\partial x^*} = 0, \quad (4.0.11)$$

$$-3 \frac{\partial P^*}{\partial z^*} = 0, \quad (4.0.12)$$

$$\frac{\partial u^*}{\partial x^*} + \frac{\partial w^*}{\partial z^*} = 0. \quad (4.0.13)$$

At the solid fluid surface, the no slip and no penetration boundary conditions are assumed,

$$u^*(x^*, 0) = 0, \quad w^*(x^*, 0) = 0, \quad (4.0.14)$$

and at the liquid vapour interface, the tangential stress balance is applied as<sup>1</sup>,

$$\frac{\partial u^*}{\partial z^*} = 0 \quad \text{on} \quad z^* = h^*. \quad (4.0.15)$$

At the free interface, where we have the kinematic boundary condition since there is no flux across the free interface,

$$\frac{\partial h^*}{\partial t^*} + u^* \frac{\partial h^*}{\partial x^*} = w^* \quad \text{on} \quad z^* = h^*. \quad (4.0.16)$$

Then we can solve the system directly by integrating Eq. (4.0.11) twice with boundary

---

<sup>1</sup>For use of the reader, before neglecting terms of order  $\epsilon^2$ , this tangential stress balance is given as [65]

$$\left( \epsilon^2 \left( \frac{\partial h^*}{\partial x^*} \right)^2 - 1 \right) \left( \frac{\partial u^*}{\partial z^*} + \epsilon^2 \frac{\partial w^*}{\partial x^*} \right) + 4\epsilon^2 \frac{\partial u^*}{\partial x^*} \frac{\partial h^*}{\partial x^*} = 0$$

conditions Eq. (4.0.14) and Eq. (4.0.15) to find the thin film velocity profile. It gives:

$$u^*(z^*) = 3 \frac{\partial P^*}{\partial x^*} \left( \frac{z^{*2}}{2} - h^* z^* \right). \quad (4.0.17)$$

Using the relation in Eq. (4.0.13), differentiating Eq. (4.0.17) with respect to  $x$  and integrating  $\frac{\partial w^*}{\partial z^*}$  with respect to  $z^*$  with boundary condition Eq. (4.0.14) gives rise to

$$w^* = 3 \frac{\partial P^*}{\partial x^*} \frac{\partial h^*}{\partial x^*} \frac{z^{*2}}{2} - 3 \frac{\partial^2 P^*}{\partial x^{*2}} \left( \frac{z^{*3}}{6} - \frac{h z^{*2}}{2} \right). \quad (4.0.18)$$

Substituting Eq. (4.0.18) into the kinematic boundary condition Eq. (4.0.16) and simplify gives the following equations for the time evolution of the film height profile

$$\frac{\partial h^*}{\partial t^*} = \frac{\partial}{\partial x^*} \left( h^{*3} \frac{\partial P^*}{\partial x^*} \right). \quad (4.0.19)$$

There are normally 2 contributions to this pressure: the Young-Laplace capillary effect  $\gamma_{lv} \frac{\partial^2 h}{\partial x^2}$  [66] and the intermolecular interactions in the film which are taken into consideration by introducing an additional disjoining pressure term  $\Pi(h) = -\frac{\partial g(h)}{\partial h}$ , i.e. from the binding potential which originates from the molecular interactions as explained in the previous chapter. As one passes across a curved liquid-vapour interface, there is a jump in pressure [67]. The increase in pressure  $\Delta P$  is equal to the product of a surface tension  $\gamma$  and the curvature  $\kappa$  of the surface. Thus the pressure in the liquid is given by

$$P = -\gamma_{lv} \kappa - \Pi(h) \approx -\gamma_{lv} \frac{\partial^2 h}{\partial x^2} - \Pi(h), \quad (4.0.20)$$

where  $\gamma_{lv}$  is the liquid-vapour surface tension,  $\kappa$  is the curvature and  $\Pi(h)$  is the disjoining pressure.

Eq. (4.0.20) is in dimensional form. By introducing the non-dimensionalisation as

previously and an additional scaling  $\Pi = \Pi^* \frac{3\eta U}{\epsilon^2 L}$ , we get

$$P^* = -\frac{\partial^2 h^*}{\partial x^{*2}} \frac{\gamma_{lv} \epsilon^3}{3\eta U} - \Pi^*, \quad (4.0.21)$$

and then noting that  $Ca = \frac{3\eta U}{\gamma_{lv}}$  is the capillary number and is assumed to be of order  $\epsilon^3$ , for the dominant balance to retain physically relevant terms (i.e. to retain surface tension). Thus Eq. (4.0.21) becomes

$$P^* = -\gamma_{lv}^* \frac{\partial^2 h^*}{\partial x^{*2}} - \Pi^*, \quad (4.0.22)$$

and substituting this pressure term back to Eq. (4.0.19) one obtains

$$\frac{\partial h^*}{\partial t^*} = \frac{\partial}{\partial x^*} \left[ h^{*3} \frac{\partial}{\partial x^*} \left( -\gamma_{lv}^* \frac{\partial^2 h^*}{\partial x^{*2}} - \Pi^* (h^*) \right) \right], \quad (4.0.23)$$

Subsequently, we drop the ‘\*’ for brevity. Equation (4.0.23) is 1st order in time and 4th order in space, and is non-linear and commonly known as the thin film equation. It describes the time evolution of the liquid film thickness and can be solved using numerical techniques described in Chapter 6. Equation (4.0.23) is the nondimensionalised form of Eq. (4.0.1) with the free energy

$$F_{IH} [h] = \int \left[ g(h) + \frac{\gamma_{lv}}{2} \left( \frac{\partial h}{\partial x} \right)^2 \right] dx, \quad (4.0.24)$$

which is obtained from Eq. (1.3.9) using the long-wave approximation  $\sqrt{1 + \left( \frac{\partial h}{\partial x} \right)^2} \approx 1 + \frac{1}{2} \left( \frac{\partial h}{\partial x} \right)^2$ . This equation is the long wave approximation version of Eq. (1.3.9) in the case where the height only varies in the  $x$ -direction and not in the  $y$ -direction.

## Chapter 5

# Binding Potentials for Vapour Nanobubbles on Surfaces Using Density Functional Theory

In this chapter we calculate density profiles of a simple model fluid in contact with a planar surface using density functional theory (DFT), in particular for the case where there is a vapour layer intruding between the wall and the bulk liquid. We apply the method of Hughes *et al.* [4] to calculate the density profiles for varying (specified) amounts of the vapour adsorbed at the wall. This is equivalent to varying the thickness  $h$  of the vapour at the surface. From the resulting sequence of density profiles we calculate the thermodynamic grand potential as  $h$  is varied and thereby determine the binding potential as a function of  $h$ . The binding potential obtained via this coarse-graining approach allows us to determine the disjoining pressure in the film and also to predict the shape of vapour nano-bubbles on the surface. Our microscopic DFT based approach captures information from length scales much smaller than some commonly used models

in continuum mechanics, such as the Navier-Stokes equations or the classical thin film model.

## 5.1 Introduction and background

For more than two decades there has been interest in surface nanobubbles, which can form when a hydrophobic surface is fully immersed in liquid [68, 69, 70, 71]. Due to the high Laplace pressure inside a hemispherical cap shaped nanobubble, we might expect the gas inside to dissolve and diffuse away in microseconds [72]. However, in reality they can sometimes remain stable for many hours or even up to days [69, 70, 73, 74].

The existence of surface nanobubbles at the solid-liquid interface plays a significant role in a number of chemical and physical processes, such as flotation in mineral processing [75], design of microdevices [76] and drug delivery to cancer cells [77]. As well as the wide range of applications, there are also theoretical challenges to understanding the fundamental physical properties of nanobubbles which has also attracted the attention of many scientists.

These surface nanobubbles contain air molecules that have come out of solution in the liquid, and are not purely filled with the vapour phase. To properly describe such a system, one must treat the full two component system of solvent liquid and solute air molecules. However, as a precursor to tackling the full binary mixture problem, the situation that must be first understood is that of the pure liquid and the properties of nanobubbles of the vapour that may appear between the liquid and a solid surface. It is this aspect that we discuss in the present chapter.

Our approach is to use a microscopic (i.e. particle resolved) classical density functional theory (DFT) [26, 38] based method to calculate a coarse grained effective interfacial free energy (often called the binding potential, which is defined in previous sections)

for vapour nanobubbles. Since DFT is an accurate theory for the spatial variations in the particle density, it thereby incorporates the effects of vapour compressibility, which are believed to be important for nanobubbles. There are, of course, other computer simulation methods where this can be done [57, 78, 79, 80]. The resulting binding potential is then incorporated into a mesoscopic interfacial free energy functional for determining the height profile of the nanobubbles. This also allows us to calculate the total free energy of such a nanobubble and how it depends on the interaction potential between the surface and the fluid particles, thereby allowing us to estimate the relative probabilities for observing nanobubbles as a function of size and surface properties.

To study nanobubbles, in Ref. [81] a simple approximate form for the binding potential  $g(h)$  was postulated, since although much can be inferred about the qualitative form of  $g(h)$  from various considerations [1, 17, 19], its precise form is not known exactly. The model of Ref. [81] includes contributions to  $g(h)$  due to the van der Waals forces. Our approach here is to develop a model for vapour nanobubbles at equilibrium, based on calculating the binding potential  $g(h)$  using DFT for all values of  $h$ , that can then be used as an input to the IH model. Since DFT incorporates the effects of the compressibility of the vapour, these effects are also incorporated into  $g(h)$  when it is calculated using our approach. The system we model here is a very small bubble of vapour located on a planar solid surface that is in contact with a bulk liquid as illustrated in Fig. 1.3(b). The height of the liquid-vapour interface is defined to be at  $h(x, y)$  above the surface, where  $(x, y)$  is the position on the surface.

To develop an understanding of such a bubble,  $h(x, y)$  is a key quantity to be determined, as is the contact angle the liquid-vapour interface makes with the substrate. This, via Young's equation [1], is related to thermodynamic quantities, namely the three interfacial tensions:  $\gamma_{lv}$ ,  $\gamma_{sl}$  and  $\gamma_{sv}$ , which are the liquid-vapour, solid-liquid and solid-vapour interfacial tensions, respectively. Of course, for larger bubbles  $h(x, y)$  is of



the shape of a hemispherical cap, because this minimises the area of the liquid-vapour interface and so also the free energy of the system. However, near the contact line (i.e. where the three phases meet) there is an additional contribution to the free energy from the binding (or interfacial) potential  $g(h)$ , which results from molecular interactions. This influences the shape of  $h(x, y)$  near the contact line and for nanobubbles is particularly important and can influence the overall shape of  $h(x, y)$ . The contribution to the pressure within the bubble can be expressed in terms of the Derjaguin (or disjoining) pressure  $\Pi(h) = -\partial g(h)/\partial h$  [1] and its effects can be observed experimentally [82].

This chapter is structured as follows: In Sec. 5.2 we describe briefly the DFT based method we apply for calculating  $g(h)$  for vapour films adsorbed between a planar wall and a bulk liquid. Then, in Sec. 5.3 and Sec. 5.4, we introduce the model fluid that we consider, the approximate DFT used to treat this fluid and the various different wall potentials that we consider. In Sec. 5.5 we present results for  $g(\Gamma)$ , for various different wall potentials and how the decay form of the wall potential moving away from the wall influences the decay form of  $g(\Gamma)$ . Following this, in Sec. 5.6 we input the obtained binding potentials into the interfacial Hamiltonian (1.3.9), in order to determine vapour nanobubble height profiles and their free energies. Finally, in Sec. 5.7 we draw our conclusions.

## 5.2 DFT approach to calculate $g(\Gamma)$

Elements of this section repeat key formulae and definitions from earlier chapters but are included to allow the reader to follow this chapter in a reasonably self-contained manner. In DFT [26, 38] we find that the grand potential  $\Omega$  is the following functional

of the fluid density profile  $\rho(\mathbf{r})$ :

$$\Omega[\rho(\mathbf{r})] = \mathcal{F}[\rho(\mathbf{r})] + \int \rho(\mathbf{r})(V_{ext}(\mathbf{r}) - \mu)d\mathbf{r}, \quad (5.2.1)$$

where  $V_{ext}(\mathbf{r})$  is the external potential felt by a single particle at position  $\mathbf{r}$  (i.e. the potential due to the solid substrate in the treatment here),  $\mu$  is the chemical potential and

$$\mathcal{F}[\rho(\mathbf{r})] = k_B T \int \rho(\mathbf{r})(\ln[\Lambda^3 \rho(\mathbf{r})] - 1)d\mathbf{r} + \mathcal{F}_{ex}[\rho(\mathbf{r})] \quad (5.2.2)$$

is the intrinsic Helmholtz free energy. The first term is the ideal-gas contribution and  $\mathcal{F}_{ex}$  is the excess part due to the interactions between the fluid particles. In the ideal-gas part,  $k_B$  is Boltzmann's constant,  $T$  is the temperature and  $\Lambda$  is the thermal de Broglie wavelength. The equilibrium fluid density profile is that which minimises  $\Omega[\rho(\mathbf{r})]$ , i.e. it satisfies the Euler-Lagrange equation

$$\frac{\delta \Omega}{\delta \rho(\mathbf{r})} = k_B T \ln[\Lambda^3 \rho(\mathbf{r})] + \frac{\delta \mathcal{F}_{ex}}{\delta \rho} + V_{ext}(\mathbf{r}) - \mu = 0. \quad (5.2.3)$$

This equation may be rearranged to obtain

$$\rho(\mathbf{r}) = \Lambda^{-3} \exp \left( \beta \left[ \mu - \frac{\delta \mathcal{F}_{ex}}{\delta \rho} - V_{ext}(\mathbf{r}) \right] \right), \quad (5.2.4)$$

where  $\beta = (k_B T)^{-1}$ . This is the form usually used for solving DFT numerically using a Picard iterative process [33, 41].

A typical series of the constrained density profiles calculated using this procedure are displayed in Fig. 5.1(a). These results are for the model fluid defined below, with fixed wall attraction strength. Fig. 5.1(b) shows the corresponding binding potential  $g(\Gamma)$ . The global minimum occurs at a small negative value of the adsorption, which

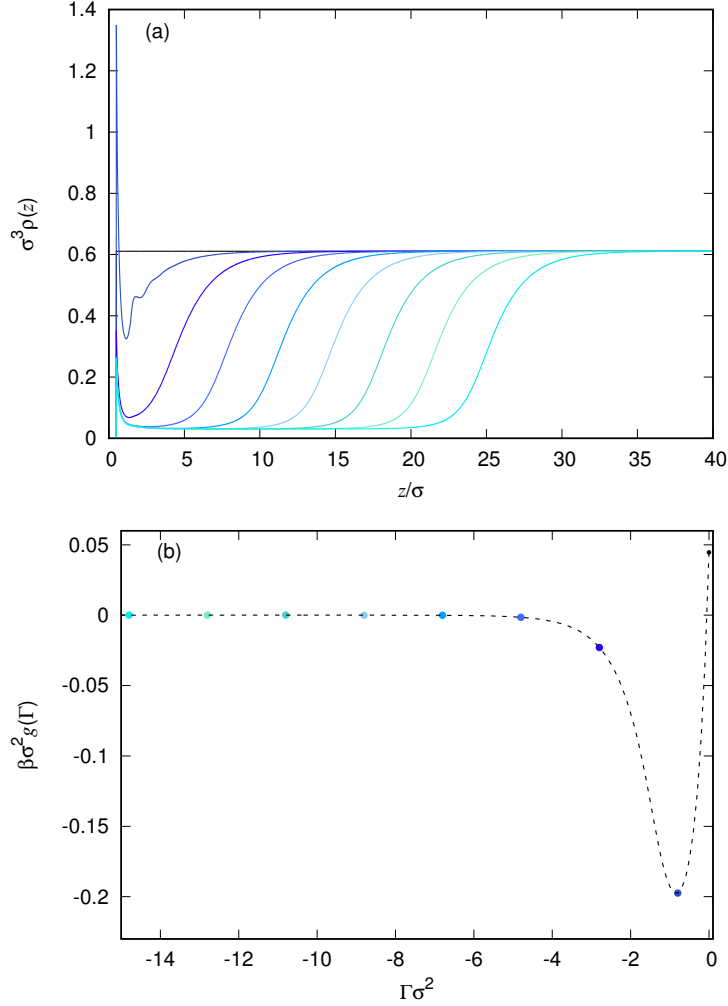


Figure 5.1: (a) A sequence of density profiles with decreasing adsorption corresponding to increasing thickness films of vapour between a wall and the bulk liquid. The adsorption values for each are  $\Gamma\sigma^2 = -0.0, -0.8, -2.8, -4.8, -6.8, -8.8, -10.8, -12.8$  and  $-14.8$ , where  $\sigma$  is the diameter of the cores of the particles. The strength of the attraction between the fluid particles is  $\beta\epsilon = 0.5$ , with range  $\lambda = \sigma$ , and the system is at vapour-liquid coexistence, with  $\mu = \mu_{coex}$ . The wall potential is that in Eq. (5.4.1), with  $\beta\epsilon_w^{(Y)} = 1.817$  and  $\lambda_w^{(Y)}/\sigma = 1$ . (b) The resulting binding potential, with the points on the curve corresponding to the sequence of density profiles displayed in (a).

corresponds to a partially drying liquid. In the density profiles there is peak near to the wall, corresponding to some particles being adsorbed preferentially at a particular distance from the surface of the wall. In the second density profile, which corresponds to the minimum in the binding potential, there are some oscillations near the wall, due to packing effects of the particles. As the adsorption becomes increasingly negative, there is an increasingly thick film of the vapour near the wall, and also as the thickness increases, the vapour density in the film becomes closer to that of the vapour at bulk vapour-liquid coexistence.

### 5.3 Model fluid

The model fluid that we consider consists of a system of particles interacting via a pair potential that can be split as follows:

$$v(r) = v_0(r) + v_1(r), \quad (5.3.1)$$

where  $r$  is the distance between the centres of the pairs of particles and  $v_0(r)$ , the repulsive-core part of the potential, is treated via the hard-sphere potential

$$v_0(r) = \begin{cases} \infty & \text{if } 0 < r \leq \sigma, \\ 0 & \text{if } \sigma < r, \end{cases} \quad (5.3.2)$$

where  $\sigma$  is the diameter of the cores of the particles. We model the attractive part of the potential  $v_1(r)$  via the following Yukawa potential

$$v_1(r) = \begin{cases} -\epsilon & \text{if } 0 < r \leq \sigma, \\ \frac{-\epsilon \exp(-(r-\sigma)/\lambda)}{r/\sigma} & \text{if } \sigma < r, \end{cases} \quad (5.3.3)$$

where  $\epsilon$  is the magnitude of interaction,  $\lambda$  is the parameter measuring the range of the attractive tail.

We make a standard approximation, and treat the contribution to the free energy from the hard-sphere repulsions via fundamental measure theory (FMT) DFT and the attractive part via a van der Waals mean field like contribution [26, 38, 31, 32, 41, 42], that is nonetheless fairly accurate [48]. In this case we can assume that the excess intrinsic Helmholtz free energy  $\mathcal{F}_{ex}$  can be approximated as follows:

$$\mathcal{F}_{ex}[\rho(\mathbf{r})] = \mathcal{F}_{hs} + \frac{1}{2} \iint \rho(\mathbf{r}_1) \rho(\mathbf{r}_2) v_1(|\mathbf{r}_1 - \mathbf{r}_2|) d\mathbf{r}_1 d\mathbf{r}_2, \quad (5.3.4)$$

where  $\mathcal{F}_{hs} = \int \Phi(\{n_\alpha\})$  is the hard-sphere contribution to the excess free energy, that we treat using Rosenfeld's original version of FMT and described in Chap. 3.2 [42]. There are more modern FMTs such as the White-Bear version and the 2D FMT for hard disks, that are more accurate when the fluid density is high and approaching freezing, but for the present study, Rosenfeld is sufficiently accurate.

## 5.4 External potential due to the wall

We assume that the planar solid substrate exerts an external potential on the fluid that varies in only one Cartesian direction, along the  $z$ -axis, which is perpendicular to the

plane of the substrate. Having chosen to model the fluid particle-particle interactions via the Yukawa pair potential in Eq. (5.3.3), an obvious choice for the potential between the particles and the wall is also a Yukawa:

$$V_{ext}^{(Y)}(z) = \begin{cases} \infty & \text{if } z < \frac{\sigma}{2} \\ \frac{-\epsilon_w^{(Y)} \exp(-z/\lambda_w^{(Y)})}{z/\sigma} & \text{if } z \geq \frac{\sigma}{2}, \end{cases} \quad (5.4.1)$$

where the parameters  $\epsilon_w^{(Y)}$  and  $\lambda_w^{(Y)}$  determine the strength of the attraction to the wall and the range, respectively.

We also consider the behaviour of the fluid in the presence of a wall with a  $z^{-3}$  power-law form for the decay of the attractive part of the potential. Such a potential can be viewed as originating from the  $r^{-6}$  decay form of the potential due to dispersion interactions that is found in e.g. the Lennard-Jones (LJ) model pair potential [38]. If one assumes a semi-infinite wall of uniform density and then integrates over the total attractive contribution due to the wall, treating all the elements as interacting with a given fluid particle with a potential decaying  $\propto r^{-6}$ , then the resulting form is (see e.g. Ref. [83])

$$V_{ext}^{(LJ)}(z) = \begin{cases} \infty & \text{if } z < \frac{\sigma}{2}, \\ \frac{-\epsilon_w^{(LJ)}}{(z/\sigma)^3} & \text{if } z \geq \frac{\sigma}{2}, \end{cases} \quad (5.4.2)$$

where the parameter  $\epsilon_w^{(LJ)}$  defines the strength of the attraction in this potential. Another wall potential that we consider is one with a short-ranged attraction, decaying with a Gaussian form [84]

$$V_{ext}^{(G)}(z) = \begin{cases} \infty & \text{if } z < \frac{\sigma}{2} \\ -\epsilon_w^{(G)} \exp\left(-(z/\lambda_w^{(G)})^2\right) & \text{if } z \geq \frac{\sigma}{2}, \end{cases} \quad (5.4.3)$$

where the parameters  $\epsilon_w^{(G)}$  and  $\lambda_w^{(G)}$  define the strength and range of this potential. Finally, we also consider a wall potential that has exponential decay

$$V_{ext}^{(E)}(z) = \begin{cases} \infty & \text{if } z < \frac{\sigma}{2} \\ -\epsilon_w^{(E)} \exp\left(-z/\lambda_w^{(E)}\right) & \text{if } z \geq \frac{\sigma}{2}, \end{cases} \quad (5.4.4)$$

with parameters  $\epsilon_w^{(E)}$  and  $\lambda_w^{(E)}$  determining the strength and range of the potential. The reason that we consider all these different potentials is that the form of the decay as  $z \rightarrow \infty$  influences the form of the decay of  $g(h)$  for  $h \rightarrow \infty$  [17, 84], as we also show below.

All our calculations of density profiles are performed on a regular grid with  $2^{14}$  points and a grid spacing  $dz = 0.01\sigma$ , so that the total domain length is  $164\sigma$ . This has the wall at one end of the system and a section at the other end with  $\rho(z) = \rho_l$  (i.e. the bulk density boundary condition), followed by a section where  $\rho(z) = 0$  (roughly 10% of the domain), to provide padding for the fast Fourier transforms used to evaluate the convolution integrals. For more details on how to calculate density profiles using DFT see Chap. 2 and Ref. [41].

## 5.5 Results for the binding potential

We calculate the binding potentials  $g(\Gamma)$  for a range of different values of the adsorption  $\Gamma$  using the procedure described above in Sec. 5.2, for the various different wall potentials given in the previous section and for varying values of the attraction strength parameter.

In Fig. 5.2 are results for the Yukawa wall potential (5.4.1) and in Fig. 5.3 are results for the LJ-like wall potential (5.4.2). We see that in both cases, when the solid substrate

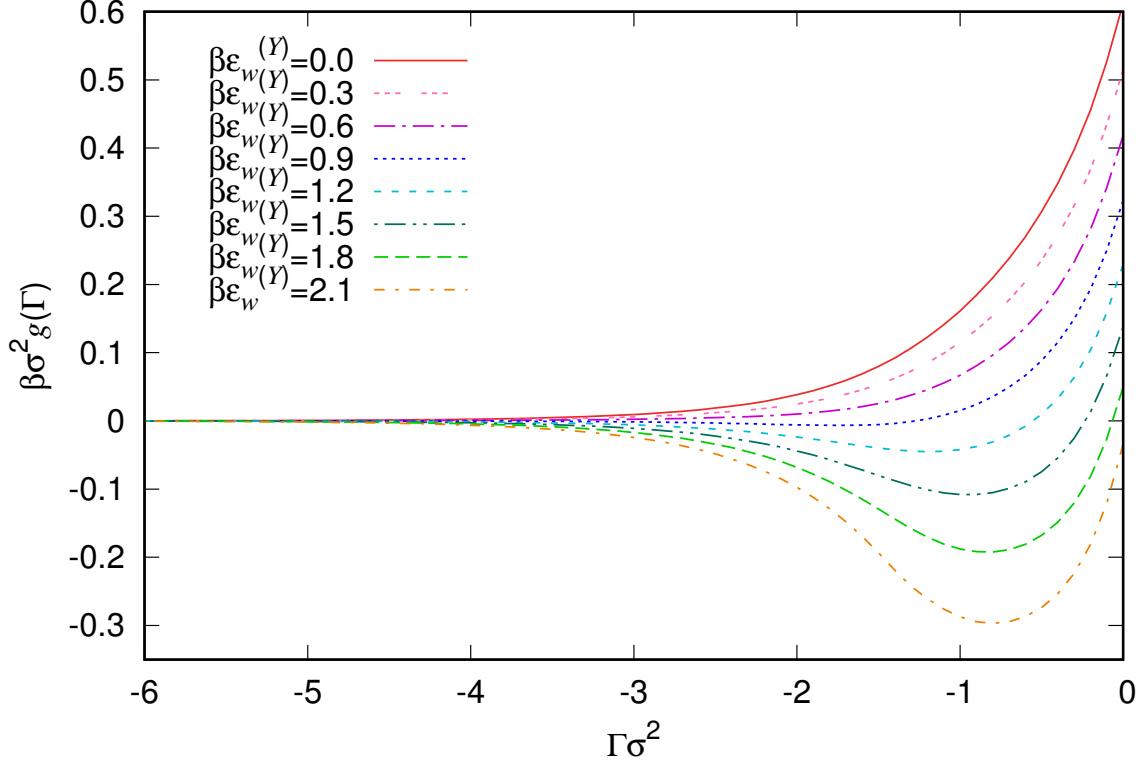


Figure 5.2: A sequence of binding potentials  $g(\Gamma)$ , for varying wall attraction strength. The fluid pair interactions have  $\beta\epsilon = 0.5$  and  $\lambda/\sigma = 1$ . The results are for the Yukawa wall potential (5.4.1), for varying  $\beta\epsilon_w^{(Y)}$  as given in the key.

is very weakly attractive, the global minimum of  $g(\Gamma)$  is at  $\Gamma \rightarrow -\infty$ , corresponding to drying of the fluid from the wall being the equilibrium state of the system. For the more attractive substrates, the global minimum of the binding potentials is at a small negative value of the adsorption, which corresponds to the partial-drying situation. Our results are consistent with previous DFT predictions that the drying transition for these types of systems is a continuous (critical) transition – see Ref. [20] and references therein for an excellent recent discussion of this. It is interesting to note that this minimum



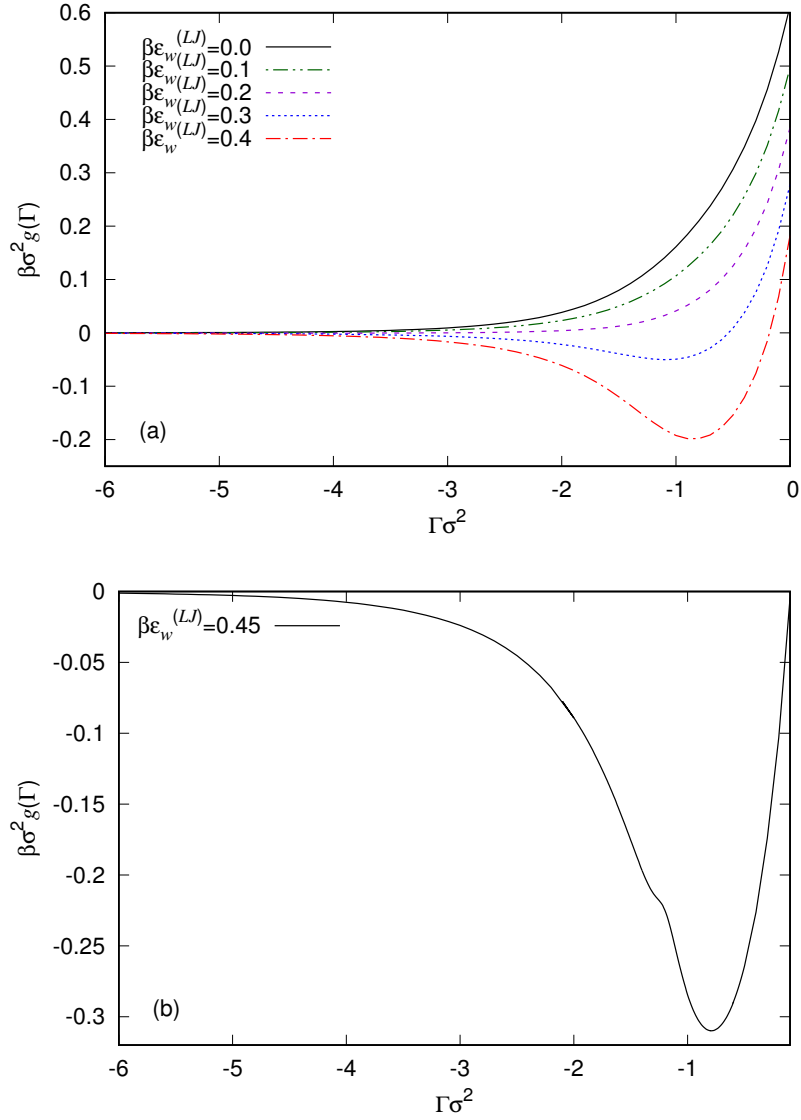


Figure 5.3: In (a) we display results for the LJ-like wall (5.4.2) with varying  $\beta \epsilon_w^{(LJ)}$ , whilst (b) shows the binding potential for the strongly attractive wall with  $\beta \epsilon_w^{(LJ)} = 0.45$ . In all except this last case the binding potentials are smooth and featureless, but in this case some small amplitude oscillations can be seen in  $g(\Gamma)$ .

in  $g(\Gamma)$  is fairly broad and the binding potentials are rather smooth and featureless, despite the density profiles which go into calculating these having significant structure near the wall – see Fig. 5.1. The width of the minimum in  $g(\Gamma)$  is certainly broader than the typical minima obtained in Ref. [6] for the case of liquid films adsorbed at a wall with the bulk phase being the vapour. We believe this is due to the fact that when there is the tendency towards drying at a solvophobic interface, there can be significant interfacial fluctuations [85, 86, 87, 88, 20, 83] and so in these cases any minima in  $g(\Gamma)$  are fairly broad.

In Fig. 5.3(b) we show the binding potential for a more strongly attracting wall, with  $\beta\epsilon_w^{(LJ)} = 0.45$ . In this case, the liquid is more strongly attracted to the wall and so we see more layered packing effects at the wall in the corresponding density profiles. In cases like this, convergence of the numerics become more difficult, because the system does not want the vapour phase at the wall, since the liquid is energetically much more favourable. We also see in this situation the appearance of some small amplitude oscillations in the binding potential, stemming from particle layering at the wall.

In Fig. 5.4(a) we compare four binding potentials corresponding to the four different external potentials defined in Sec. 5.4, with the wall potential attraction strength parameters chosen so that they all have the same minimal value of  $g(\Gamma_0)$ . Since the vapour-liquid interfacial tension  $\beta\sigma^2\gamma_{lv} = 0.603$  is the same in all cases, this means that these all correspond to the same macroscopic contact angle, because they all have the same minimum value of  $g(\Gamma_0)$  – see Eq. (3.6.12). It is interesting to note that the width of the potential minimum in  $g(\Gamma)$  is not the same for each of these different wall potentials. This means the precise form of the external potential due to the wall is important for controlling the amplitude of interfacial fluctuations near the wall. We also see that the form of the external potential controls significantly the way  $g(\Gamma)$  decays as  $\Gamma \rightarrow -\infty$ . This can be seen even more clearly in Fig. 5.5 where we instead plot

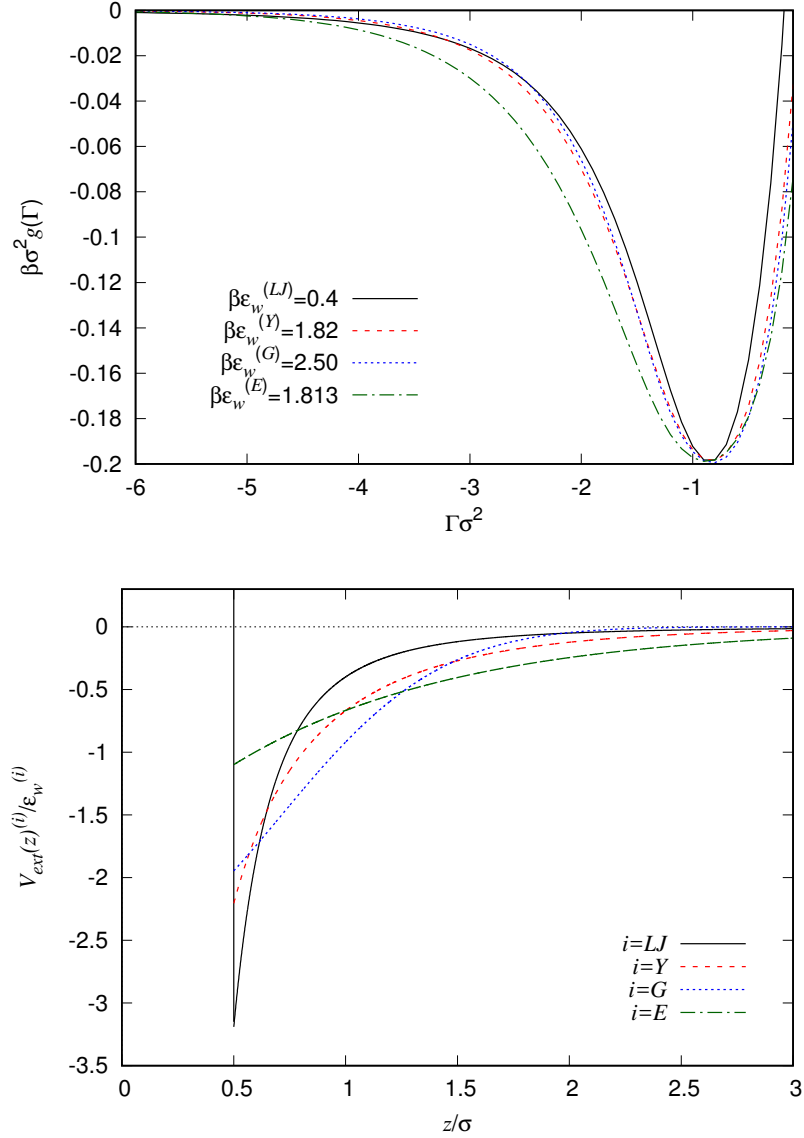


Figure 5.4: In panel (a) we show a comparison of the binding potentials corresponding to the four different external potentials defined in Sec. 5.4. The bulk fluid is the same in all cases, with  $\beta\epsilon = 0.5$  and  $\lambda/\sigma = 1$ . The parameters are chosen as given in the key and with  $\lambda_w^{(Y)} = \lambda_w^{(G)} = \lambda_w^{(E)} = \lambda$  (all the same), so that they all have the same minimal value of  $g(\Gamma_0)$  and therefore also the same macroscopic contact angle. In panel (b) we display plots of the corresponding four different wall potentials.

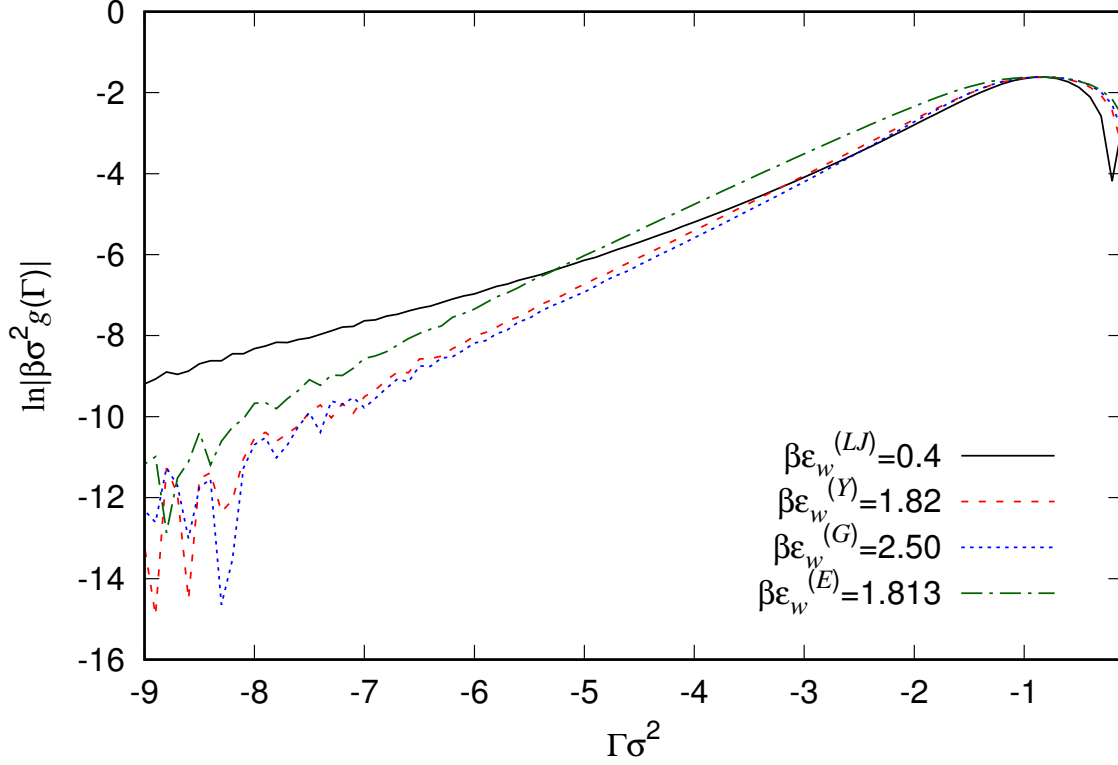


Figure 5.5: The same binding potentials as displayed in figure 5.4(a), except here we instead plot  $\ln |g(\Gamma)|$  versus  $\Gamma$ .

$\ln |g(\Gamma)|$  versus  $\Gamma$ , which allows to observe more clearly the form of the asymptotic decay. The form of the asymptotic decay of binding potentials is discussed extensively in Refs. [17, 19, 89], and these results largely carry over to the case of drying at interfaces – see Ref. [20]. As one should expect, the slowest decay is for the LJ-like wall potential (5.4.2), since this has a power-law decay for  $z \rightarrow \infty$ . For the other three wall potentials the binding potential decays exponentially, so that when we plot  $\ln |g(\Gamma)|$ , we see in Fig. 5.5 a straight line. We see that for  $\Gamma\sigma^2 < -2$  the gradient is roughly the same for all three. This is because at this particular state point the correlation length in the

vapour phase  $\xi_v \approx \sigma = \lambda$ , i.e. is very similar in value to the decay length of the wall potentials (5.4.1) and (5.4.4). For short-ranged wall-fluid and fluid-fluid potentials one should expect the binding potential to decay for  $h \rightarrow \infty$  as [17, 19, 84, 20]

$$g(h) = a \exp(-h/\xi_v) + \dots \quad (5.5.1)$$

where  $a$  is a constant and “ $\dots$ ” denotes faster decaying terms. So in this case, when one plots  $\ln |g(\Gamma)|$ , for large  $\Gamma$  one sees a straight line with gradient equal to  $-1/[\xi_v(\rho_v - \rho_l)]$ . On the other hand, if there is an exponentially decaying wall potential (5.4.4), then one instead has [84]

$$g(h) = a \exp(-h/\xi_v) + b \exp(-h/\lambda_w^{(E)}) + \dots, \quad (5.5.2)$$

where  $b$  is a constant, so whichever is bigger out of  $\xi_v$  and  $\lambda_w^{(E)}$  determines the ultimate decay of  $g(h)$  for  $h \rightarrow \infty$ . When the wall potential has a Yukawa decay like in Eq. (5.4.1), then this can also determine the decay of  $g(h)$ , somewhat like in Eq. (5.5.2), except with a renormalised decay length [84]. Note that for larger negative values of the adsorption the binding potential  $g(\Gamma)$  becomes small and so on the logarithmic scale in Fig. 5.5 one sees the numerical round-off errors, appearing as random fluctuations with increasing amplitude as  $\Gamma \rightarrow -\infty$ .

It is also interesting to note in Fig. 5.4(a) that all of the binding potentials have a finite value for  $g(\Gamma \rightarrow 0)$ , but the values of  $g(0)$  for the different wall potentials are all very different and in particular the result corresponding to the LJ wall is much higher. We believe the origin of this difference is the fact that the LJ wall potential Eq. (5.4.2) has a deeper (but more narrow) potential minimum for  $z \rightarrow \sigma/2^+$  than the other wall potentials, as can be seen in Fig. 5.4(b). This is also supported by the fact that the values of  $g(0)$  are ordered in magnitude in the same order as the values

of the wall potentials at contact,  $V_{ext}^{(i)}(z \rightarrow \sigma/2^+)$ . That the value of  $g(0)$  must be finite was discussed in the context of liquid droplets at surfaces in Refs. [4, 6]. Indeed,  $g(\Gamma)$  remains finite even for small positive values of  $\Gamma$ , which corresponds to a negative excess of vapour being adsorbed at the wall. However, the fact that  $g(0)$  remains finite should not significantly affect the behaviour at the contact line, since the value at the minimum  $g(\Gamma_0)$  is far more important than the value  $g(0)$  in determining contact line properties.

In Fig. 5.6 we display a set of binding potentials for the exponential wall potential Eq. (5.4.4), calculated for varying wall potential decay length  $\lambda_w^{(E)}$ . Increasing the range for fixed  $\epsilon_w^{(E)}$  increases the overall integrated strength of the wall potential and so, of course, makes the liquid more favourable at the wall and the vapour less favourable. This is manifest in the increasingly deep minimum in  $g(\Gamma)$ , as  $\lambda_w^{(E)}$  is increased. In Fig. 5.7 we plot  $\ln |g(\Gamma)|$ , which allows one to see the crossover from the first term on the right hand side of Eq. (5.5.2) dominating the decay of  $g(\Gamma)$ , to the second term dominating, for larger  $\lambda_w^{(E)}$ .

In the following section we take the binding potentials that we have calculated using DFT and input them into the IH (1.3.9) in order to determine vapour nanobubble height profiles. To do this we fit the binding potential to obtain an analytic form which can then be input easily. The form we use is (c.f. Eq. (5.5.2) and also Refs. [4, 6]):

$$g(\Gamma) = a_1 e^{\frac{\Gamma}{l_0}} + a_2 e^{\frac{2\Gamma}{l_0}} + a_3 e^{\frac{3\Gamma}{l_0}} + \dots \quad (5.5.3)$$

where  $l_0$ ,  $a_1$ ,  $a_2$ ,  $a_3$ , etc, are parameters to be fitted. The values obtained for these parameters for all of the binding potentials displayed in this thesis are given in Table B.1 in the Appendix B. Recall that  $\Gamma$  is normally a negative quantity in Eq. (5.5.3).

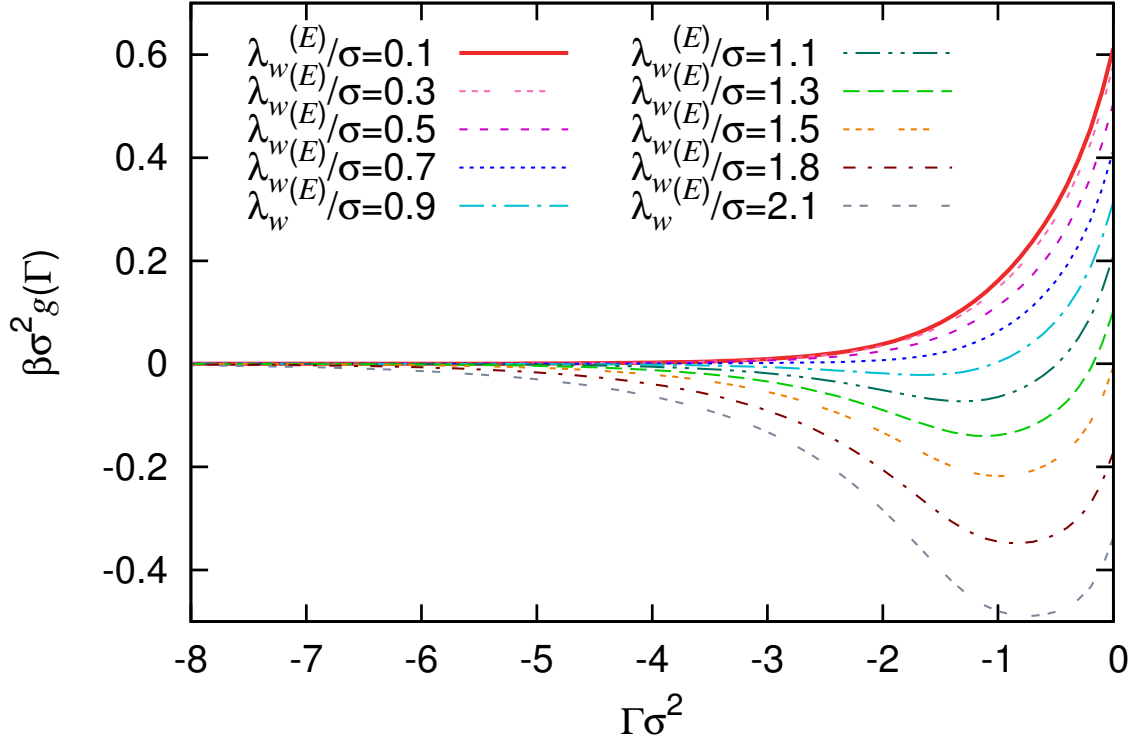


Figure 5.6: A series of binding potentials for the exponential wall potential (5.4.4) with varying  $\lambda_w^{(E)}$  and fixed  $\beta\epsilon_w^{(E)} = 1$ . The fluid pair interactions have  $\beta\epsilon = 0.5$  and  $\lambda/\sigma = 1$ .

## 5.6 Vapour nanobubble profiles

In Fig. 5.8, we display a sequence of equilibrium vapour nanobubble height profiles  $h(x) = \Gamma(x)/(\rho_v - \rho_l)$ , calculated by minimising Eq. (1.3.9) together with binding potentials calculated using DFT. We do this for the fluid with interaction parameters  $\beta\epsilon = 0.5$  and  $\lambda/\sigma = 1$  at a series of walls with the Yukawa potential (5.4.1) with fixed  $\lambda_w^{(Y)}/\sigma = 1$  and various values of the wall attraction parameter  $\epsilon_w^{(Y)}$ .

In Eq. (1.3.9) we set the liquid-vapour interfacial tension  $\beta\sigma^2\gamma_{lv} = 0.603$ , the value we obtain from the DFT. We also assume for simplicity that the system is uniform

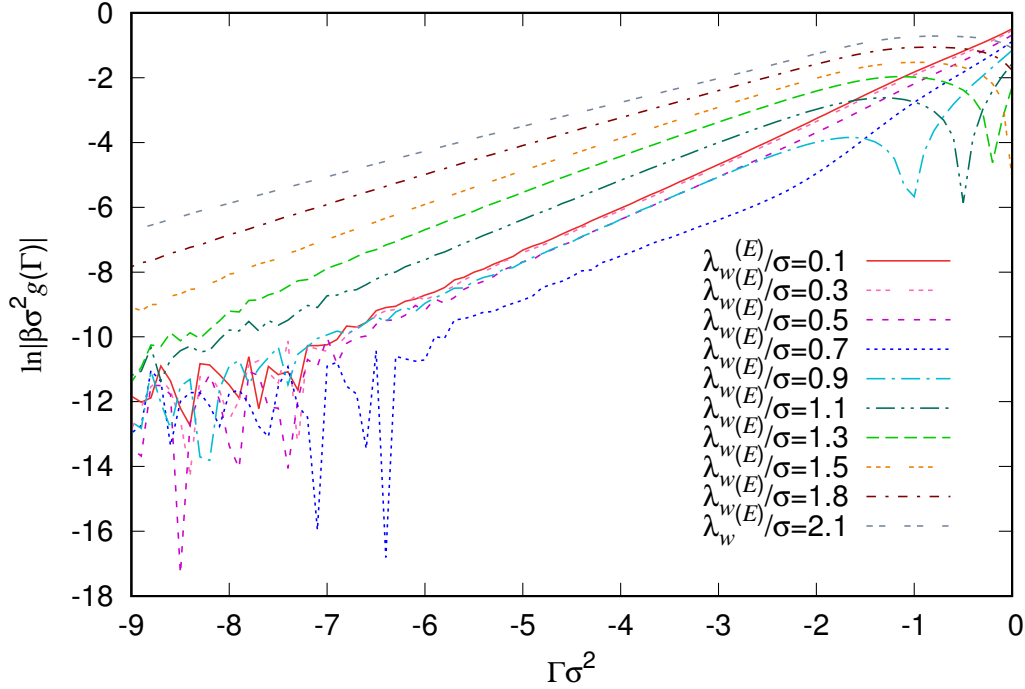


Figure 5.7: The same binding potentials as displayed in Fig. 5.6 for varying  $\lambda_w^{(E)}$ , but here we instead plot  $\ln|g(\Gamma)|$  versus  $\Gamma$ .

in the  $y$ -direction, so strictly speaking the profiles that we calculate are actually for ridge-shaped nanobubbles. However, we do not expect results from calculating radially symmetric height profiles (varying in both the  $x$ - and  $y$ -directions) to have cross-section height profiles qualitatively different from the ones we calculate here. We apply periodic boundary conditions  $h(x = 0) = h(x = L)$ , where  $L$  is the length of the domain. The height profiles in Fig. 5.8 all have the same area under the curve (i.e. the same total adsorption).

We numerically minimise the free energy (1.3.9) by solving the corresponding thin-film equation with disjoining pressure  $\Pi(h) = -\partial g/\partial h$  and converging to equilibrium, based on the approach of Ref. [55] which will be discussed in the next chapter. This



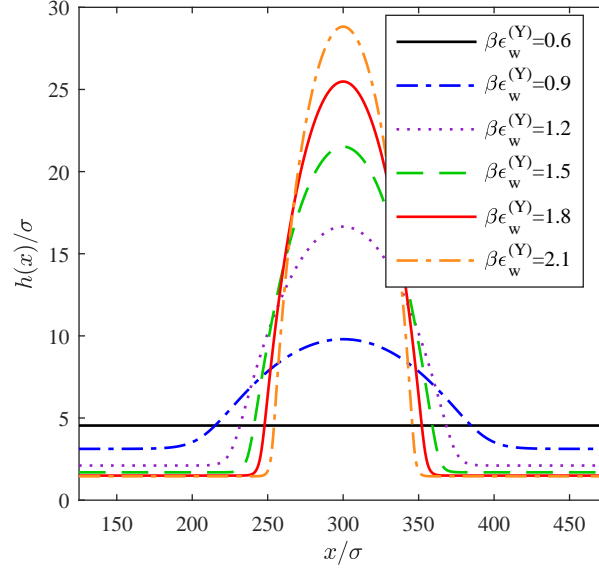


Figure 5.8: A series of equilibrium vapour nanobubble height profiles  $h(x) = \Gamma(x)/(\rho_v - \rho_l)$ , calculated by minimising Eq. (1.3.9) together with the binding potentials for the fluid with  $\beta\epsilon = 0.5$  and  $\lambda/\sigma = 1$  at the Yukawa wall (5.4.1), with fixed  $\lambda_w^{(Y)}/\sigma = 1$  and various values of the wall attraction parameter  $\epsilon_w^{(Y)}$ , as given in the key. The total area under all of the curves is  $2727\sigma^2$  and the length of the domain  $L = 600\sigma$ .

uses the method of lines, with finite difference approximations for the spatial derivatives and the *ode15s* Matlab variable-step, variable-order solver [90].

The initial guess to equilibrate from has a Gaussian shaped “bump” in it that breaks the symmetry and determines the final location of the nanobubble on the surface. In Fig. 5.8 we see that the vapour nanobubbles become more spread out over the surface as the attraction due to the wall is decreased. Then, for  $\beta\epsilon_w^{(Y)} = 0.6$ , there is a uniform thickness film of vapour on the substrate. This corresponds to the drying transition and it occurs at the value of  $\epsilon_w^{(Y)}$  that one must expect from inspecting the binding potential curves in Fig. 5.2(a), i.e. where the minimum in  $g(h)$  at a finite value of  $h$

disappears, which occurs by the minimum value diverging  $h \rightarrow \infty$ , since this drying transition is continuous (critical). For the profiles containing a nanobubble, the height of the vapour “precursor” film corresponds roughly to the value at the minimum in the binding potentials for the different values of  $\beta\epsilon_w^{(Y)}$ . However, in a finite size domain, the height is shifted slightly from the minimum value due to the Laplace pressure in the nanobubbles combined with the effects of mass conservation in our periodic domain. The excess pressure due to the presence of the nanobubble has two components,

$$\frac{\delta F_{\text{IH}}}{\delta h} = -\Pi(h(x)) - \kappa(h(x)), \quad (5.6.1)$$

where  $F_{\text{IH}}$  is given in Eq. (1.3.9),  $\Pi$  is the disjoining pressure and the curvature contribution is

$$\kappa = \gamma_w \nabla \cdot \left( \frac{\nabla h}{\sqrt{1 + (\nabla h)^2}} \right). \quad (5.6.2)$$

In Fig. 5.9 we display the values of these two contributions to the excess pressure as a function of position through a nanobubble, for the case where  $\beta\epsilon_w^{(Y)} = 1.5$ . The corresponding nanobubble height profile is displayed in Fig. 5.8. We see in Fig. 5.9 that these two pressure components vary significantly with  $x$ , in particular in the contact line region. Of course, the sum of these is a constant as this is the condition for equilibrium.

As an example of the type of multiscale interfacial phenomenon that our coarse grained model can be used to describe, we compute vapour nanobubble height profiles on a patterned heterogeneous surface. This consists of a surface divided into two regions with a different wettability on each of the two halves of the surface. We calculate the free energies for nanobubbles on each half, and from this we are able to determine the relative probabilities for finding vapour nanobubbles on each type of surface. We define

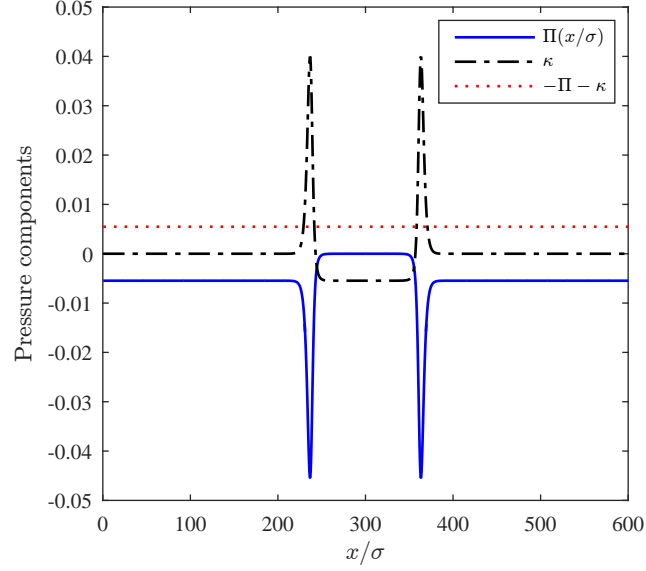


Figure 5.9: The components of the excess pressure,  $\Pi$  and  $\kappa$ , given by Eqs. (5.6.1) and (5.6.2), for a nanobubble with volume  $2727\sigma^2$  and wall attraction strength  $\beta\epsilon_w^{(Y)} = 1.5$ . The corresponding height profile is displayed in Fig. 5.8.

our position dependent binding potential as

$$g(x, h) = g_l(h)(1 - f(x)) + g_r(h)f(x), \quad (5.6.3)$$

where the smooth switching function

$$f(x) = \frac{1}{2} \left[ \tanh\left(\frac{x - L/2}{\mathcal{W}}\right) - \tanh\left(\frac{x - L}{\mathcal{W}}\right) \right] + \frac{1}{2} \left[ \tanh\left(\frac{x + L/2}{\mathcal{W}}\right) - \tanh\left(\frac{x}{\mathcal{W}}\right) \right], \quad (5.6.4)$$

where  $\mathcal{W} = \sigma$  determines the width of the smooth transition zone between the two halves of the surface. This function also satisfies our periodic boundary conditions.

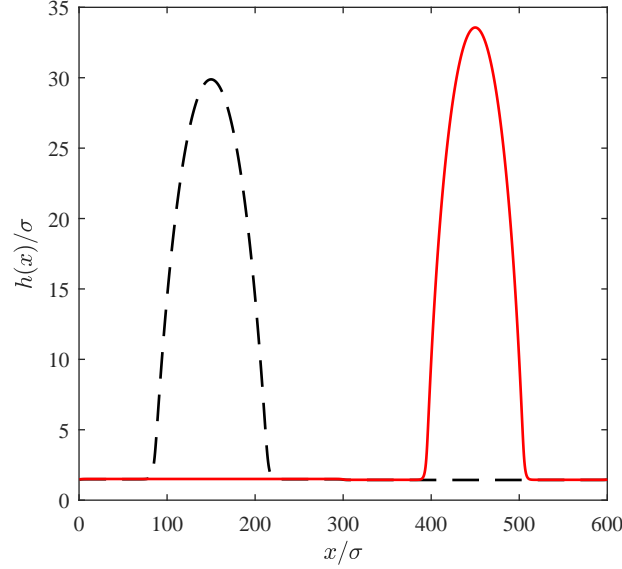


Figure 5.10: A comparison of two equilibrium vapour nanobubble profiles on a heterogeneous surface with position dependent binding potential (5.6.3). The external potential due to the wall has attraction strength  $\beta\epsilon_w^{(Y)} = 2.1$  on the right half of the system and  $\beta\epsilon_w^{(Y)} = 1.8$  on the left half. The total volume of vapour in the system is the same in both cases.

$g_l(h)$  and  $g_r(h)$  are the binding potentials on the left and right hand halves of the surface, respectively. These are calculated for the Yukawa wall with  $\lambda_w^{(Y)}/\sigma = 1$ . On the right we have  $\beta\epsilon_w^{(Y)} = 2.1$ , which represents a more solvophilic surface, whilst on the left we have a lower attraction parameter,  $\beta\epsilon_w^{(Y)} = 1.8$ , which represents a more solvophobic surface.

In Fig. 5.10 we display the height profiles for two different nanobubbles having the same volume  $V$  but each centred on the two different halves of the system. The total domain length is  $L = 600\sigma$ . The initial condition used to calculate each of these has the Gaussian bump centred at either  $x = L/4$  or  $x = 3L/4$ , in order to locate the centres

of the final equilibrium nanobubbles at these points. The left hand vapour nanobubble on the less attractive wall (smaller  $\epsilon_w^{(Y)}$ ) has the lower free energy. The free energy of the whole system  $F$  is calculated using Eq. (1.3.9) and in Fig. 5.11(a) we display results for  $F$  calculated as a function of  $V$ . In this figure these results are compared with those from a simple macroscopic (capillarity) approximation, described below. Using this data, in Fig. 5.11(b) we plot the quantity  $\beta(F_r - F_l)$  as a function of  $V$ , where  $F_l$  is the free energy for the nanobubble on the left and  $F_r$  when it is on the right. Since the probability of a given state  $i$  occurring  $P_i \propto e^{-\beta F_i}$ , we therefore have that the ratio of the probabilities for finding the nanobubble on the two different halves of the system  $P_r/P_l = e^{-\beta(F_r - F_l)}$ , i.e. the exponential of minus the quantity displayed in Fig. 5.11(b) is the relative probability. Since the left half of the surface is more solvophobic, we have  $P_l > P_r$ , and as the size of the nanobubbles increases, the probability of finding such a nanobubble on the more solvophobic half of the system becomes much more likely, with the relative probability,  $P_l \gg P_r$ . Note that the curves in Fig. 5.11 end on the left at a finite value of the volume  $V$ . This is because when the volume of vapour in the system is less than the end point value, the system can lower the total system free energy by having a uniform film thickness everywhere, at a value shifted slightly from the value at the minimum of  $g(h)$ , rather than by having most of the system with  $h$  at the minimum of  $g(h)$  but also retaining a bubble which has a larger interfacial contribution from curvature.

The macroscopic (capillarity) approximation that we compare our results with consists of setting the height profile of the vapour nanobubble to be an analytic piecewise function of  $x$ . We assume that outside of the nanobubble the film height is uniform: in the left half of the system we set  $h(x) = h_l$ , where  $h_l$  is the value at the minimum of the binding potential  $g_l(h)$  and in the right half we set  $h(x) = h_r$ , where  $h_r$  is the value at the minimum of  $g_r(h)$ . For the nanobubble itself, we assume the height profile is the

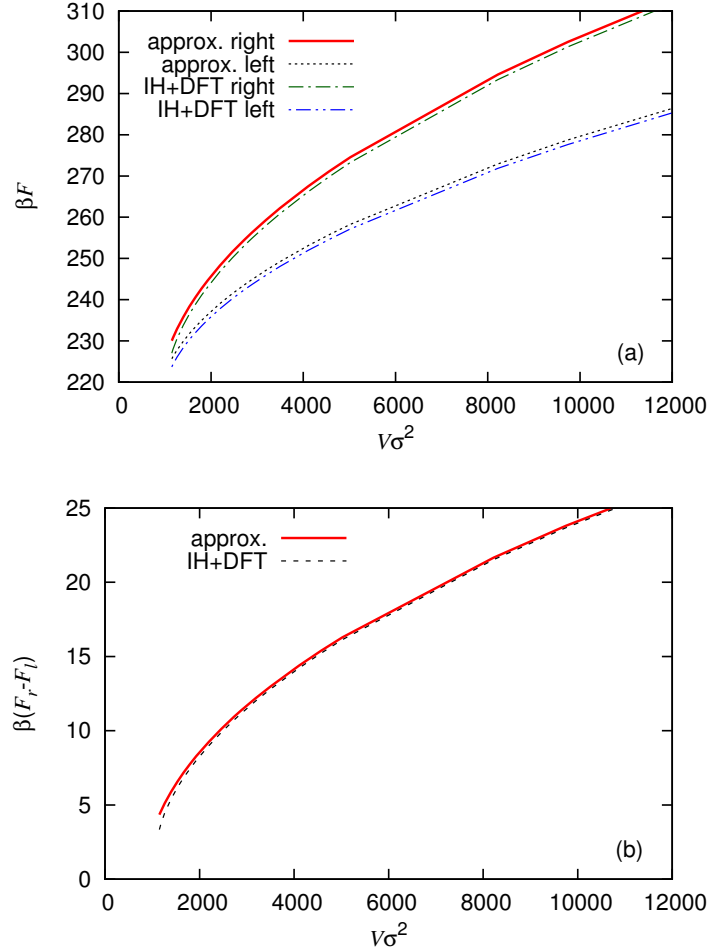


Figure 5.11: In panel (a) we display the free energy  $F$  as a function of the vapour nanobubble volume  $V$ , for a heterogeneous system with wall attraction  $\beta\epsilon_w^{(Y)} = 2.1$  on the right half of the surface and  $\beta\epsilon_w^{(Y)} = 1.8$  on the left. The labels “right” and “left” in the key denote on which side of the system the nanobubble is located – c.f. Fig. 5.10. We compare results calculated from Eq. (1.3.9) with the binding potentials obtained from DFT, which are labelled “IH+DFT” with results from a simple macroscopic approximation (5.6.7), labelled “approx.”. In panel (b) we plot the quantity  $\beta(F_r - F_l)$  as a function of  $V$ . The exponential  $e^{-\beta(F_r - F_l)}$  gives the ratio of the probabilities  $P_r/P_l$  of finding the nanobubble on the two sides. Since the left half of the surface is more solvophobic, we have  $P_l > P_r$ .

arc of a circle  $h(x) = h_{circ}(x) = h_c + \sqrt{R^2 - (x - x_c)^2}$ , where  $h_c$ ,  $x_c$  and  $R$  are constant coefficients to be determined that depend on the size and location of the nanobubble. If we denote the locations of the two nanobubble contact lines to be  $x = A$  and  $x = A + w$ , i.e.  $w$  is the width of the nanobubble, then  $x_c = A + w/2$  and we must have that at these two points, the height profile is continuous. So, when the nanobubble is on the left we have  $h(A) = h(A + w) = h_l$  and when it is on the right,  $h(A) = h(A + w) = h_r$ . The second condition that we apply on the circular arc part of the nanobubble profile is that the slope at both ends should be equal to the tangent of the contact angle,  $h'(A) = -h'(A + w) = -\tan \theta$ . With these conditions, it is straightforward to write the coefficients  $R$  and  $h_c$  as functions of  $A$  and  $w$ . When the nanobubble is on the left hand side, the volume (area under the profile) is:

$$V = h_l \left( \frac{L}{2} - w \right) + h_r \frac{L}{2} + \int_A^{A+w} h_{circ}(x) dx, \quad (5.6.5)$$

with an analogous formula for when it is on the right. This gives us an expression for  $V$  as a function of  $w$ . Or, equivalently, we can vary  $w$  and still obtain a series of nanobubble profiles for various values of  $V$ .

Using this height profile we can also obtain an approximation for the free energy  $F$ . The surface tension contribution depends on the length of the interface. This is easy to get for the straight line pieces and for the circular nanobubble section it depends on the arc length

$$s = \int_A^{A+w} \sqrt{1 + h'(x)^2} dx, \quad (5.6.6)$$

which is also straightforward to evaluate. We assume that there is only a contribution to  $F$  from the binding potential when the height profile is at the value at the minimum of  $g(h)$ . Putting all this together we obtain the following estimate for the total free

energy of the system when the vapour nanobubble is on the left hand side of the system

$$F_{\text{IH}}^{\text{approx.}} = g_l(h_l) \left( \frac{L}{2} - w \right) + g_r(h_r) \frac{L}{2} + \gamma_{lv}(s + L - w), \quad (5.6.7)$$

and an analogous expression when the nanobubble is on the right. The results plotted in Figs. 5.11 labelled “approx.” are obtained using Eq. (5.6.7). We see that there is fairly good agreement in Fig. 5.11(a) between Eq. (5.6.7) and the results from the full minimisation of Eq. (1.3.9); the difference is less than 1%. However, as Fig. 5.11(b) illustrates, even such small errors can make more of a difference when calculating quantities like  $(F_r - F_l)$  and so also the ratio  $P_r/P_l = e^{-\beta(F_r - F_l)}$ , demonstrating the importance of getting details right for this sort of calculation. This is particularly important for small nanobubbles. For example, when the nanobubble volume  $V\sigma^2 = 1400$ , we have  $e^{-\beta(F_r - F_l)} = e^{-5.9} \approx 0.0027$  via Eq. (5.6.7), but from the full minimisation of Eq. (1.3.9) we obtain  $e^{-\beta(F_r - F_l)} = e^{-5.4} \approx 0.0045$ ; i.e. there is a 60% difference between the two results for the relative probabilities  $P_r/P_l$ . Another important detail for these types of calculations is getting correctly the true overall shape of  $g(h)$ , since this makes a contribution to  $F$ , which is neglected in Eq. (5.6.7), coming from the contact line region of the nanobubble.

Another source of error in Eq. (5.6.7) worth highlighting is that we have assumed that the heights of the film away from the nanobubble are the values at the exact minima of the binding potentials  $g_l$  and  $g_r$ . Consequently, any additional vapour volume in the system is assumed to be in the nanobubble. In reality, as we see from results from minimising Eq. (1.3.9) and magnifying in the small  $h$  region, there is a balance between having the vapour in the small- $h$  flat layer and having it in the nanobubble. The Laplace pressure in the nanobubble makes it become a little smaller, transferring some of the vapour into the flat film and thereby raising the free energy contribution from these



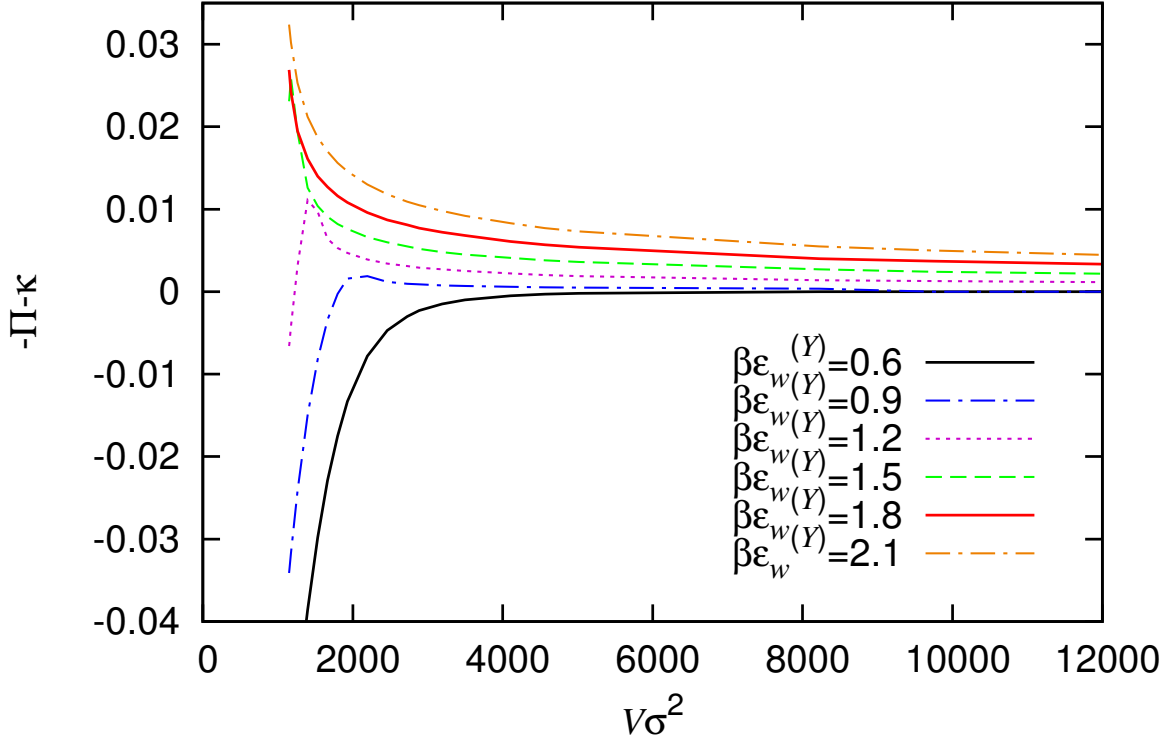


Figure 5.12: The excess pressure  $-\Pi - \kappa$ , given by Eq. (5.6.1), for a range of different nanobubble volumes and for values of the wall attraction strength parameter  $\beta\epsilon_w^{(Y)}$  as given in the key. See also Fig. 5.8.

portions of the system. There are also further sources of error due to the assumption that the nanobubble has a circular shape, in particular in the region near the contact lines where it would be expected to smoothly transition to the film heights, and in the error approximating the profile's transition across the wettability gradient as a sharp step.

In Fig. 5.12 we display  $(-\Pi - \kappa)$ , the excess pressure due to the presence of the nanobubble, given by Eq. (5.6.1), for a range of different nanobubble volumes and for a

range of different values of the wall attraction strength parameter  $\beta\epsilon_w^{(Y)}$ . Recall that the bulk fluid pressure is  $\beta\sigma^3p = 0.026$ , so the figure shows that these excess pressures are comparable in magnitude. For values of  $\beta\epsilon_w^{(Y)}$  smaller than that at the drying transition we see that for  $V \rightarrow \infty$ ,  $(-\Pi - \kappa) \rightarrow 0$  from below, whilst for  $\beta\epsilon_w^{(Y)}$  greater than that at the drying transition, then  $(-\Pi - \kappa) \rightarrow 0$  from above.

## 5.7 Concluding remarks

In this chapter we have presented results for the binding potential  $g(h)$  for films of vapour intruding between a bulk liquid and flat planar surfaces and used the calculated  $g(h)$  to determine film height profiles for vapour nanobubbles on the surface. The binding potentials are calculated using a microscopic DFT, applying the fictitious external potential method developed by Hughes *et al.* [4, 6], which is based on calculating a series of constrained fluid density profiles at the wall with varying thickness (adsorption). We see from our results in e.g. Fig. 5.4(a) that despite the resulting binding potentials being rather smooth and featureless, details such as the width of the minimum and the form of the decay in  $g(h)$  do depend crucially on the details of the microscopic interactions. We also see from our estimates of the relative probabilities of finding a nanobubble on different parts of a heterogenous surface that having a reliable approximation for  $g(h)$  is necessary for the estimates to be accurate. It is clear that to correctly describe vapour nanobubbles one must have an accurate binding potential. Here, we have used a microscopic DFT based on FMT to determine  $g(h)$ , although one could instead use computer simulations [57, 78, 79, 80]. However, the DFT calculations are computationally much faster than molecular dynamics simulations. Our DFT calculations take of order seconds to run, which is much less than the minutes or hours that molecular dynamics simulations take to run.

The overall coarse-graining procedure developed here, building on the work in Refs. [4, 6], allows us to determine multi-scale properties of fluids at interfaces. The approach allows to go from the microscopic features of the molecular interactions and go up in length scales to describe mesoscopic aspects such as nanobubbles on surfaces. Our approach has here been applied to a simple model heterogenous surface, but it could also be applied in a straight-forward manner to more complex surfaces and structures, since, for example, the contributions to  $g(h)$  from surface curvature are understood [13, 91].

In the work presented here we have assumed that it is just the vapour phase inside the nanobubbles. However, as mentioned in the introduction, perhaps the more experimentally relevant situation is when the nanobubbles also contain dissolved gas (i.e. air) molecules that have come out from solution in the bulk liquid. In Ref. [81] a theory for this situation is developed. The authors argue that one should set the binding potential in Eq. (1.3.9) to be the potential  $U(h) = w(h) - w(h_c) - \beta\mu_g h p_g(h)$ , where  $w(h)$  is the “bare” binding potential between the wall and the bulk liquid and the last term is the contribution from the gas in the nanobubble, that has chemical potential  $\mu_g$  and pressure  $p_g(h)$ , which is assumed to be related to the disjoining pressure and given by the ideal-gas equation of state. Whilst this approach has the advantage of being relatively simple, one could also include the effects of dissolved gas in the present approach by treating the system as a binary mixture and then using a DFT for the mixture to determine the influence of different amounts of the gas at the interface on  $g(h)$ . Such a DFT approach would, of course, include the effects of the gas compressibility, which are believed to be important for such surface nanobubbles.

Finally, we should remark that some of the values of the wall attraction parameter  $\epsilon_w^{(Y)}$  that we use are rather small, corresponding to very solvophobic surfaces. Considering simple molecular liquids at interfaces, such values are perhaps somewhat unrealistic,

being weaker than one would typically expect to find. For example, for water on hydrophobic surfaces such wax or Teflon, one does not see contact angles significantly greater than  $130^\circ$  [20]. However, at (patterned) superhydrophobic surfaces much larger contact angles are possible, so studying the behaviour of the model right up to the drying transition is relevant to such systems. Also, the model fluid considered here is also a reasonably good model for certain colloidal suspensions (e.g. colloid-polymer mixtures [92]) and for such systems even purely repulsive wall potentials are possible, when e.g. polymers are grafted onto the walls. The work here is highly relevant to such colloidal systems.

# Chapter 6

## Modelling Spreading of a Droplet

In the previous chapter, we applied the method developed in Ref. [6] to calculate the binding potential for films of vapour at interfaces and to determine important properties of nanobubbles. In this chapter we present a study of the spreading of liquid droplets on a solid substrate at very small scales. We focus on the regime where effective wetting energy (binding potential) and surface tension effects significantly influence steady and spreading droplets. In particular, we focus on strong packing and layering effects in the liquid near the substrate due to underlying density oscillations in the fluid caused by attractive substrate-liquid interactions. We show that such phenomena can be described by a thin-film (or long-wave or lubrication) model including an oscillatory Derjaguin (or disjoining/conjoining) pressure, and explore the effects it has on steady droplet shapes and the spreading dynamics of droplets on both, an adsorption (or precursor) layer and completely dry substrates. At the molecular scale, commonly used two-term binding potentials with a single preferred minimum controlling the adsorption layer height are inadequate to capture the rich behaviour caused by the near-wall layered molecular packing. The adsorption layer is often sub-monolayer in thickness, i.e.,

the dynamics along the layer consists of single-particle hopping, leading to a diffusive dynamics, rather than the collective hydrodynamic motion implicit in standard thin-film models. We therefore modify the model in such a way that for thicker films the standard hydrodynamic theory is realised, but for very thin layers a diffusion equation is recovered.

## 6.1 Introduction

The spreading of liquid droplets is a fascinating and highly consequential phenomenon which has received great attention for over a century [3, 93, 94, 21]. When a small volume of liquid is placed on a solid substrate, it can spread to form a hemispherical drop with a free surface and three-phase equilibrium contact angle  $\theta$ . This is referred to as partial wetting. However, if the liquid molecules are strongly attracted to the substrate the liquid spreads as much as it can, forming a pancake shaped ultrathin drop. This is referred to as complete wetting. This wetting behaviour influences phenomena that arise in everyday life, such as in the sliding of rain drops on windows or plant leaves, paint coating a wall or tear films in the eye [1]. As well as being a simple day to day process, static and dynamic wetting behaviour also influences many industrial processes. Critical applications such as coating, printing and lubrication have motivated many scientists to understand the evolution of thin liquid films and drops on substrates and to develop models for their dynamics [95, 21]. All these wetting phenomena are governed by surface and interfacial interactions that occur over length scales varying from the very small ( $\text{\AA}$ ) molecular distances to a few nm for van der Waals or electrostatic forces to the mesoscopic ( $\mu\text{m}$ ) scale for capillary forces. Understanding the interplay of all these interactions and their influence on the interfacial fluid dynamics and thermodynamics is at the core of understanding the behaviour and properties of droplets and thin liquid

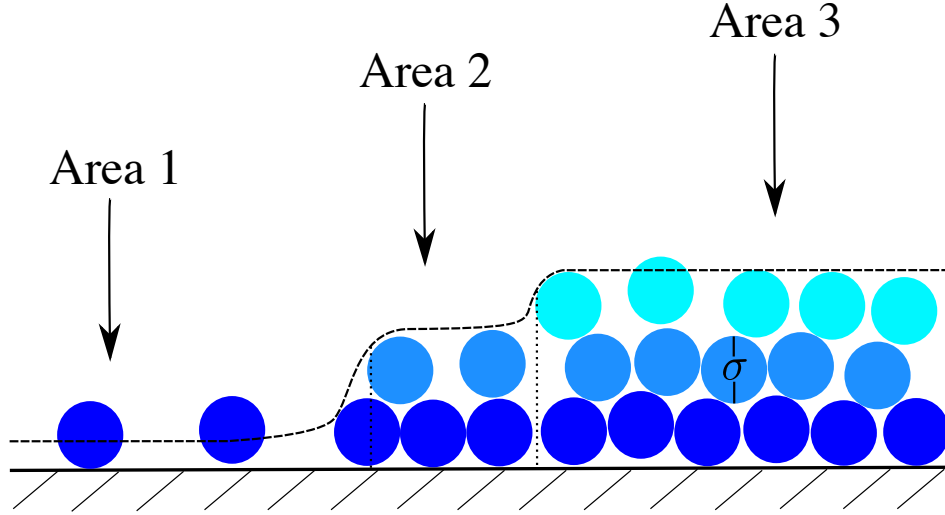


Figure 6.1: A sketch of the molecular configurations in a cross section through the contact line region of a drop of liquid which exhibits strong layering effects. The contact angle is  $\theta \approx 0$ . We identify three distinct regions, Areas 1-3, where the adsorption takes three distinct values due to the fact that when the substrate adsorption is low, the influence of molecular packing becomes important. The dashed line gives the corresponding effective film height. In Area 1, the amount adsorbed on the substrate is low, so the effective film height  $h \ll \sigma$ , the diameter of the molecules.

films on a solid substrate.

Here, we develop a thin-film model in the form of a partial differential equation (PDE) that describes the time evolution of the local amount of liquid on a substrate. It includes many aspects of the microscopic interactions between the liquid molecules and the substrate. When the cohesive forces between the molecules that form the liquid are short ranged compared to the size of the molecules  $\sigma$ , then strong layering at the substrate is possible, particularly at low temperatures [1, 96, 97, 98, 59, 99, 5, 6]. See also the molecular dynamics simulation results in Ref. [100].

Consider the contact line region of a drop of such a system, that is close to the

wetting transition, with  $\theta \approx 0^\circ$ . A sketch of a configuration of the molecules is displayed in Fig. 6.1. Three distinct regions, Areas 1–3 can be identified, based on the amount adsorbed. The thickness of the individual layers is approximately equal to the diameter of the liquid molecules,  $\sigma$ . In Area 1, there are just a few molecules adsorbed on the substrate, so the film height  $h \ll \sigma$ , as defined via Eq. (3.6.3). In Areas 2 and 3, the film height is roughly an integer number of molecular layers, since the strong intermolecular attractions favour complete layers. In Refs. [5, 6], density functional theory (DFT) for a simple model system was used to calculate the density distribution of a liquid at a substrate exhibiting this type of layered structure formation, which is remarkably similar to the terraced spreading drops observed in the experiments reported in [97]. In Refs. [5, 6], using the method developed in Ref. [4] the binding (or wetting) potential  $g(h)$  was also calculated as described in the previous chapters here. This binding potential  $g(h)$ , together with the interfacial tensions, gives the excess free energy for having a liquid film of thickness  $h$  adsorbed on the substrate (see Eq. (1.3.2)). It was found that in the types of situations sketched in Fig. 6.1, the binding potential is oscillatory.

In this chapter we consider the influence of such an oscillatory binding potential on the shape of steady drops and also on the dynamics of drop spreading. The established thin film models describe the advective motion<sup>1</sup> of the liquid over the substrate, sometimes also incorporating slip [21, 22]. However, normally, such models do not include the diffusive particle-hopping dynamics that one should expect when the adsorption is low [23, 24], such as in Area 1 in Fig. 6.1. Thus, we also develop here an augmented thin-film equation that incorporates this effect, with the principal aims of this work being (a) incorporating well-founded structural disjoining pressures into thin-film

---

<sup>1</sup>As mentioned in Chapter 1, we again note by ‘advective’ motion, we refer to classical hydrodynamic motion of the film—principally using the term to contrast with the diffusive dynamics added in Sec. 6.4



modelling, and (b) to propose and probe a model that switches between diffusion and hydrodynamics.

This chapter is structured as follows: The relevant physical concepts of interfacial science are introduced in Sec. 6.2. In Sec. 6.3 the mathematical description of steady and spreading drops is derived and the solution methodology that is used to solve the model are introduced. An extension to include diffusive effects into the dynamics is discussed in Sec. 6.4 and results are presented in Secs. 6.5-6.7. Finally, our concluding remarks for this chapter are made in Sec. 6.8.

## 6.2 The form of the binding potential

Note that one can also use a molecular dynamics computer simulation based method for calculating  $g(h)$  [101, 102, 78, 103, 104]. For simple Lennard-Jones like fluids it was shown [4, 5, 6] that the following form gives a good fit to the binding potential over the whole range:

$$g(h) = \frac{H(e^{-p(h)} - 1)}{12\pi h^2}, \quad (6.2.1)$$

where  $p(h) = h^2(a_0e^{-a_1h} + a_2 + a_3h + a_4h^2 + a_5h^5)$ . Eq. (6.2.1) gives the correct decay for  $h \rightarrow \infty$ , namely that in Eq. (1.3.5), but remains finite in the limit  $h \rightarrow 0$ . However, as also shown in Ref. [5], Eq. (6.2.1) is not appropriate for all liquids as it does not capture any layering effects. It is then shown that for a simple fluid with only short-range attractive interactions between the molecules (i.e., no van der Waals contribution,  $H = 0$ ), the following form gives a good fit to the binding potential data obtained using

DFT:

$$g_2(h) = e^{-\frac{h}{a_0}} [a_5 + a_4 \cos(a_1 h + a_2)] + a_6 e^{-2\frac{h}{a_0}} + a_7 e^{-3\frac{h}{a_0}} + a_8 e^{-4\frac{h}{a_0}} + a_9 e^{-5\frac{h}{a_0}} + a_{10} e^{-6\frac{h}{a_0}}. \quad (6.2.2)$$

$a_0$  is the bulk correlation length in the liquid phase at the interface, and the other  $a_i$ 's corresponds to further constants, determined via fits to the DFT data and for the particular treated case take the following values:  $a_0 = 0.907508$ ,  $a_1 = -7.35183$ ,  $a_2 = 5.90059$ ,  $a_3 = 0$ ,  $a_4 = -0.011038$ ,  $a_5 = -0.000147646$ ,  $a_6 = 0.0449827$ ,  $a_7 = 0.422683$ ,  $a_8 = -0.7673$ ,  $a_9 = -0.230683$  and  $a_{10} = 0.559131$  [5]. These are all in units where the particle diameter  $\sigma = 1$  and the thermal energy  $k_B T = 1$ , where  $k_B$  is the Boltzmann constant and  $T$  the temperature of the system. Henceforth, these are the units in which all lengths and energies are given.

Eq. (6.2.2) has a damped oscillatory decay as  $h \rightarrow \infty$ . The oscillations lead to the presence of multiple minima in  $g_2(h)$ , which result in the formation of ‘steps’ or ‘terraces’ in the vicinity of the contact line at the droplet edge – examples are displayed later in Sec. 6.5. Each subsequent minimum in  $g_2(h)$  corresponds to the addition of a further layer. In Fig. 6.2 we display a plot of  $g_2(h)$ , appropriately scaled with  $\sigma^2/(k_B T)$ . The global minimum is labelled ‘0’, where the film thickness (adsorption) is very small, and there are almost zero molecules on the substrate, so the system is partially-wetting, but with small contact angle  $\theta$ , since  $g(h_0)$  is only slightly negative. The boxed labels ‘1’, ‘2’, ‘3’, and ‘4’ indicate the local minima corresponding to the respective number of complete layers of molecules on the substrate. We can see from Fig. 6.2 that in this system, one layer of molecules is not as favourable as two or more complete layers of molecules. Note that the oscillatory behaviour in  $g_2(h)$  is also seen in the corresponding liquid density profiles in the full DFT calculations [5].

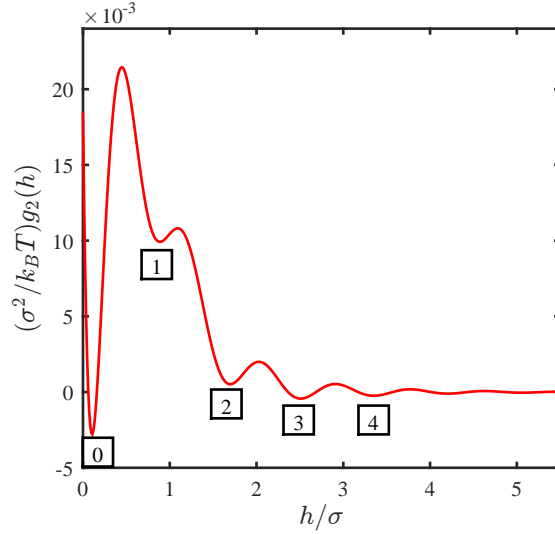


Figure 6.2: A plot of the binding potential in Eq. (6.2.2), calculated in [5] using DFT. The global minimum is labelled ‘0’, as this state corresponds to Area 1 in Fig. 6.1, where the film thickness is almost zero. The local minima at larger  $h$  are labelled ‘1, 2, 3, 4’ and represent one, two, three and four layers of molecules, respectively.

Eq. (6.2.2) contains many parameters and is the binding potential for a particular liquid on a particular substrate at a particular temperature [5]. Here we seek to understand the overall effects of oscillatory binding potentials on liquid drop shapes and the spreading behaviour. Therefore we truncate the expression in Eq. (6.2.2) to obtain the following simplified expressions,

$$g_3(h) = a \cos(hk + b)e^{-\frac{h}{c}} + de^{-\frac{h}{2c}}, \quad (6.2.3)$$

and

$$g_4(h) = a \cos(hk + b)e^{-\frac{h}{c}} + de^{-\frac{2h}{c}}, \quad (6.2.4)$$

where  $a$ ,  $b$ ,  $c$ ,  $d$ ,  $k$  are coefficients that we vary to determine the generic types of

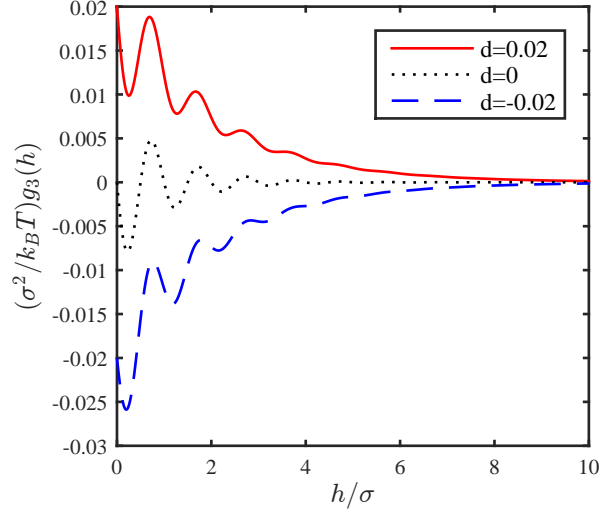


Figure 6.3: A plot of binding potential  $g_3(h)$  in Eq. (6.2.3) with  $a = 0.01$ ,  $b = \pi/2$ ,  $c = 1$ ,  $k = 2\pi$ ,  $d = 0.02$  (solid red line)  $d = 0$  (dotted black line) and  $d = -0.02$  (dashed blue line).

behaviours that one can observe. We introduce two oscillatory binding potentials where one has exponential decay ( $g_3(h)$ ) and the other one has oscillatory decay ( $g_4(h)$ ). These simpler expressions retain the overall character of the expression in Eq. (6.2.2), but contain fewer parameters. In Figs. 6.3 and 6.4 we display plots of the binding potentials (6.2.3) and (6.2.4), respectively, with the typical parameter values that we use in our study, namely  $a = 0.01$ ,  $b = \pi/2$ ,  $c = 1$ ,  $k = 2\pi$ , and varying the parameter  $d$ , such as  $d = 0.02$  (red) which represents a wetting situation,  $d = 0$  (black) refers to a partially-wetting case but close to the wetting transition, and  $d = -0.02$  (blue) partially-wetting.

These two binding potentials  $g_3(h)$  and  $g_4(h)$  are somewhat more generic than  $g_2(h)$ , but at the same time they retain the oscillatory behaviour of  $g_2(h)$ , which gives the layering. The lowest (positive) local minimum of  $g_3(h)$  for  $d = 0.02$  is at  $h = 0.2522$

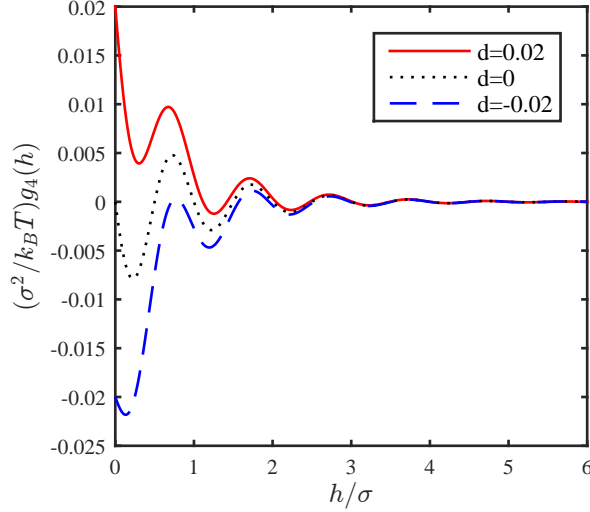


Figure 6.4: A plot of binding potential  $g_4(h)$  in Eq. (6.2.4) with  $a = 0.01$ ,  $b = \pi/2$ ,  $c = 1$ ,  $k = 2\pi$ ,  $d = 0.02$  (solid red line)  $d = 0$  (dotted black line) and  $d = -0.02$  (dashed blue line).

which is similar to the local minimum of the full expression  $g_2(h)$  with the parameter values obtained from the DFT results in Ref. [5], namely  $h = 0.1081$ . For relatively large  $h$ , both  $g_3(h)$  and  $g_4(h)$  tend to zero but with different limiting behaviours. For  $g_3(h)$ , the exponential decay dominates whereas for  $g_4(h)$ , the sinusoidal oscillations dominate. Note that the ultimate asymptotic decay is determined by the form of the decay into bulk of the liquid density profiles that are in contact with a substrate [105, 106, 5, 6]. Whether the decay is monotonic or damped oscillatory depends on the state point (i.e. temperature and density) and on which side of the Fisher-Widom (FW) line this state point is. The FW line is the locus in the phase diagram at which the asymptotic decay of the radial distribution function crosses over from monotonic to damped-oscillatory decay [105, 106, 107].

### 6.3 Thin film equation

The time evolution of a thin liquid film on a surface can be derived from energetic considerations. In the approximate systems of Fig. 1.3, the free energy of the system is

$$F_{\text{IH}}[h] = \iint \left[ g(h) + \frac{\gamma_{lv}}{2} (\nabla h)^2 \right] dx dy. \quad (6.3.1)$$

This contains two contributions: (i) the binding potential contribution from the molecular interactions with the substrate and (ii) the energy of the free surface (surface tension), where  $\nabla = (\frac{\partial}{\partial x}, \frac{\partial}{\partial y})$  is the 2D gradient operator. The latter is proportional to the fluid surface area and the approximation  $\sqrt{1 + (\nabla h)^2} \approx 1 + \frac{1}{2}(\nabla h)^2$ , appropriate when the gradients are small, has been made in Eq. (6.3.1). We have also neglected an irrelevant constant term.

The quantity

$$\frac{\delta F_{\text{IH}}}{\delta h} = -\Pi - \gamma_{lv} \nabla^2 h \quad (6.3.2)$$

is the negative of the local pressure in the film and so any gradients in this quantity give the thermodynamic force which drives the flow of liquid over the substrate. There is therefore a current  $\mathbf{j} = -Q(h) \nabla \frac{\delta F_{\text{IH}}}{\delta h}$ , where  $Q(h)$  is the mobility coefficient. Combining this with the continuity equation, we obtain [108, 16]

$$\frac{\partial h}{\partial t} = -\nabla \cdot \mathbf{j} = \nabla \cdot \left[ Q(h) \nabla \frac{\delta F_{\text{IH}}[h]}{\delta h} \right]. \quad (6.3.3)$$

The mobility coefficient  $Q(h)$  depends on the film thickness. Often the expression  $Q(h) = h^3/(3\eta)$  is assumed, where  $\eta$  is the fluid viscosity. This is what emerges from the long-wave approximation of the Navier-Stokes equations with no-slip boundary

conditions [63], giving

$$\frac{\partial h}{\partial t} = \nabla \cdot \left( \frac{h^3}{3\eta} \nabla (-\gamma_{lv} \nabla^2 h - \Pi(h)) \right). \quad (6.3.4)$$

Assuming some slip, then  $Q(h)$  can acquire additional terms, for example, Navier-slip [109] results in  $Q(h) = \beta h^2 + h^3/3\eta$  [63, 110]. In the next section we discuss further mobilities  $Q(h)$  which describe diffusion effects.

Equilibrium (steady state) drop profiles are those which minimise  $F_{\text{IH}}[h]$  subject to the constraint that the volume of the liquid  $V = \iint h dx dy$  is fixed, i.e. which minimise

$$\Omega[h] \equiv F_{\text{IH}}[h] + \lambda \iint h dx dy, \quad (6.3.5)$$

where  $\lambda$  is the Lagrange multiplier associated with the volume constraint. The minimising curve satisfies

$$\frac{\delta \Omega}{\delta h} = 0, \quad (6.3.6)$$

which is equivalent to

$$-\Pi - \gamma_{lv} \nabla^2 h = \lambda. \quad (6.3.7)$$

From this we can identify  $\lambda$  as the pressure difference across the interface due to the Laplace and disjoining pressures. If we consider a 1D droplet such that  $h = h(x)$  and let  $u = h, v = u'$ , we have

$$u' = h', \quad (6.3.8)$$

$$v' = \frac{1}{\gamma_{lv}} \left( \frac{dg}{dh} - \lambda \right), \quad (6.3.9)$$

which can be used to plot the phase plane diagram of equilibrium solutions, as shown

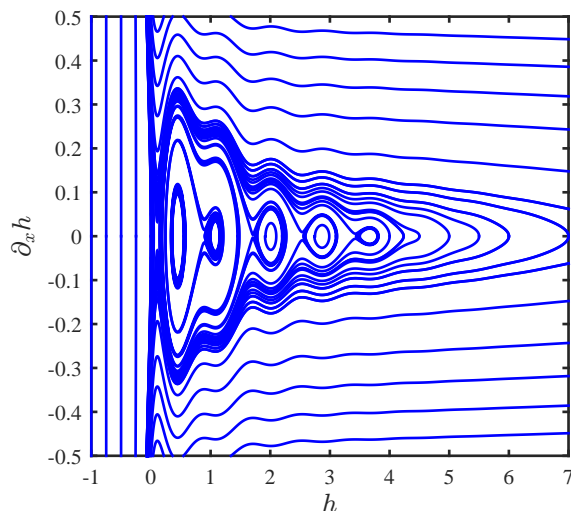


Figure 6.5: A phase plane diagram when the binding potential is  $g_2$  in Eq. (6.2.2) and  $\gamma_{lv} = 0.51$ , which shows all possible equilibrium solutions of our thin film equation as the maximal drop height is varied, with the Lagrange multiplier having the value  $\lambda = 9.8 \times 10^{-4}$ .

in Fig. 6.5 (for standard Derjaguin pressures such plots can be found in Refs. [108, 111] where also the influence of  $\lambda$  is discussed). In this figure closed loops correspond to periodic solutions – i.e. the solutions that one obtains on finite domains with periodic boundary conditions. This allows one to determine at a glance the range of equilibrium profiles that one may expect to obtain from the model. The oscillations in the ‘streamlines’ in Fig. 6.5 correspond to steps or terraces in the contact line region of the droplet solutions. Such droplet profiles are obtained below as stationary solutions of our PDE model.



## 6.4 Incorporating the effects of diffusion into the mobility

In droplet spreading simulations with the advective mobility, we see that on some occasions a very thin precursor film can extend ahead of the bulk of the main droplet. Physically, when this film is very thin, in particular when the film thickness is much less than the order of a particle diameter  $\sigma$ , such as illustrated in Area 1 in Fig. 6.1, we would expect the motion to be dominated by diffusion. Currently our model only describes the advective motion over the substrate – recall that Eq. (6.3.4) is obtained from a long-wave approximation to Navier-Stokes plus no-slip boundary conditions.

We now seek to modify the thin-film equation in a simple way such that both, diffusion and advection occur throughout the droplet, but for where the adsorbed film is very thin (i.e. less than roughly a monolayer or two), diffusion dominates, but for where the film thickness is larger, advection dominates. Thus, the two limiting cases we require are: (i) the diffusion equation

$$\frac{\partial h}{\partial t} = \nabla \cdot (D \nabla h), \quad \text{when } h \ll \sigma, \quad (6.4.1)$$

where  $D$  is the diffusion coefficient for particles moving over the surface, and (ii) the thin-film equation

$$\frac{\partial h}{\partial t} = \nabla \cdot \left[ \frac{h^3}{3\eta} \nabla \frac{\delta F_{\text{IH}}}{\delta h} \right], \quad \text{when } h \gg \sigma, \quad (6.4.2)$$

which is Eq. (6.3.4). Both Eqs. (6.4.1) and (6.4.2) can be obtained as appropriate limits of the more general Eq. (6.3.3), if the mobility  $Q(h)$  is suitably generalised, as we now show.

To see how a diffusion equation can be obtained, we consider the case when  $h$  is close

to 0. From the Maclaurin series expansion of  $g(h)$  we obtain  $-\Pi(h) = g'(0) + g''(0)h + \dots$ , which, together with Eq. (6.3.2), gives

$$\frac{\delta F_{\text{IH}}}{\delta h} = g'(0) + g''(0)h - \gamma_{lv} \nabla^2 h + \dots \quad (6.4.3)$$

If we assume

$$Q(h) = \alpha_0 + \alpha_1 h + \alpha_2 h^2 + h^3/(3\eta), \quad (6.4.4)$$

then in the  $h \rightarrow 0$  limit we have  $Q(h) \approx \alpha_0$  and so from Eqs. (6.3.3) and (6.4.3) we obtain

$$\frac{\partial h}{\partial t} \approx \alpha_0 \nabla^2 (g''(0)h - \gamma_{lv} \nabla^2 h), \quad (6.4.5)$$

which in the limit where the first term dominates (for example if scaling into regions near contact lines), yields Eq. (6.4.1), together with the result that  $\alpha_0 = D/g''(0)$ .

In the limit when  $h$  is large, Eq. (6.4.4) gives  $Q(h) \approx h^3/(3\eta)$ , and so the desired result, Eq. (6.4.2), is recovered. Thus, our final model is

$$\frac{\partial h}{\partial t} = \nabla \cdot \left[ \left( \frac{D}{g''(0)} + \frac{h^3}{3\eta} \right) \nabla (-\gamma_{lv} \nabla^2 h - \Pi(h)) \right], \quad (6.4.6)$$

where we have set the coefficients  $\alpha_1$  and  $\alpha_2$  to zero. If we kept the terms involving  $\alpha_1$  and  $\alpha_2$  we would effectively be also investigating the effect of slip at the substrate, which at these molecular scales is usually seen as a coarse grained method to account for any number of physical processes that allow for contact line motion [112]. In particular, as mentioned previously  $\alpha_2$  can be associated with the popular Navier-slip model, and  $\alpha_1$  with a nonlinear slip model [110]. Detailed comparisons between slip models in the thin-film setting can be found elsewhere [113, 114, 115].

We note that other authors have discussed the modelling of diffusion or diffusive

regimes in thin films [116, 117, 118]. Ref. [116] used a piece-wise mobility for diffusive and advective regimes in a mesoscopic hydrodynamic approach to droplet motion due to surface freezing/melting. The authors of Ref. [117] have a discussion on adiabatic and diffusive films, but they talk about them in a different context than the present work. In [117] the argument is that when the edge of the film is very thin it becomes approximately flat so that curvature effects are negligible. In this case the thin film equation can be written in the same form as the diffusion equation with an (approximately constant) height-dependent diffusion term being  $D(h) = -h^3/(3\eta)\partial_h\Pi$ . Clearly this is quite different to our proposed implementation where we wish to model a diffusive region of the droplets where height increases from zero or a negligible value  $h \ll \sigma$  to  $h \approx \sigma$  rapidly. Finally, Ref. [118] compares the time evolution of relaxing liquid ridges employing various different mobility functions, including a diffusive one.

Returning to our governing equation (6.4.6), we now nondimensionalise, by scaling

$$\begin{aligned} \nabla &= \frac{1}{\sigma} \nabla^*, \quad h = \sigma h^*, \quad t = \tau t^*, \quad \Pi = \frac{k_B T}{\sigma^3} \Pi^*, \\ \gamma_{lv} &= \frac{k_B T}{\sigma^2} \gamma_{lv}^*, \quad F_{IH} = k_B T F_{IH}^*, \end{aligned} \quad (6.4.7)$$

where we recall that  $\sigma$  is the diameter of particles on the substrate, and  $\nabla^*$ ,  $h^*$ ,  $t^*$ ,  $\Pi^*$  and  $\gamma_{lv}^*$  are the dimensionless quantities, and we have also given a scaling for the total free energy as its dynamic evolution is investigated in our numerical results presented below. By taking

$$\tau = \frac{3\eta\sigma^3}{k_B T}, \quad \bar{\alpha}_0 = \frac{3\alpha_0\eta}{\sigma^3} = \frac{3D\eta}{g''(0)\sigma^3}, \quad (6.4.8)$$

we obtain

$$\frac{\partial h^*}{\partial t^*} = \nabla^* \cdot [(\bar{\alpha}_0 + h^{*3}) \nabla^* (-\gamma_{lv}^* \nabla^{*2} h^* - \Pi^*)]. \quad (6.4.9)$$

Subsequently, we drop the ‘\*’ for simplicity. This is our new equation which describes the evolution of the liquid film, incorporating both advection and diffusion.

## 6.5 Spreading on a non-zero background adsorption

The results presented in this section are obtained for the four binding potentials introduced in section 6.2. The time simulations are initiated at the instant when the droplet is released onto the substrate and are carried out until the droplet comes to rest, at the equilibrium steady state (where we monitor the free energy and see it reaches a constant). The initial condition is assumed to be a drop shape which is modelled with a Gaussian function of the form

$$h(x, t = 0) = Ce^{-\left[\frac{(x-x_f/2)}{E}\right]^2} + h_b, \quad (6.5.1)$$

where the parameter  $h_b$  is the background value of  $h$ , i.e. the imposed layer height far away from the droplet, which can be set to a value  $\neq h_0$  if desired. Recall that the height  $h_0$  is the height of the ‘precursor’ film/foot that extends away from the droplet during its approach to equilibrium. It is the height at which the lowest (positive) minimum of the binding potential occurs. In particular,  $h_0$  corresponds to the global minimum of  $g_1$  (the commonly investigated spreading situation) and  $g_2$  (the terraced spreading situation), but not necessarily the global minimum of  $g_3$  or  $g_4$  (the generalised versions of  $g_2$ ), depending on their parameter values.

In Eq. (6.5.1), the parameter  $C$  is the amplitude of the initial droplet, i.e. it is the height of the droplet above the background film at time  $t = 0$ .  $E$  controls the width of the initial droplet, and  $x_f$  is the length of the domain.

This initial condition specifies the height  $h(x, t = 0)$  in the  $z$ -axis, and it is assumed

uniform in the  $y$ -direction to create a 2D droplet. The spreading of 2D droplets has been investigated extensively [63, 115] as they give qualitatively the same behaviour as for 3D axisymmetric droplets, particularly in the important region near the contact line. Periodic boundary conditions are applied, so that  $h(x = 0, t) = h(x = x_f, t)$ , and the symmetry of the droplet is preserved in the dynamics due to the symmetric initial condition of Eq. (6.5.1).

All computations are performed using a method of lines technique, using finite difference approximations for the spatial derivatives, trapezoidal numerical integration for computing integrals (for the free energy and for confirming mass conservation), and the *ode15s* Matlab variable-step, variable-order (VSVO) solver [90]. A convergence test was applied, with the conclusion that a small enough grid size should be applied—typically here  $dx = 0.2$ , details are given in the Appendix A.

To be able to compare the spreading dynamics of droplets with the two binding potentials  $g_1$  and  $g_2$ , given by Eqs. (1.3.7) and (6.2.2) respectively, we first must find the values of parameters  $a$  and  $b$  in  $g_1$  which make the contact angle and  $h_0$  for both binding potentials the same. Combining Eq. (1.3.3) and Young's equation (1.2.1), gives the following relationship between the minimum of the binding potential and the equilibrium contact angle [3, 58, 119]

$$\theta = \cos^{-1} \left( 1 + \frac{g(h_0)}{\gamma_{lv}} \right). \quad (6.5.2)$$

For  $g_2$  in Eq. (6.2.2), with the coefficients given by DFT calculation [5], the minimum of  $g_2$  is  $-0.0028$  at  $h_0 = 0.1081$ , and the corresponding surface tension (also from the DFT [5]) is  $\gamma_{lv} = 0.5101$ . This value of  $\gamma_{lv}$  is kept fixed throughout this section to enable a fair comparison between other effects such as the form of binding potential. The effect of surface tension is to smooth out gradients in the liquid-vapour film height

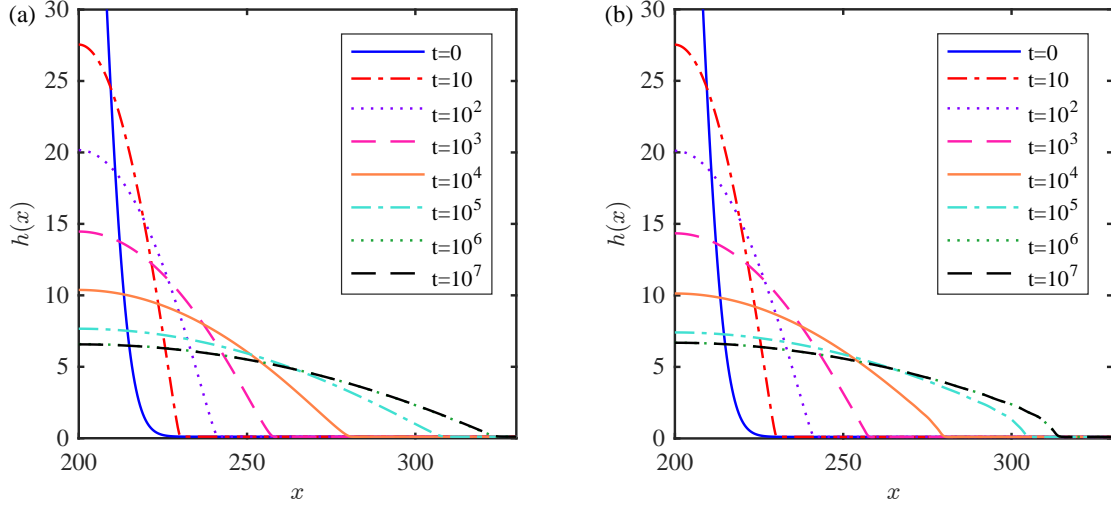


Figure 6.6: The time sequence of drop profiles for a liquid drop spreading on a substrate, with: (a) the binding potential  $g_1$  given by Eq. (1.3.7) with  $a = 2.756 \times 10^{-8}$  and  $b = 5.453 \times 10^{-5}$ , and (b) the binding potential  $g_2$  given by Eq. (6.2.2). The parameters in the initial condition are chosen as  $h_b = 0.1081$ ,  $C = 60$  and  $E = 10$  in both cases. The diffusive mobility coefficient  $\bar{\alpha}_0 = 0$ . The  $t = 0$  profile is centred at  $x = 200$  and then spreads until reaches equilibrium.

$h$ , thus a smaller surface tension would enhance the influence of the oscillatory binding potentials and give sharper terraces at equilibrium. Substituting these values back to Eq. (6.5.2) gives the equilibrium contact angle  $\theta = 6.006^\circ$ . By equating the value and location of the minimum of  $g_1$  in terms of the parameters  $a$  and  $b$ , with the respective numeric values for  $g_2$ , we find  $a = 2.756 \times 10^{-8}$  and  $b = 5.453 \times 10^{-5}$ , which allow a direct comparison between binding potentials  $g_1$  and  $g_2$ , and the investigation of the effect of oscillatory binding potentials.

Fig. 6.6(a) shows the time sequence of drop profiles for a liquid drop spreading on a substrate already covered by an equilibrium background film, with binding potential  $g_1$

given by Eq. (1.3.7), with  $a = 2.756 \times 10^{-8}$  and  $b = 5.453 \times 10^{-5}$ . The diffusive mobility coefficient  $\bar{\alpha}_0 = 0$ . The parameters in the initial condition are chosen as  $h_b = 0.1081$ ,  $C = 60$  and  $E = 10$ . The  $t = 0$  profile is centred at  $x = 200$  and then spreads. The liquid spreads rapidly from rest until  $t \approx 10^4$  under the effect of surface tension due to the significant difference between effective imposed initial contact angle and the equilibrium contact angle. The spreading then slows as the droplet equilibrates, as expected. The curves for times  $t = 10^6$  and  $t = 10^7$  are overlapped and virtually indistinguishable, indicating that equilibrium has been reached.

The results in Fig. 6.6(a) are for the single-well binding potential of  $g_1$ . Fig. 6.6(b) shows the equivalent time sequence of drop profiles for the oscillatory binding potential  $g_2$  in Eq. (6.2.2). The spreading dynamics initially follows a very similar trajectory until approximately  $t \approx 10^5$ . The height at the centre of the droplet continues to equilibrate at a similar rate to the case in Fig. 6.6(a) (with  $g_1$ ) but for  $t \gtrsim 10^4$  we notice the emergence of a foot, or terrace, in the droplet near the contact line at a value  $h \approx 2$  corresponding to the third minimum in the oscillatory binding potential  $g_2$  (with label ‘2’ in Fig. 6.2), corresponding to a thickness of two particle layers.

From these comparisons we see that the dynamics is predominately driven by the relaxation of the contact angle to its equilibrium, and finer details of the binding potential do not dramatically change the timescales of spreading—especially when monitoring the equilibration of the maximal droplet height. However, significant differences near the contact line can occur where oscillations lead to terracing of the droplet. We see a reduction in wetting length for equilibrium droplets: the right contact line location at approximately  $x = 325$  and  $x = 315$  in Figs. 6.6(a) and 6.6(b), respectively. A more detailed comparison of the two equilibrium droplet profiles is given in Fig. 6.7. We see a marginal difference in maximal height, with more pronounced differences in the contact line region, with the final drop shape with binding potential  $g_2$  having obvious ‘steps’,

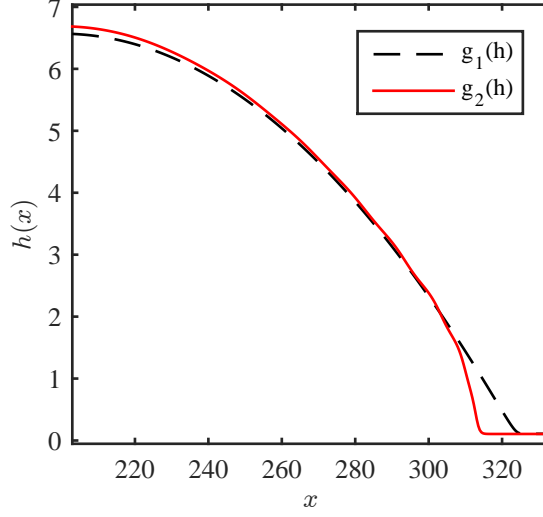


Figure 6.7: A comparison of the final equilibrium droplets with binding potentials  $g_1$  and  $g_2$ , corresponding to Figs. 6.6(a) and 6.6(b). The equilibrium contact angle  $\theta$ , the surface tension  $\gamma_{lv}$  and the initial condition are the same for both cases.

or terraces (for example, at  $x \approx 306$  and  $x \approx 298$ ). This is caused by the oscillations in the binding potential  $g_2$ , with each ‘step’ corresponding to one layer of fluid particles (recall that whilst one layer is a local minimum in  $g_2$ , it is far less preferable than for  $h = h_0$  or for two or more complete layers of particles).

Fig. 6.8 shows the time evolution of the total free energies given by Eq. (6.3.1), appropriately nondimensionalised as in Eq. (6.4.7), corresponding to the two spreading situations in Figs. 6.6- 6.6(b). This shows that the timescales of spreading are unaffected by the choice of  $g_1$  or  $g_2$  in the case where coefficients were chosen to fix identical  $h_0$  values and equilibrium contact angles. In this particular example then, it appears as though the formation of the terraces seen in Fig. 6.7 (with  $g_2$ ) does not change the speed of approach to equilibrium. However, further investigation with a variety of initial conditions has shown that other events unique to oscillatory binding potentials



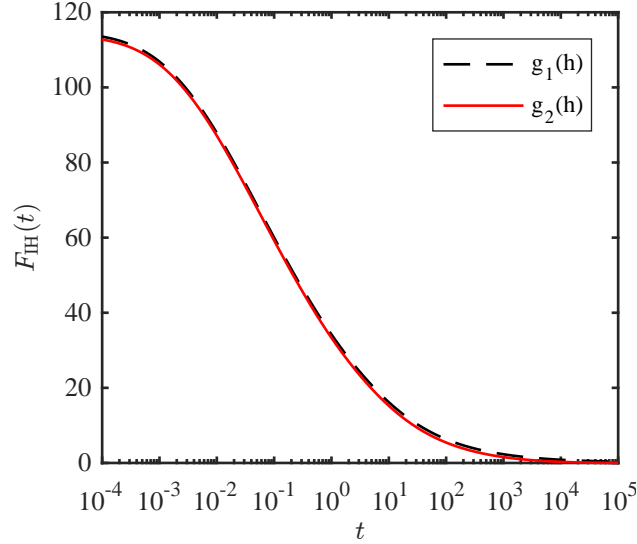


Figure 6.8: The time evolution of the free energy (6.3.1) as a droplet spreads to equilibrium with binding potentials  $g_1$  and  $g_2$ , corresponding to Figs. 6.6(a) and 6.6(b). The equilibrium contact angle  $\theta$ , the surface tension  $\gamma_{lv}$  and the initial condition are the same for both cases.

can have significant effects, which we detail later.

Having demonstrated that oscillatory binding potentials are worthy of greater scrutiny through visualising the difference between the commonly used  $g_1$  form to the specific  $g_2$  one taken from a particular DFT calculation, we now analyse the more generic behaviour of binding potentials with oscillations, as given by the simplified forms  $g_3$  and  $g_4$ .

In Fig. 6.9 we display equilibrium drop profiles when the binding potential is  $g_3$  in Eq. (6.2.3), for various values of the parameter  $d$ , namely  $d = \{0.02, 0, -0.02\}$  (c.f. Fig. 6.3). The other parameters take the values  $a = 0.01$ ,  $b = \frac{\pi}{2}$ ,  $c = 1$  and  $k = 2\pi$ . The parameters in the initial condition are chosen as  $C = 6$ ,  $E = 10$ ,  $x_f = 200$ , and

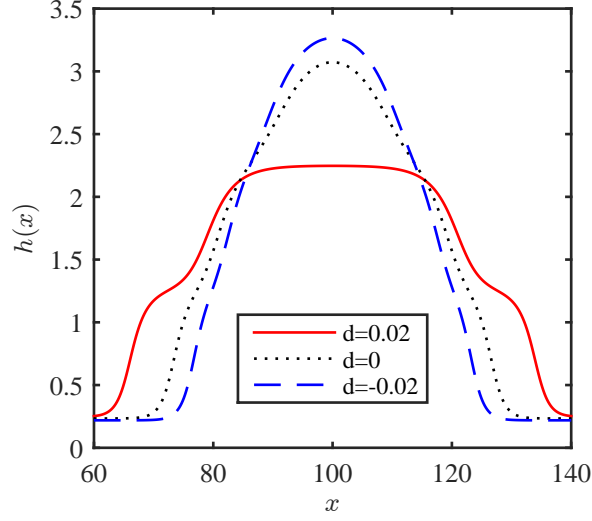


Figure 6.9: Equilibrium drop profiles with binding potential  $g_3$  in Eq. (6.2.3) as the parameter  $d$  is varied and with  $a = 0.01$ ,  $b = \frac{\pi}{2}$ ,  $c = 1$ ,  $k = 2\pi$ .

$h_b = \{0.2522, 0.2282, 0.1921\}$  for  $d = \{0.02, 0, -0.02\}$ , respectively. These give the lowest (positive) local minimum at a similar value to that of  $g_2$ , to allow for direct comparison. As discussed in Sec. 6.2,  $d = 0.02$  is wetting whereas the other two are partially-wetting (although  $d = 0$  is close to the wetting transition). From Fig. 6.9 we see the influence of this, as the drops for higher  $d$  spread out further, and thus have lower maximal height. The height spacing of the steps seen in these equilibrium drop profiles also corresponds to the spacing of the minima in  $g_3$ .

To explore the dynamics of spreading using  $g_3$ , in Fig. 6.10 we plot the time evolution of the normalised free energy difference

$$\Delta(t) = \frac{F_{\text{IH}}(t) - F_{\text{IH}}(t = \infty)}{F_{\text{IH}}(t = 0) - F_{\text{IH}}(t = \infty)}, \quad (6.5.3)$$

where the free energy  $F_{\text{IH}}$  is given by Eq. (6.3.1). One might expect a smooth approach

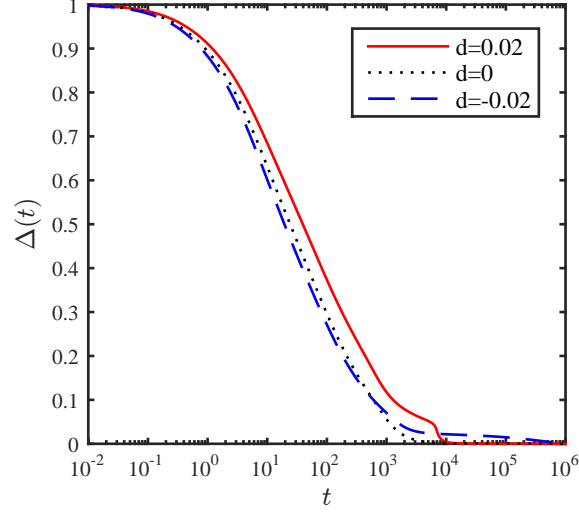


Figure 6.10: The normalised free energy difference for droplet spreading under the influence of binding potential  $g_3$ , for various values of the parameter  $d$ . The expression of  $g_3$  is given by Eq. (6.2.3), with  $a = 0.01$ ,  $b = \frac{\pi}{2}$ ,  $c = 1$ , and  $k = 2\pi$ .

to equilibrium, as observed in Fig. 6.8. Instead, we see a number of stages to the dynamics, including the usual initial spreading/relaxation from the initial condition; the formation of terraces; a ‘popping’ event where a rapid reduction of the free energy results from a sudden jump of the droplet free surface from one minimum of the binding potential to another; and then finally the usual long-time approach to equilibrium. The small jump for  $d = 0.02$  happens at  $t \approx 10^4$  and there are not any obvious jumps for  $d = 0$  and  $d = -0.02$ .

To understand the dynamics more clearly, in Fig. 6.11 we plot the time sequence of drop profiles for binding potential  $g_3$  with  $d = 0.02$ . The time is chosen from where the ‘popping’ event is about to happen till it finishes. The drop starts to form two ‘terraces’ from  $t = 10^3$ , in the corresponding normalised free energy difference curve displayed in Fig. 6.10 this behaviour is shown as the first inflection point where the normalised free

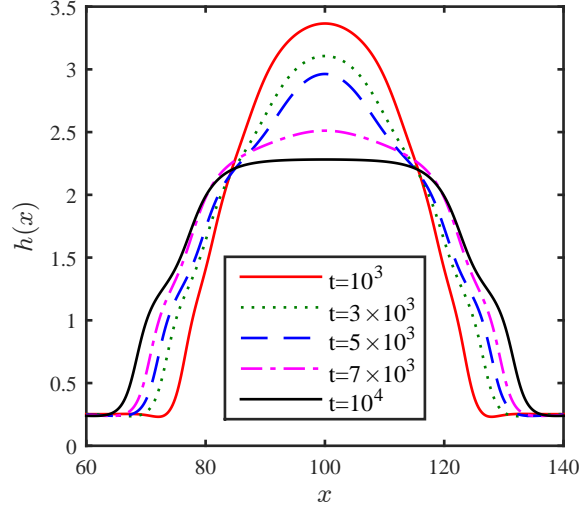


Figure 6.11: A time sequence of drop profiles for a liquid drop spreading on a substrate, with binding potential  $g_3$  given by Eq. (6.2.3), with  $a = 0.01$ ,  $b = \frac{\pi}{2}$ ,  $c = 1$ ,  $k = 2\pi$ ,  $d = 0.02$ . The initial condition is chosen as  $h_b = 0.2522$ ,  $C = 6$ ,  $E = 10$  and  $x_f = 200$ . The corresponding free energy time evolution is displayed as the solid (red) line in Fig. 6.10.

energy difference  $\approx 0.1$ . As the drop spreads from  $t = 3 \times 10^3$  to  $t = 5 \times 10^3$ , the top part of the drop becomes ‘sharper’ and then it suddenly jumps down to form a flat top to minimise the free energy. This is an example of a ‘popping’ events that leads to the sudden decreases observed in Fig. 6.10. After  $t = 10^4$  the drop keeps spreading and reaches equilibrium.

Fig. 6.12(a) shows a sequence of equilibrium droplet profiles using binding potential  $g_3$  with fixed  $d = 0.02$  and various values of  $a$ . The time evolution of the normalised free energy differences leading to the formation of these drops is displayed in Fig. 6.12(b) and the corresponding binding potentials are displayed in Fig. 6.12(c). All of these drops have the same values of  $C = 6$ ,  $E = 10$  and  $x_f = 200$ . Smaller values of  $a$  lead to

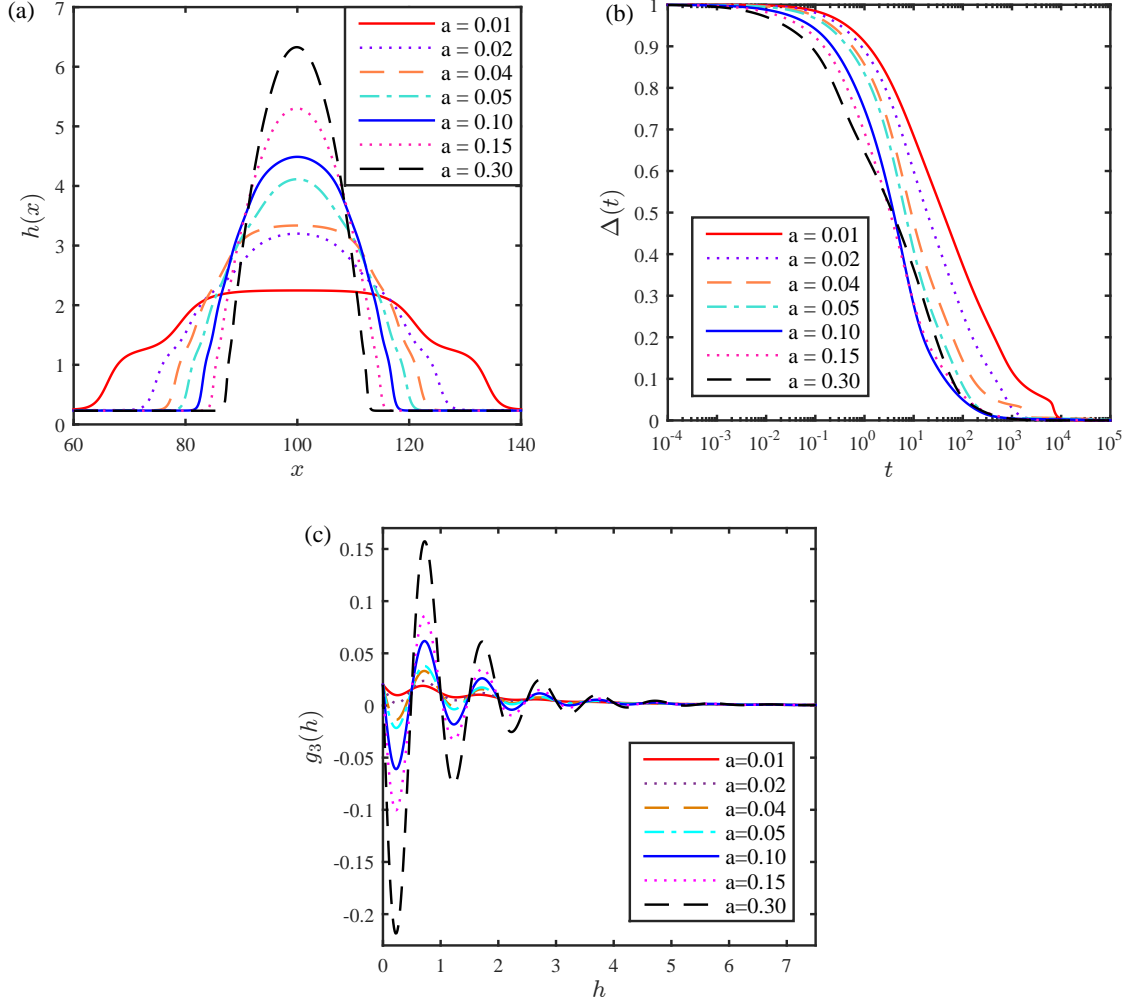


Figure 6.12: (a) A sequence of equilibrium droplet profiles with binding potential  $g_3$  and varying  $a$ , as given in the legend. We also have  $d = 0.02$ , and  $h_b$  is set as the lowest positive minimum of the binding potential (for  $a = 0.01$ ,  $h_b = 0.3$ , for  $a = 0.02$ ,  $h_b = 0.2282$ , for  $a \geq 0.04$ ,  $h_b = 0.1322$ ). (b) A plot of the time evolution of the normalised free energy differences of the dynamics leading to the formation of the drops in (a). (c) Shows the corresponding binding potentials.

broader droplets with flatter tops and fewer steps. This is due to the amplitude of the oscillations in the binding potential being smaller and the correspondingly higher value of the lowest positive local minima. As  $a$  increases, the system undergoes a wetting transition, so the most obvious effect on the droplets is the extent of spreading, which is controlled by the equilibrium contact angle which in turn is determined by the height of the lowest positive minimum in the binding potential.

Fig. 6.12(b) shows the corresponding normalised free energy differences for spreading on these binding potentials. As before, steps in this quantity correspond to popping events or the emergence of terraces. There are overall trends as  $a$  is varied, such as secondary (and higher) terracing events are harder to see in curves for large  $a$ . Also, in general, the spreading to equilibrium occurs more quickly for greater  $a$ , as would be expected from the binding potentials and equilibrium droplet profiles, given that the distance the droplet has to spread is less. However, there are exceptions to this trend such as the case with  $a = 0.04$ , where the ‘popping’ event takes an unusually long time to occur. Thus, it is possible for the crossing of the normalised free energy difference curves for different values of  $a$ , where at a particular stage of the dynamics certain evolutions are slowed by the formation of terraces (e.g. by being ‘pinned’ to particular heights), whereas at the same time such an event does not occur in an otherwise slower (larger difference between initial and equilibrium contact angles) spreading situation. We believe the occurrence of slow dynamics in the system corresponds to parts of the profile having to pass over saddles in the free energy.

Comparing the normalised free energy difference curves for  $a = 0.1$  and  $a = 0.3$  in Fig. 6.12(b), we see the curves cross and are rather different in shape, indicating that the different stages of the dynamics occur on different timescales. Interestingly, however, both take the same overall time to finally equilibrate. The  $a = 0.3$  case initially decreases much more rapidly, due to the high barrier in the binding potential

between the minimum at  $h_0$  and the next minimum at  $h_1$ , corresponding to 1 layer of particles [see Fig. 6.12(c)]. The free energy cost of having  $h \approx \frac{1}{2}(h_0 + h_1)$  is high, so the system chooses  $h = h_0$  or  $h = h_1$  as quickly as it can. Following this, there is a slower relaxation over a longer timescale. In contrast, for  $a = 0.1$  the energy difference between the first positive local maximum and the neighbouring minimum is much less, so there is only one timescale visible in the relaxation to equilibrium.

Having investigated the dynamics of spreading for  $g_3$ , a binding potential with oscillations but also having monotonic exponential decay at larger  $h$ , we now focus on  $g_4$ , which has oscillatory decay for  $h \rightarrow \infty$ .

Final equilibrium drop profiles with the binding potential  $g_4$  for various values of the parameter  $d$  are shown in Fig. 6.13(a). The initial drop profile (6.5.1) has  $C = 6$ ,  $E = 10$ ,  $x_f = 200$ , and  $h_b = \{0.3, 0.2282, 0.1322\}$  which are the corresponding minima ( $h_0$ ) for  $d = \{0.02, 0, -0.02\}$ . Similar to the drop profiles with binding potential  $g_3$ , higher values of  $d$  lead to broader droplets and flatter tops, as the system passes through the wetting transition. However, instead of having two complete layers of particles for  $d = 0.02$  as shown in Fig. 6.9 for  $g_3$ , the final equilibrium shape with binding potential  $g_4$  has only one particle layer. This is in agreement with intuitive analysis of the plot of  $g_4$  against  $h$  in Fig. 6.4, since the global minimum of  $g_4$  with  $d = 0.02$  is at  $h \approx 1$  and thus one layer of particles is preferred.

To investigate the dynamics of spreading with binding potential  $g_4$ , in Fig. 6.13(b) we plot the corresponding normalised free energy difference over time for the same three values of  $d$ . In the two  $d \neq 0$  cases the drop takes a much longer time to reach equilibrium than the cases in Fig. 6.12 (with  $g_3$ ). Also, there are two obvious ‘popping’ events on the  $d = 0.02$  curve. At the first inflection point (at  $t \approx 10^3$ ), the drop starts to form terraces and the centre of the drop ‘pins’ to a particular height until the first jump (‘popping event’) occurs between  $t = 10^3$  and  $t = 10^4$ , where the normalised

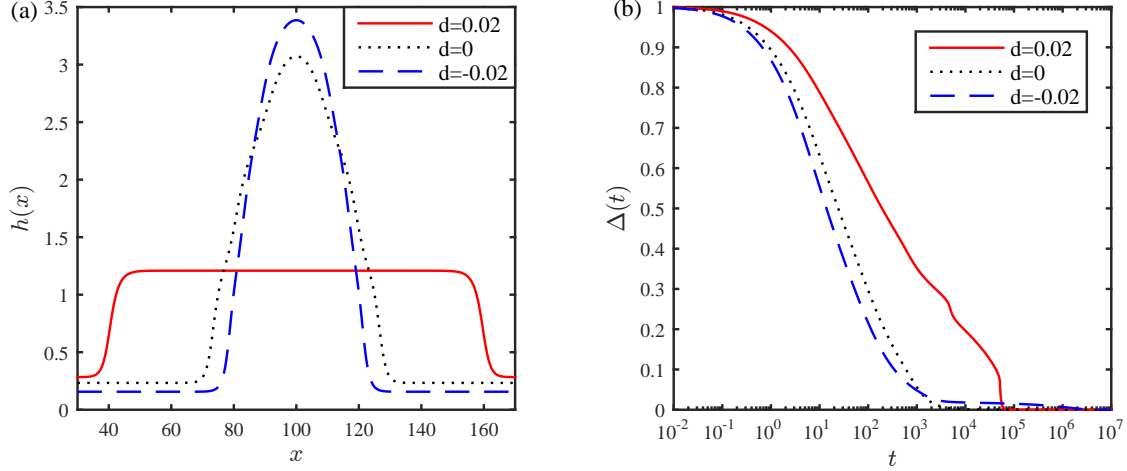


Figure 6.13: (a) Equilibrium drop profiles with the binding potential  $g_4$  in Eq. (6.2.4), as the parameter  $d$  is varied. We take  $a = 0.01$ ,  $b = \frac{\pi}{2}$ ,  $c = 1$ ,  $k = 2\pi$  and  $d = \{0.02, 0, -0.02\}$ . (b) The corresponding normalised free energy difference for the spreading of the droplets.

energy difference drops down from  $\approx 0.26$  to  $\approx 0.22$ , during which the top part of the droplet flattens. A similar process occurs again at  $t \approx 7 \times 10^4$  because one layer of particles is slightly more favourable than two or more layers of particles (see Fig. 6.4). We believe that in this case the dynamics is particularly slow because the difference in the free energy of the different minima of  $g_4$  for  $d = 0.02$  are rather small.

The slow dynamics for the case  $d = -0.02$  in Fig. 6.13(b) is for a different reason. Looking at the time evolution of the drop profile, the drop initially seems to reach equilibrium with a background film height equal to  $h_0$ . However, this leaves the top of the droplet on a maximum in the binding potential, and so the background film height raises up slightly to allow the top of the drop to move off the maximum. In the final equilibrium neither the background film nor the top of droplet are in any binding potential minima, but nonetheless the state is the best overall equilibrium for the entire



droplet.

In Fig. 6.14(a) we display a sequence of equilibrium droplet profiles for binding potential  $g_4$  and various values of  $a$ . As  $a$  is increased the amplitude of the oscillations in  $g_4$  increases and also the system is further from the wetting transition with a larger contact angle, since the primary minimum in  $g_4$  at  $h = h_0$  becomes lower as  $a$  is increased. In Fig. 6.14(b) we display the corresponding time evolution of the normalised free energy difference and in (c) the binding potential. The overall behaviour is somewhat similar to that displayed in Fig. 6.12 for binding potential  $g_3$ . However, the overall time it takes to equilibrate varies even more in this case, being anywhere in the range  $10^3 - 10^6$ . As before, this is due to the slow dynamics that occurs due to popping, pinning and other such events as the droplet evolves in a complex free energy landscape having many long ‘valleys’ and saddle points.

## 6.6 Spreading versus dewetting towards equilibrium

In view of the apparent complexity in the underlying free energy landscape in which the spreading droplet evolves, a natural question to arise is: does that landscape exhibit multiple minima? All the results presented so far correspond to spreading droplets, so to address this question, we also consider cases where the initial condition consists of a pancake-like drop that is spread out more than the expected final equilibrium state, so that the evolution towards equilibrium consists of a dewetting dynamics, with the contact line of the droplet receding.

In some cases, identical equilibrium profiles are found from both spreading and dewetting simulations. However, it is also not uncommon for different equilibria to be realised. In Fig. 6.15 we highlight a case of this latter situation, where the initial

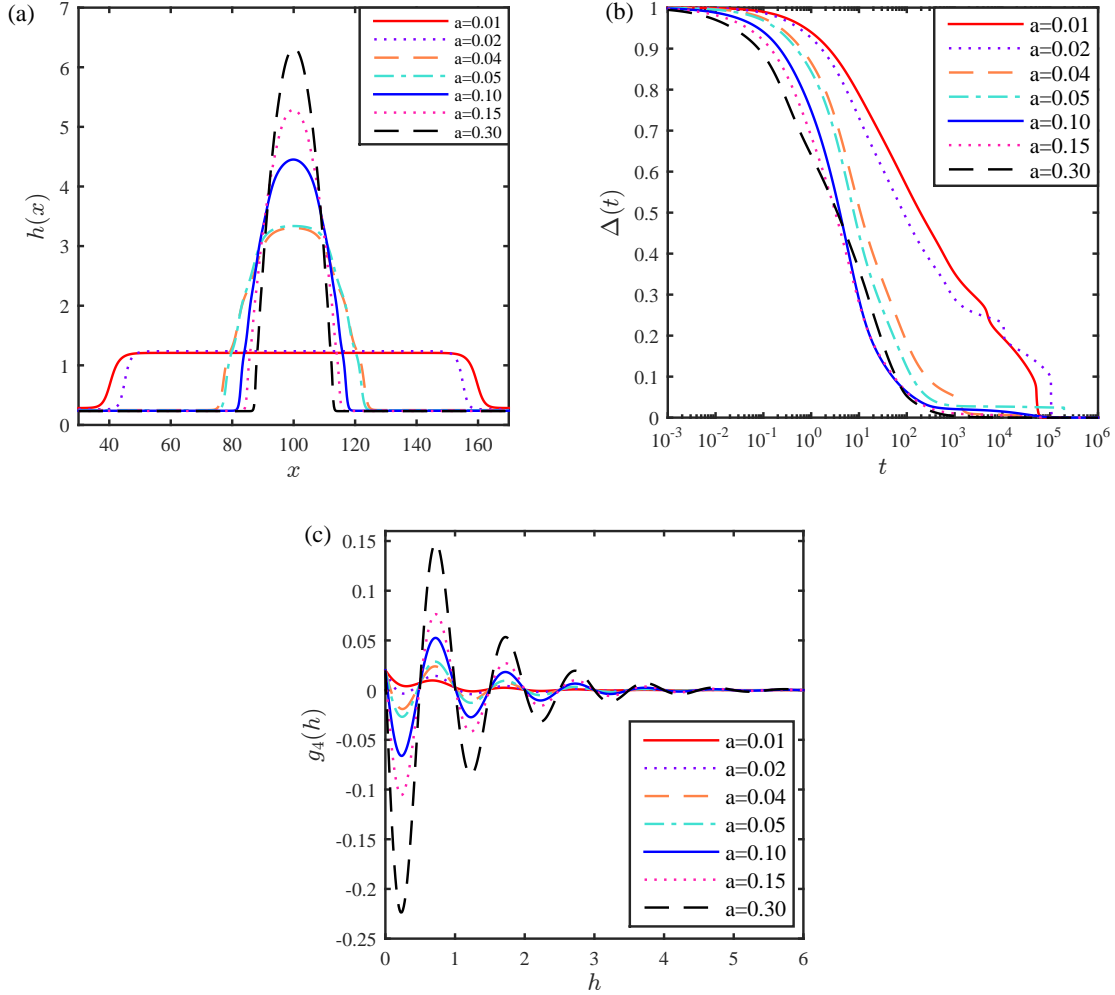


Figure 6.14: (a) A sequence of equilibrium droplet profiles with binding potential  $g_4$  and varying  $a$ , as given in the legend. We also have  $d = 0.02$ , and  $h_b$  is set as the lowest positive minimum of the binding potential (for  $a = 0.01$ ,  $h_b = 0.300$ , for  $a = 0.02$ ,  $h_b = 0.2642$ , for  $a = \{0.04, 0.05\}$ ,  $h_b = 0.2402$ , and for the remaining values of  $a$ ,  $h_b = 0.2282$ ). (b) A plot of the time evolution of the normalised free energy differences of the dynamics leading to the formation of the drops in (a). (c) Shows the corresponding binding potentials.

profiles for spreading and dewetting were given as

$$h(x, t = 0) = 18.00 e^{-\left[\frac{(x-x_f/2)}{6}\right]^2} + h_b, \quad (6.6.1)$$

and

$$h(x, t = 0) = 1.694 e^{-\left[\frac{(x-x_f/2)}{60}\right]^8} + h_b, \quad (6.6.2)$$

respectively, and where  $x_f = 400$ ,  $h_b = h_0 = 0.1081$ , and the binding potential  $g_2$  is used (we can also obtain the latter case with a larger domain i.e.  $x_f = 600$ ). Specifically, in Fig. 6.15(a) we present the final equilibrium states of two droplets with the same volume that have evolved to attain different equilibrium profiles—although as expected given both simulations are for identical substrates with the same binding potentials, the effective contact angle made with the background film is seen to be in agreement in both equilibria. We further note that the drops have dynamically evolved to find the locally lowest energy configuration for their height profile across the entire domain. As the effective domain is finite (due to the periodic boundary conditions), this means that the background height at equilibrium is not exactly  $h_0$ , the lowest (positive) minimum value for the imposed binding potential (in this case  $g_2(h)$ ). Indeed, the two cases in Fig. 6.15(a) have slightly different values for the background film height, corresponding to different values of  $\lambda$  [defined in Eq. (6.3.7)]. In Fig. 6.15(b) the corresponding evolutions of the normalised free energy differences are depicted to highlight the very different approaches to equilibrium for these two situations. We further note that they have not approached the same free energy equilibrium. In particular the spreading case has been able to find a lower minimum in the energy landscape, since it has reached  $F_{\text{IH}}(\infty) = 0.046$ , compared to  $F_{\text{IH}}(\infty) = 0.15$  for dewetting.

In our simulations, it is noticed that dewetting usually proceeds less rapidly than

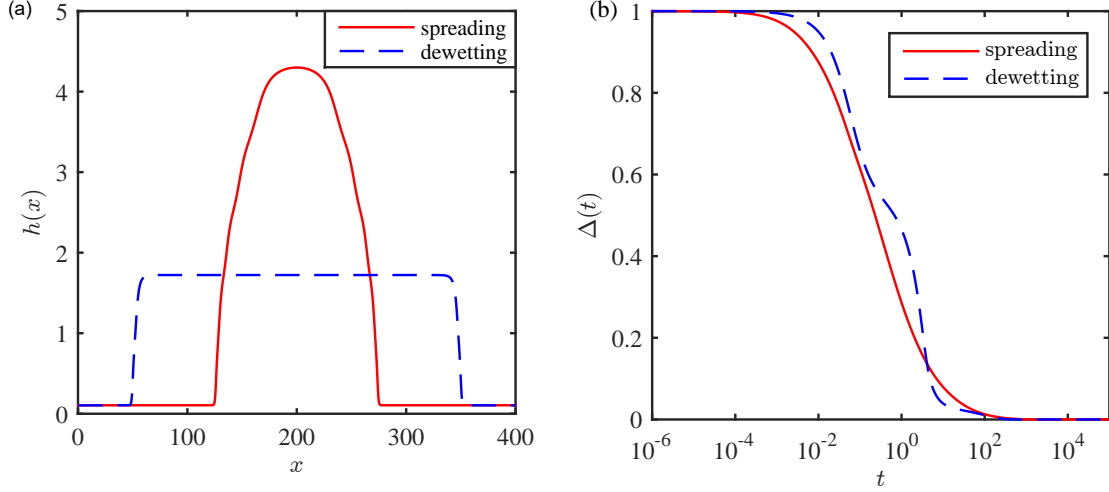


Figure 6.15: (a) The final equilibrium state obtained for the same volume of liquid on the surface undergoing both spreading and dewetting on a background film  $h = h_0$ . The binding potential used is  $g_2$ , with initial conditions that were evolved to reach these final equilibria given in (6.6.1) for the spreading situation, and (6.6.2) for dewetting. (b) shows the corresponding evolutions of the normalised free energy differences, noting that for spreading  $F_{\text{IH}}(0) = 16.89$  and  $F_{\text{IH}}(\infty) = 0.046$ , whereas for dewetting  $F_{\text{IH}}(0) = 0.44$  and  $F_{\text{IH}}(\infty) = 0.15$ .

spreading, as has been reported previously for droplet motion simulations [120]. Alongside the fact that the relative depth of the minima in the binding potentials are mostly greater for smaller values of film height, we see that popping events are much less common in dewetting than in spreading and the terraces are formed in a more gradual evolution.

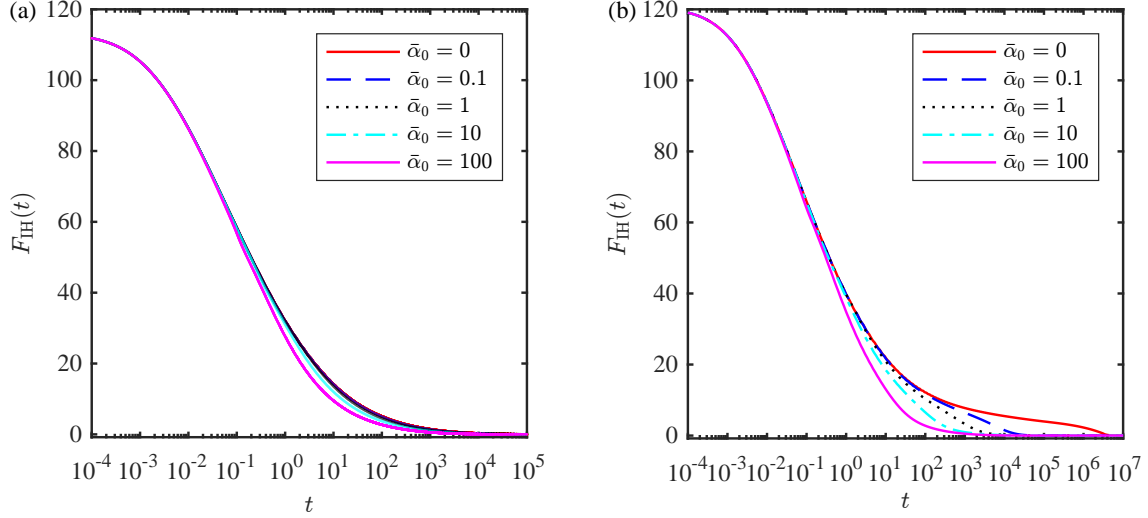


Figure 6.16: The free energy over time during droplet spreading with binding potential  $g_2$  for various values of the diffusion coefficient  $\bar{\alpha}_0$  on: (a) a substrate covered by a film of thickness  $h_b = h_0 = 0.1081$  and (b) a totally dry substrate, i.e.  $h_b = 0$ . The initial condition in both cases has  $C = 60$ ,  $E = 10$  and  $x_f = 400$ .

## 6.7 Including diffusion

All results presented thus far are for spreading onto a substrate already covered with a film of thickness  $h_0$ , essentially like conducting a spreading experiment on an ostensibly dry substrate but that already has a few particles adsorbed on it. We have modelled this situation assuming that the droplet evolution proceeds with advection only – i.e. the case where  $\bar{\alpha}_0 = 0$  in our governing equation (6.4.9). However, as discussed in Sec. 6.4, when the amount adsorbed on the substrate is a single monolayer or less, we expect the dynamics to be diffusive. This is even more true when thin films advance onto a substrate that is completely dry, with no particles at all present on the substrate before the droplet is introduced. Therefore, we now consider the case  $\bar{\alpha}_0 > 0$ .

We first consider the case where the binding potential is  $g_2$ . In Figs. 6.16(a) and

6.16(b) we show cases where the droplet is initiated on a background film of thickness  $h_b = h_0$  (as previously) and  $h_b = 0$  (a totally dry initial substrate), respectively. We see two main effects: (i) increasing diffusion (larger  $\bar{\alpha}_0$ ) speeds up the evolution in all cases; (ii) diffusion has a far greater impact when the droplet is spreading on a totally dry substrate, as in Fig. 6.16(b), compared to when spreading on an already present ‘precursor’. In these plots, a relatively large initial droplet is chosen (with  $C = 60$ ), hence most of the droplet has  $h \gg \sigma$  throughout the evolution. Thus, as anticipated in the model development discussion in Sec. 6.4, diffusion does not have a dramatic effect for large drops initially and  $O(1)$  times. However, for drops of any size, the latter stages of the approach to equilibrium ultimately requires a reshaping of the height profile along terraces (at small multiples of  $\sigma$ ) caused by the oscillatory binding potential. In these latter stages, diffusion then speeds up this reshaping process, and even for large droplets can decrease the time to reach equilibrium by orders of magnitude (e.g. see the behaviour of the free energy in Fig. 6.16(b) for  $F_{\text{IH}}(t) \lesssim 5$ ).

For much smaller droplets, however, where the average height of the drop is small, the diffusion is much more influential across the entire evolution, speeding up the equilibration. In Figs. 6.17(a) and 6.17(b) we plot the evolution of the free energy for a particular set of parameters in  $g_3$  and  $g_4$  for a small initial droplet on a totally dry substrate ( $C = 6, h_b = 0$ ). In these cases the spreading happens more rapidly when  $\bar{\alpha}_0 > 0$ . It can be many orders of magnitude faster than the case  $\bar{\alpha}_0 = 0$ . This shows that (i) including diffusion is essential in situations where the physics dictates that it has an effect, and that (ii) the order in which parts of the droplets evolve can be reversed. For example, consider the extreme cases of  $\bar{\alpha}_0 = 0$  and  $\bar{\alpha}_0 = 100$  in Fig. 6.17(b). For high diffusion the early time dynamics consists of the precursor foot spreading out rapidly, before a final popping event to reach equilibrium for the larger part of the droplet centre. In contrast, when there is no diffusion  $\bar{\alpha}_0 = 0$ , the spreading occurs

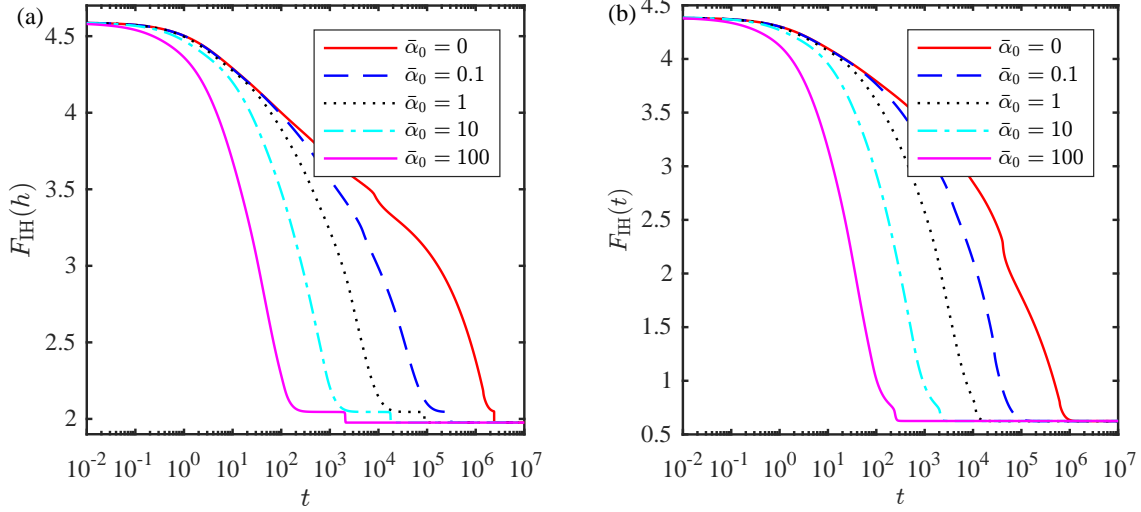


Figure 6.17: The free energy over time during droplet spreading on a totally dry substrate for various values of the diffusion coefficient  $\bar{\alpha}_0$  with: (a) binding potential  $g_3(h)$  and (b) binding potential  $g_4(h)$ . The initial condition in both cases is  $h_b = 0$ ,  $C = 6$ ,  $E = 10$  and  $x_f = 200$ .

as usual with the main part of the droplet evolving to very close to the final shape before the precursor foot eventually is formed in the final approach to equilibrium. In Fig. 6.18 we plot the time sequence of drop profiles for binding potential  $g_3(h)$  with diffusion coefficient  $\bar{\alpha}_0 = 1$ . The corresponding free energy time evolution is displayed as the dot (black) line in Fig. 6.17(a).

## 6.8 Concluding remarks

In this chapter we have investigated thin liquid films spreading on a flat solid substrate, including effects such as surface tension, oscillatory binding potentials, advective flow dynamics and surface diffusion. Lubrication theory and dimensional analysis have been

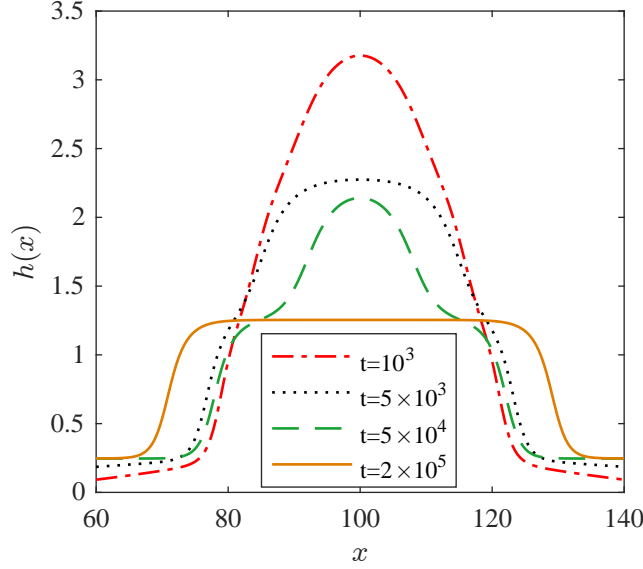


Figure 6.18: A time sequence of drop profiles for a liquid drop spreading on a substrate, with binding potential  $g_3$  given by Eq. (6.2.3), and diffusion coefficient  $\bar{\alpha}_0 = 1$ . The initial condition is chosen as  $h_b = 0$ ,  $C = 6$ ,  $E = 10$  and  $x_f = 200$ . The corresponding free energy time evolution is displayed as the dot (black) line in Fig. 6.17(a).

used to derive a model governing equation (6.4.6) for the drop height profile. From this one can also obtain the pressure and velocity profile. Solving numerically using the Finite Difference Method has allowed us to simulate the thin film droplet spreading.

The oscillatory binding potentials that we have used model the molecular packing that can occur in certain liquids at interfaces [1, 96, 97, 98, 5, 6, 59, 99]. These occur in systems that exhibit layering transitions near to the wetting transition. Note that spreading nanoparticle-laden drops [121] have previously been modelled with thin-film models incorporating oscillatory disjoining pressures [122, 123, 124]. These dynamical models describe the time evolution of two coupled fields: the height of the liquid film and the local concentration of nanoparticles. In Ref. [123] it is shown that the presence of



nanoparticles can also lead to terraced droplets and steps emerging from the contact line. In the context of the gradient dynamics form presented here in (6.3.3) it should be noted that such a form also exists for nanoparticle-laden or surfactant-laden films [125, 126, 127]. Such a model shows that an oscillatory nanoparticle-dependent wetting potential does not only result in an oscillatory disjoining pressure but also in a correspondingly amended chemical potential for the particles.

We have shown that having an oscillatory binding potential leads to a rich and varied droplet spreading dynamics. The time evolution towards equilibrium can often exhibit several stages. There is the usual spreading and relaxation from the initial condition, but there is also the formation of terraces and ‘popping’ events where there is a rapid drop in the free energy due to a jump of the droplet free surface from one minimum of the binding potential to another. There is also the usual final long-time approach to equilibrium. We believe this rich behaviour is due to the complexity of the underlying free energy landscape that exhibits multiple minima, long valleys along which the dynamics is slow and saddle points. To better understand the underlying free energy landscape, we expect a systematic phase plane analysis is required – i.e. a systematic examination how diagrams like that in Fig. 6.5 vary as the parameters in the system are changed.

Our extended thin-film hydrodynamic model (6.4.6) is also capable of describing the crossover from advective to diffusive dynamics that must occur when the film thickness is of order one particle thick or less. Such a crossover must occur [23]. We have shown that when diffusion is included, the droplet spreading is faster, particularly for very small droplets and for all droplets in the latter stages of their approach to equilibrium. Incorporating diffusion can also change the dynamic pathway taken – c.f. the discussion above around Fig. 6.17(b) and Ref. [118] where the nonlinear dynamics of

the Plateau-Rayleigh instability<sup>2</sup> of a liquid ridge is investigated comparing pathways occurring for different mobility functions. Note however that incorporating a small amount of diffusion does not change Tanner’s law [128]. Recall that Tanner’s law states that over a significant portion of the spreading time of a radially symmetric liquid drop (puddle), the radius  $R$  grows in time as  $R \sim t^n$ , with exponent  $n = 1/10$ . For 2D spreading drops like those studied here, the law still applies, but with exponent  $n = 1/7$  [128]. Tanner’s law was derived in situations with relatively small contact angle and slow spreading, i.e. small capillary number. We have checked that including moderate diffusion does not change Tanner’s law, however it does change the pre-factor, so that the overall time for the drop to equilibrate is less with diffusion incorporated. The extent of the time period that Tanner’s law holds (usually after initial transient relaxations to a quasistatic shape up until a change to exponential behaviour during the latter stages of approach to equilibrium) can also be significantly reduced in our oscillatory binding potential simulations. This happens, as would be expected, when the majority of the droplet profile lies in the region where terraces form and the greater range of dynamical features occur, creating the rich evolutions we have explored. A final note on the relevance of Tanner’s law, however, is that if a very large diffusion coefficient is imposed then the overriding asymptotic structure of the bulk of the droplet moving with a  $h^3$  mobility would break down, and in this situation we could expect an entirely different evolution. We leave this diffusion dominated regime for possible future work.

The work presented here has largely focused on the simplified oscillatory binding potentials  $g_3(h)$  and  $g_4(h)$ . Recall that the more complex  $g_2(h)$  in Eq. (6.2.2) is the one that was obtained as a fit to the DFT data [5]. Additionally, all of these have the

---

<sup>2</sup>The Plateau-Rayleigh instability occurs when a falling stream of liquid breaks up into droplets. As our work is 2D and this instability occurs in 3D, it is something we might consider in future work.

Hamaker constant  $H = 0$ . There is therefore clearly much more work to do understanding the spreading behaviour when realistic binding potentials are used that are valid for all values of film thickness. Comparison of different binding potentials could also be performed for a wider range of fluids, e.g. colloidal fluids, oils, polymeric solutions etc.

Other extensions to the present work that would be fruitful include solving for the droplet spreading dynamics in 3D, including gravity, e.g. to also consider sliding droplets, which exhibit extremely rich behaviour [129]. Preliminary results indicate that it would also be interesting to study what happens when the initial condition is not symmetric, and also the droplet dynamics in the presence of other droplets.

# Chapter 7

## Final Remarks

In this thesis we have modelled both nanoscale droplets and nanobubbles on surfaces. Using classical density functional theory, we have calculated the density profiles for varying amounts of fluid adsorbed at the wall and also the resulting effective interfacial free energy, which gives the binding potential, as a function of the film thickness  $h$ . This is an important quantity and gives the contribution to the excess free energy due to a film on a surface. The global minimum of the binding potential determines the wetting behaviour of the fluid on the substrate – i.e. quantities like the contact angle  $\theta$ . The commonly used forms of the binding potential, such as that in Eq. (1.3.7) are really only applicable for large film thickness. However, our method, based on DFT, which is a statistical mechanical theory, is able to capture information valid over the whole range of values of  $h$ .

The DFT that we used is fairly accurate, because it is based on FMT for Rosenfeld's theory for the reference hard-sphere fluid free energy. For the inter-particle attraction at long ranges, we model it using a Yukawa tail pair potential and treat its contribution to the free energy via a simple mean field approximation. This model is a generic model

for simple liquids [38] and so our results are relevant to a wide number of real-world pure fluid systems.

Significant new results in this thesis were presented in Chapters 5 and 6. The results in Chapter 5 are for the binding potentials calculated using DFT for a vapour nanobubble on a variety of different forms of external potentials. We demonstrated that having an accurately calculated binding potential does affect the wetting behaviour. We have also computed nanobubble profiles on a patterned heterogeneous surface and calculated the free energy on each surface, which allowed us to find the relative probability of having nanobubbles on such surfaces. Then in Chapter 6 we investigated the dynamics of terraced droplets which were caused by having an oscillatory binding potential with multiple minima. We have also extended our model such that it can describe both advective flow and surface diffusion.

These results constitute a multi-scale modelling method that can be applied to any system involving fluids at interfaces. The method takes as input the molecular interactions of the fluid particles and bridges the scales upwards to generate an approach that can be used to describe dynamic complex interfacial flows with moderate computational resources. Although here the approach was used for fairly simple systems consisting of bubbles and droplets on planar surfaces, it can straightforwardly be generalised to much more complex situations of industrial relevance.

Thus, in this thesis we have explained, extended and further developed the necessary tools to include nanoscopic physical information into macroscopic fluid models to understand equilibrium and dynamic wetting behaviours. Obvious interest remains in the full calculation of these processes in molecular and dynamical density functional theory (DDFT) simulations for validation and further development, but computations would require larger resources than with the methods used here. Other interesting areas of future research include incorporating phase change dynamics (evaporation or

condensation) and chemical reactions into this modelling approach. It could also be possible to investigate deformable substrates such as found in living systems or active fluids. Finally fundamental development of the underlying theory in situations far from equilibrium will also be needed.

# Appendix A

## Convergence Test

As a prerequisite to generating the results presented in Chapter 6, we conducted convergence tests in order to be certain of the accuracy of the solutions of our numerical analysis. There are some interesting results from this analysis relating to the choice of spatial grid spacing in the discretisation that readers should be aware of if trying to reproduce our results.

To test accuracy, we calculate droplet evolutions for a series of different mesh discretisations, going to increasingly finer meshes (i.e. an increase of the number of points within the interval) and compare the results with the previous one. If the results are equal within a small percentage error, the first mesh is good enough. On the other hand, if the results differ by a large amount, the same process must be repeated for a finer mesh. A finer mesh generally results in a more accurate solution and lowers the convergence error, indeed once the grid is sufficiently fine, convergence does occur. However this requires progressively larger memory and takes more time to compute – particularly for the time evolution given the effective number of ODEs to be solved increases with the number of grid points. Thus a desirable mesh would combine acceptable accuracy

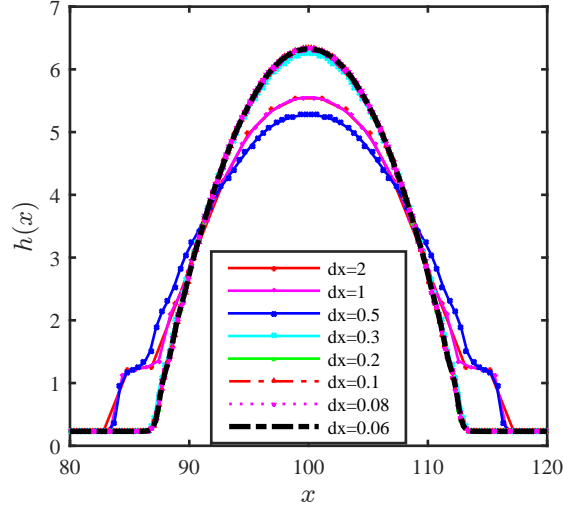


Figure A.1: Equilibrium droplet profile with  $g_3$  and with  $x_f = 200$ ,  $d = 0.02$ ,  $a = 0.3$ ,  $h_b = 0.2282$ , discretising with various grid spacings  $dx$  to obtain the numerical solution, where  $dx = \frac{x_f}{N}$  and where  $N$  is the total number of grid points. The values used are  $N = 100$ ,  $N = 200$ ,  $N = 400$ ,  $N = 667$ ,  $N = 1000$ ,  $N = 2000$ ,  $N = 2500$ , and  $N = 3333$ . The last four of these are virtually indistinguishable.

with economical cost.

Fig. A.1 shows the sequence of the droplet profiles for  $g_3$  with  $d = 0.02$ ,  $a = 0.3$ ,  $C = 6$  and  $E = 10$ , with different  $dx$ , where  $dx$  is the grid spacing  $dx = \frac{x_f}{N}$ , where  $N$  is the number of grid points and is chosen as  $N = 100$ ,  $N = 200$ ,  $N = 400$ ,  $N = 667$ ,  $N = 1000$ ,  $N = 2000$ ,  $N = 2500$ , and  $N = 3333$ . There is a greatly elongated terrace of height  $h(x) \approx 1$  for the curves with the coarsest three discretisations, which disappears as  $dx$  decreases. Also, the terraces in these curves are more pronounced compared to the others. Thus in this case, a poor mesh grid results in a very different final equilibrium droplet shape. There is also sometimes a loss of volume during the time evolution when the grid spacing is too large, i.e. the algorithm does not accurately capture the



conservation of mass, which must be satisfied in our non-volatile system.

# Appendix B

## Parameter Values for the Binding Potential Fit Functions

In Table B.1 we give values of the coefficients in the binding potential  $g(\Gamma)$  in Eq. (5.5.3), obtained by fitting to the results from DFT for a range of different values of the parameters in the wall potential, for the fluid with  $\lambda = \sigma$  and  $\beta\epsilon = 0.5$ .

## APPENDIX B. PARAMETER VALUES FOR THE BINDING POTENTIAL FIT FUNCTIONS

Table B.1: The parameter values  $a_1, a_2, \dots, a_8$  and  $l_0$  in the binding potential  $g(\Gamma)$  in Eq. (5.5.3), obtained from fitting to the data calculated using the DFT, for the various different wall potentials given in Eqs. (5.4.1)–(5.4.4). The attraction and range parameters  $\epsilon_w^{(i)}$  and  $\lambda_w^{(i)}$  in these potentials are also given below. The first column refers to the number of the figure above in which the binding potentials are displayed.

Figure	wall type	$\beta\epsilon_w^{(i)}$	$\lambda_w^{(i)}/\sigma$	$a_1$	$a_2$	$a_3$	$a_4$	$a_5$	$a_6$	$a_7$	$a_8$	$l_0$
3	Y	1.817	1	-0.102902	-1.52976	-7.19867	45.6063	-82.5011	64.6922	-18.9215	0	1.13494
5.2	Y	0	1	0.436017	1.56668	-5.80142	10.5037	-10.2276	5.2632	-1.12803	0	0.764648
5.2	Y	0.3	1	0.188742	1.01604	-1.10085	-1.90374	6.14653	-5.55662	1.72492	0	0.834599
5.2	Y	0.6	1	0.0636616	-0.0223561	3.88825	-12.2983	17.6613	-12.1129	3.23861	0	0.898494
5.2	Y	0.9	1	-0.00913047	-1.07813	8.16947	-20.2538	25.6447	-16.2729	4.12271	0	0.914339
5.2	Y	1.2	1	-0.103283	-2.23702	13.5188	-31.1874	37.6513	-23.154	5.74073	0	0.894094
5.2	Y	1.5	1	-0.316933	-3.50244	22.3324	-53.6347	66.6376	-42.0627	10.6847	0	0.832845
5.2	Y	1.8	1	-0.0998242	-1.4847	-6.998	44.2127	-79.8251	62.5049	-18.2605	0	1.13798
5.2	Y	2.1	1	-0.187165	-0.875099	-20.9172	99.1027	-170.089	130.938	-38.0072	0	1.13219
5.3(a)	LJ	0	1	0.412147	1.61894	-5.73846	10.0637	-9.48287	4.71324	-0.974014	0	0.775053
5.3(a)	LJ	0.1	1	0.374952	0.774098	-3.02401	5.77044	-5.69195	2.90088	-0.607194	0	0.695483
5.3(a)	LJ	0.2	1	-0.0259831	0.448125	-2.49345	8.72886	-13.2268	9.67743	-2.72339	0	1.32478
5.3(a)	LJ	0.3	1	-0.110418	0.500301	-8.71096	38.0178	-72.4731	72.5622	-37.2913	7.78349	1.08473
5.3(a)	LJ	0.4	1	-0.426825	0.267704	-21.7157	122.223	-279.301	326.179	-193.284	46.2408	0.917036
5.4(a)	Y	1.82	1	-0.10833	-1.40042	-7.99612	47.6637	-85.1519	66.386	-19.3495	0	1.13885
5.4(a))	LJ	0.4	1	-0.426825	0.267704	-21.7157	122.223	-279.301	326.179	-193.284	46.2408	0.917036
5.4(a)	G	2.5	1	-0.202165	-1.65283	-17.9331	135.977	-352.077	448.15	-283.891	71.6529	0.983802
5.4(a)	E	1.813	1	-1.09031	-2.16095	30.576	-99.8449	165.53	-151.694	73.1886	-14.5204	0.823677
5.6	E	1	0.1	0.422319	1.45854	-4.35437	3.93238	5.11002	-14.2398	11.6767	-3.39351	0.77295
5.6	E	1	0.3	0.411692	1.11381	-2.86337	0.299185	10.7624	-19.7299	14.683	-4.09718	0.765508
5.6	E	1	0.5	0.274977	0.375024	2.8439	-17.8841	43.0349	-52.6678	32.7557	-8.2269	0.788426
5.6	E	1	0.7	0.0666694	-0.635408	10.4577	-39.9909	78.0552	-84.3057	48.0902	-11.3238	0.855997
5.6	E	1	0.9	-0.0977131	-1.83569	16.2998	-50.1598	83.5545	-79.3539	40.6478	-8.74109	0.943813
5.6	E	1	1.1	-0.683713	0.654502	11.6287	-50.4985	99.458	-105.867	59.1351	-13.6179	0.836162
5.6	E	1	1.3	-0.868291	-0.0780018	10.9717	-29.3915	32.1351	-11.0863	-4.90455	3.32424	0.932054
5.6	E	1	1.5	-1.0713	0.527968	-0.0153676	26.0912	-95.6713	142.44	-98.7294	26.4225	1.01572
5.6	E	1	1.8	-1.43689	3.52772	-29.5133	143.46	-330.821	397.535	-242.33	59.4076	1.12934
5.6	E	1	2.1	-1.86145	8.06742	-64.7503	260.356	-529.595	580.619	-329.22	76.0464	1.23315

# Bibliography

- [1] P.-G. De Gennes, F. Brochard-Wyart, and D. Quéré, *Capillarity and wetting phenomena: Drops, bubbles, pearls, waves*. Springer, 2013.
- [2] T. Young, “An essay on the cohesion of fluids,” *Philos. Trans. Roy. Soc. London*, vol. 95, pp. 65–87, 1805.
- [3] P.-G. De Gennes, “Wetting: statics and dynamics,” *Rev. Mod. Phys.*, vol. 57, no. 3, p. 827, 1985.
- [4] A. P. Hughes, U. Thiele, and A. J. Archer, “Liquid drops on a surface: Using density functional theory to calculate the binding potential and drop profiles and comparing with results from mesoscopic modelling,” *J. Chem. Phys.*, vol. 142, no. 7, p. 074702, 2015.
- [5] A. P. Hughes, *Determining the shape of a liquid droplet: from microscopic theory to coarse grained models*. PhD thesis, Loughborough University, 2015.
- [6] A. P. Hughes, U. Thiele, and A. J. Archer, “Influence of the fluid structure on the binding potential: Comparing liquid drop profiles from density functional theory with results from mesoscopic theory,” *J. Chem. Phys.*, vol. 146, no. 6, p. 064705, 2017.

- [7] B. V. Derjaguin and N. V. Churaev, “On the question of determining the concept of disjoining pressure and its role in the equilibrium and flow of thin films,” *J. Colloid Interface Sci.*, vol. 66, no. 3, pp. 389–398, 1978.
- [8] B. V. Derjaguin and E. V. Obukov, “Anomalien dünner Flüssigkeitsschichten III,” *Acta Physicochim. URSS*, vol. 5, no. 1, pp. 1–22, 1936.
- [9] J.-D. Chen, “Effects of London–van der Waals and electric double layer forces on the thinning of a dimpled film between a small drop or bubble and a horizontal solid plane,” *J. Colloid Interface Sci.*, vol. 98, p. 329, 1984.
- [10] J. N. Israelachvili and H. Wennerström, “Entropic forces between amphiphilic surfaces in liquids,” *J. Phys. Chem.*, vol. 96, no. 2, pp. 520–531, 1992.
- [11] H. T. Davis, *Statistical mechanics of phases, interfaces, and thin films*. Wiley-VCH, 1996.
- [12] J. N. Israelachvili, *Intermolecular and Surface Forces*. London: Academic Press, 3rd ed., 2011.
- [13] M. C. Stewart and R. Evans, “Critical drying at a spherical substrate,” *J. Phys.: Condens. Matter*, vol. 17, no. 45, p. S3499, 2005.
- [14] L. W. Schwartz and R. R. Eley, “Simulation of droplet motion on low-energy and heterogeneous surfaces,” *J. Colloid Interface Sci.*, vol. 202, no. 1, pp. 173–188, 1998.
- [15] L. Pismen, “Mesoscopic hydrodynamics of contact line motion,” *Colloid. Surf. A*, vol. 206, no. 1–3, pp. 11–30, 2002.

- [16] U. Thiele, “Thin film evolution equations from (evaporating) dewetting liquid layers to epitaxial growth,” *J. Phys.: Condens. Matter*, vol. 22, no. 8, p. 084019, 2010.
- [17] S. Dietrich, “Wetting phenomena,” in *Phase Transitions and Critical Phenomena* (C. Domb and J. Lebowitz, eds.), vol. 12, Academic Press, London, 1988.
- [18] M. Schick, “An introduction to wetting phenomena,” in *Liquids at Interfaces, Proceedings of the Les Houches 1988 Session XLVIII*, Elsevier, 1988.
- [19] M. Schick, “Liquids at interfaces, Proceedings of the Les Houches summer school in theoretical physics, session XLVIII,” 1990.
- [20] R. Evans, M. C. Stewart, and N. B. Wilding, “Drying and wetting transitions of a Lennard-Jones fluid: Simulations and density functional theory,” *J. Chem. Phys.*, vol. 147, no. 4, p. 044701, 2017.
- [21] D. Bonn, J. Eggers, J. Indekeu, J. Meunier, and E. Rolley, “Wetting and spreading,” *Rev. Mod. Phys.*, vol. 81, no. 2, p. 739, 2009.
- [22] A. Münch, B. Wagner, and T. P. Witelski, “Lubrication models with small to large slip lengths,” *J. Eng. Math.*, vol. 53, pp. 359–383, 2005.
- [23] T. Ala-Nissila, R. Ferrando, and S. C. Ying, “Collective and single particle diffusion on surfaces,” *Adv. Phys.*, vol. 51, no. 3, pp. 949–1078, 2002.
- [24] S. F. Burlatsky, G. Oshanin, A. M. Cazabat, M. Moreau, and W. P. Reinhardt, “Spreading of a thin wetting film: Microscopic approach,” *Phys. Rev. E*, vol. 54, pp. 3832–3845, 1996.

- [25] J. W. Gibbs, *Elementary principles in statistical mechanics*. Edward Arnold, London, 1902.
- [26] R. Evans, “The nature of the liquid-vapour interface and other topics in the statistical mechanics of non-uniform, classical fluids,” *Adv. Phys.*, vol. 28, no. 2, pp. 143–200, 1979.
- [27] T. F. Meister and D. M. Kroll, “Density-functional theory for inhomogeneous fluids: application to wetting,” *Phys. Rev. A*, vol. 31, no. 6, p. 4055, 1985.
- [28] P. Tarazona, U. M. B. Marconi, and R. Evans, “Phase equilibria of fluid interfaces and confined fluids: non-local versus local density functionals,” *Mol. Phys.*, vol. 60, no. 3, pp. 573–595, 1987.
- [29] F. van Swol and J. R. Henderson, “Wetting and drying transitions at a fluid-wall interface. Density-functional theory versus computer simulation. II,” *Phys. Rev. A*, vol. 43, no. 6, p. 2932, 1991.
- [30] J. R. Henderson, P. Tarazona, F. van Swol, and E. Velasco, “Weighted density functional theories of drying at solid–fluid interfaces: Clarification of recent controversies,” *J. Chem. Phys.*, vol. 96, no. 6, p. 4633, 1992.
- [31] R. Evans, “Density functionals in the theory of nonuniform fluids,” in *Fundamentals of Inhomogeneous Fluids* (D. Henderson, ed.), ch. 3, pp. 85–175, Taylor & Francis, 1992.
- [32] J. Wu, “Density functional theory for chemical engineering: From capillarity to soft materials,” *AIChE Journal*, vol. 52, no. 3, pp. 1169–1193, 2006.

- [33] A. P. Hughes, U. Thiele, and A. J. Archer, “An introduction to inhomogeneous liquids, density functional theory, and the wetting transition,” *Am. J. Phys.*, vol. 82, no. 12, pp. 1119–1129, 2014.
- [34] A. Nold, B. D. Goddard, P. Yatsyshin, N. Savva, and S. Kalliadasis, “Pseudospectral methods for density functional theory in bounded and unbounded domains,” *J. Comp. Phys.*, vol. 334, pp. 639–664, 2017.
- [35] A. Nold, D. N. Sibley, B. D. Goddard, and S. Kalliadasis, “Fluid structure in the immediate vicinity of an equilibrium three-phase contact line and assessment of disjoining pressure models using density functional theory,” *Phys. Fluids*, vol. 26, no. 7, p. 072001, 2014.
- [36] A. Nold, L. G. MacDowell, D. N. Sibley, B. D. Goddard, and S. Kalliadasis, “The vicinity of an equilibrium three-phase contact line using density-functional theory: density profiles normal to the fluid interface,” *Mol. Phys.*, vol. 116, no. 17, pp. 2239–2243, 2018.
- [37] N. D. Mermin, “Thermal properties of the inhomogeneous electron gas,” *Phys. Rev.*, vol. 137, no. 5A, p. A1441, 1965.
- [38] J.-P. Hansen and I. R. McDonald, *Theory of simple liquids: with applications to soft matter*. Academic Press, 2013.
- [39] G. W. Brindley, “Identification of clay minerals by x-ray diffraction analysis,” *Clays and Clay Minerals*, vol. 1, no. 1, pp. 119–129, 1952.
- [40] C. N. Likos, “Effective interactions in soft condensed matter physics,” *Phys. Rep.*, vol. 348, no. 4-5, pp. 267–439, 2001.



- [41] R. Roth, “Fundamental measure theory for hard-sphere mixtures: a review,” *J. Phys.: Condens. Matter*, vol. 22, no. 6, p. 063102, 2010.
- [42] Y. Rosenfeld, “Free-energy model for the inhomogeneous hard-sphere fluid mixture and density-functional theory of freezing,” *Phys. Rev. Lett.*, vol. 63, pp. 980–983, Aug 1989.
- [43] J. K. Percus, “Equilibrium state of a classical fluid of hard rods in an external field,” *J. Stat. Phys.*, vol. 15, pp. 505–511, Dec 1976.
- [44] J. K. Percus, “One-dimensional classical fluid with nearest-neighbor interaction in arbitrary external field,” *J. Stat. Phys.*, vol. 28, pp. 67–81, May 1982.
- [45] J. K. Percus, “Free energy models for nonuniform classical fluids,” *J. Stat. Phys.*, vol. 52, no. 5, pp. 1157–1178, 1988.
- [46] G. A. Mansoori, N. F. Carnahan, K. E. Starling, and T. W. Leland Jr, “Equilibrium thermodynamic properties of the mixture of hard spheres,” *J. Chem. Phys.*, vol. 54, no. 4, pp. 1523–1525, 1971.
- [47] R. Roth, R. Evans, A. Lang, and G. Kahl, “Fundamental measure theory for hard-sphere mixtures revisited: the White Bear version,” *J. Phys.: Condens. Matter*, vol. 14, pp. 12063–12078, nov 2002.
- [48] A. J. Archer, B. Chacko, and R. Evans, “The standard mean-field treatment of inter-particle attraction in classical DFT is better than one might expect,” *J. Chem. Phys.*, vol. 147, no. 3, p. 034501, 2017.
- [49] V. A. Parsegian, *Van der Waals forces: a handbook for biologists, chemists, engineers, and physicists*. Cambridge University Press, 2005.

- [50] D. E. Sullivan, “Van der Waals model of adsorption,” *Phys. Rev. B*, vol. 20, no. 10, p. 3991, 1979.
- [51] R. Evans, U. M. B. Marconi, and P. Tarazona, “Capillary condensation and adsorption in cylindrical and slit-like pores,” *J. Chem. Soc. Faraday Trans.*, vol. 82, no. 10, pp. 1763–1787, 1986.
- [52] A. A. Louis, E. Allahyarov, H. Löwen, and R. Roth, “Effective forces in colloidal mixtures: From depletion attraction to accumulation repulsion,” *Phys. Rev. E*, vol. 65, no. 6, p. 061407, 2002.
- [53] A. J. Archer and R. Evans, “Relationship between local molecular field theory and density functional theory for non-uniform liquids,” *J. Chem. Phys.*, vol. 138, no. 1, p. 014502, 2013.
- [54] D. W. Oxtoby, “Homogeneous nucleation: theory and experiment,” *J. Phys.: Condens. Matter*, vol. 4, pp. 7627–7650, sep 1992.
- [55] H. Yin, D. N. Sibley, U. Thiele, and A. J. Archer, “Films, layers, and droplets: The effect of near-wall fluid structure on spreading dynamics,” *Phys. Rev. E*, vol. 95, no. 2, p. 023104, 2017.
- [56] J. S. Rowlinson and B. Widom, *Molecular theory of capillarity*. Dover, 1982.
- [57] L. G. MacDowell, “Computer simulation of interface potentials: Towards a first principle description of complex interfaces,” *Eur. Phys. J. Special Topics*, vol. 197, no. 1, p. 131, 2011.
- [58] M. Rauscher and S. Dietrich, “Wetting phenomena in nanofluidics,” *Annu. Rev. Mater. Res.*, vol. 38, pp. 143–172, 2008.

- [59] B. V. Derjaguin and N. V. Churaev, “Structural component of disjoining pressure,” *J. Colloid Interf. Sci.*, vol. 49, p. 249, 1974.
- [60] A. J. Archer and R. Evans, “Nucleation of liquid droplets in a fluid with competing interactions,” *Mol. Phys.*, vol. 109, no. 23-24, pp. 2711–2722, 2011.
- [61] O. Buller, W. Tewes, A. J. Archer, A. Heuer, U. Thiele, and S. V. Gurevich, “Nudged elastic band calculation of the binding potential for liquids at interfaces,” *J. Chem. Phys.*, vol. 147, no. 2, p. 024701, 2017.
- [62] D. J. Benney, “Long waves on liquid films,” *J. Math. Phys.*, vol. 45, no. 2, p. 150, 1966.
- [63] A. Oron, S. H. Davis, and S. G. Bankoff, “Long-scale evolution of thin liquid films,” *Rev. Mod. Phys.*, vol. 69, no. 3, p. 931, 1997.
- [64] H. Schlichting and K. Gersten, *Boundary-layer theory*. Springer, 2016.
- [65] D. N. Sibley, N. Savva, and S. Kalliadasis, “Slip or not slip? A methodical examination of the interface formation model using two-dimensional droplet spreading on a horizontal planar substrate as a prototype system,” *Phys. Fluids*, vol. 24, no. 8, p. 082105, 2012.
- [66] P.-S. de Laplace and N. I. Bowditch, *Mecanique celeste*. from the Press of Isaac R. Butts, 1829.
- [67] D. J. Acheson, *Elementary fluid dynamics*. Oxford University Press, 1990.
- [68] J. L. Parker, P. M. Claesson, and P. Attard, “Bubbles, cavities, and the long-ranged attraction between hydrophobic surfaces,” *J. Phys. Chem.*, vol. 98, no. 34, pp. 8468–8480, 1994.

- [69] V. S. J. Craig, “Very small bubbles at surfaces the nanobubble puzzle,” *Soft Matter*, vol. 7, no. 1, pp. 40–48, 2011.
- [70] D. Lohse and X. Zhang, “Surface nanobubbles and nanodroplets,” *Rev. Mod. Phys.*, vol. 87, no. 3, p. 981, 2015.
- [71] M. Alheshibri, J. Qian, M. Jehannin, and V. S. J. Craig, “A history of nanobubbles,” *Langmuir*, vol. 32, no. 43, pp. 11086–11100, 2016.
- [72] S. Ljunggren and J. C. Eriksson, “The lifetime of a colloid-sized gas bubble in water and the cause of the hydrophobic attraction,” *Colloids Surf. A*, vol. 129, pp. 151–155, 1997.
- [73] H. Stevens, R. F. Considine, C. J. Drummond, R. A. Hayes, and P. Attard, “Effects of degassing on the long-range attractive force between hydrophobic surfaces in water,” *Langmuir*, vol. 21, no. 14, pp. 6399–6405, 2005.
- [74] A. C. Simonsen, P. L. Hansen, and B. Klösgen, “Nanobubbles give evidence of incomplete wetting at a hydrophobic interface,” *J. Colloid Interface Sci.*, vol. 273, no. 1, pp. 291–299, 2004.
- [75] M. A. Hampton and A. V. Nguyen, “Accumulation of dissolved gases at hydrophobic surfaces in water and sodium chloride solutions: Implications for coal flotation,” *Minerals Engineering*, vol. 22, no. 9, pp. 786–792, 2009.
- [76] W. F. Paxton, K. C. Kistler, C. C. Olmeda, A. Sen, S. K. St. Angelo, Y. Cao, T. E. Mallouk, P. E. Lammert, and V. H. Crespi, “Catalytic nanomotors: autonomous movement of striped nanorods,” *J. Am. Chem. Soc.*, vol. 126, no. 41, pp. 13424–13431, 2004.

- [77] S. M. Janib, A. S. Moses, and J. A. MacKay, “Imaging and drug delivery using theranostic nanoparticles,” *Adv. Drug Deliv. Rev.*, vol. 62, no. 11, pp. 1052–1063, 2010.
- [78] N. Tretyakov, M. Müller, D. Todorova, and U. Thiele, “Parameter passing between molecular dynamics and continuum models for droplets on solid substrates: The static case,” *J. Chem. Phys.*, vol. 138, no. 6, p. 064905, 2013.
- [79] J. Benet, P. Llombart, E. Sanz, and L. G. MacDowell, “Premelting-induced smoothening of the ice-vapor interface,” *Phys. Rev. Lett.*, vol. 117, no. 9, p. 096101, 2016.
- [80] K. Jain, K. S. Rane, and J. R. Errington, “Using isothermal-isobaric monte carlo simulation to study the wetting behavior of model systems,” *J. Chem. Phys.*, vol. 150, no. 8, p. 084110, 2019.
- [81] V. B. Svetovoy, I. Dević, J. H. Snoeijer, and D. Lohse, “Effect of disjoining pressure on surface nanobubbles,” *Langmuir*, vol. 32, no. 43, pp. 11188–11196, 2016.
- [82] X. H. Zhang, N. Maeda, and J. Hu, “Thermodynamic stability of interfacial gaseous states,” *J. Phys. Chem. B*, vol. 112, no. 44, pp. 13671–13675, 2008.
- [83] B. Chacko, R. Evans, and A. J. Archer, “Solvent fluctuations around solvophobic, solvophilic, and patchy nanostructures and the accompanying solvent mediated interactions,” *J. Chem. Phys.*, vol. 146, no. 12, p. 124703, 2017.
- [84] A. J. Archer and R. Evans, “Wetting in the binary Gaussian core model,” *J. Phys.: Condens. Matter*, vol. 14, no. 6, p. 1131, 2002.

- [85] S. N. Jamadagni, R. Godawat, and S. Garde, “Hydrophobicity of proteins and interfaces: Insights from density fluctuations,” *Annu. Rev. Chem. Biomol. Eng.*, vol. 2, p. 147, 2011.
- [86] M. Kanduc, A. Schlaich, E. Schneck, and R. R. Netz, “Water-mediated interactions between hydrophilic and hydrophobic surfaces,” *Langmuir*, vol. 32, no. 35, p. 8767, 2016.
- [87] R. Evans and M. C. Stewart, “The local compressibility of liquids near non-adsorbing substrates: a useful measure of solvophobicity and hydrophobicity?,” *J. Phys.: Condens. Matter*, vol. 27, no. 19, p. 194111, 2015.
- [88] R. Evans and N. B. Wilding, “Quantifying density fluctuations in water at a hydrophobic surface: evidence for critical drying,” *Phys. Rev. Lett.*, vol. 115, no. 1, p. 016103, 2015.
- [89] J. R. Henderson, “Statistical mechanics of the disjoining pressure of a planar film,” *Phys. Rev. E*, vol. 72, no. 5, p. 051602, 2005.
- [90] L. F. Shampine and M. W. Reichelt, “The MATLAB ODE Suite,” *SIAM J. Sci. Comput.*, vol. 18, no. 1, pp. 1–22, 1997.
- [91] M. C. Stewart and R. Evans, “Wetting and drying at a curved substrate: Long-ranged forces,” *Phys. Rev. E*, vol. 71, no. 1, p. 011602, 2005.
- [92] M. Dijkstra, J. M. Brader, and R. Evans, “Phase behaviour and structure of model colloid-polymer mixtures,” *J. Phys.: Condens. Matter*, vol. 11, no. 50, p. 10079, 1999.
- [93] Y. Sui, H. Ding, and P. D. M. Spelt, “Numerical simulations of flows with moving contact lines,” *Ann. Rev. Fluid Mech.*, vol. 46, pp. 97–119, 2014.

- [94] J. H. Snoeijer and B. Andreotti, “Moving contact lines: scales, regimes, and dynamical transitions,” *Ann. Rev. Fluid Mech.*, vol. 45, pp. 269–292, 2013.
- [95] E. B. Dussan, “On the spreading of liquids on solid surfaces: Static and dynamic contact lines,” *Ann. Rev. Fluid Mech.*, vol. 11, pp. 371–400, 1979.
- [96] J. M. Brader, R. Evans, and M. Schmidt, “Statistical mechanics of inhomogeneous model colloidpolymer mixtures,” *Mol. Phys.*, vol. 101, no. 23-24, pp. 3349–3384, 2003.
- [97] F. Heslot, N. Fraysse, and A. M. Cazabat, “Molecular layering in the spreading of wetting liquid drops,” *Nature*, vol. 338, pp. 640 – 642, 1989.
- [98] J. X. Yang, J. Koplik, and J. R. Banavar, “Terraced spreading of simple liquids on solid-surfaces,” *Phys. Rev. A*, vol. 46, pp. 7738–7749, 1992.
- [99] P. A. Kralchevsky and N. D. Denkov, “Analytical expression for the oscillatory structural surface force,” *Chem. Phys. Lett.*, vol. 240, pp. 385–392, 1995.
- [100] R. E. Isele-Holder and A. E. Ismail, “Requirements for the formation and shape of microscopic precursors in droplet spreading,” *Langmuir*, vol. 32, no. 18, pp. 4472–4478, 2016.
- [101] L. G. MacDowell and M. Müller, “Adsorption of polymers on a brush: Tuning the order of the wetting phase transition,” *J. Chem. Phys.*, vol. 124, no. 8, 2006.
- [102] L. G. MacDowell, “Computer simulation of interface potentials: Towards a first principle description of complex interfaces?,” *Eur. Phys. J. Special Topics*, vol. 197, no. 1, p. 131, 2011.

- [103] L. G. MacDowell, J. Benet, N. A. Katcho, and J. M. Palanco, “Disjoining pressure and the film-height-dependent surface tension of thin liquid films: New insight from capillary wave fluctuations,” *Adv. Colloid Interface Sci.*, vol. 206, pp. 150 – 171, 2014. Manuel G. Velarde.
- [104] E. M. Fernández, E. Chacón, L. G. MacDowell, and P. Tarazona, “Mesoscopic Hamiltonian for the fluctuations of adsorbed Lennard-Jones liquid films,” *Phys. Rev. E*, vol. 91, p. 062404, Jun 2015.
- [105] R. Evans, J. R. Henderson, D. C. Hoyle, A. O. Parry, and Z. A. Sabeur, “Asymptotic decay of liquid structure: oscillatory liquid-vapour density profiles and the Fisher-Widom line,” *Mol. Phys.*, vol. 80, no. 4, pp. 755–775, 1993.
- [106] R. Evans, R. J. F. L. de Carvalho, J. R. Henderson, and D. C. Hoyle, “Asymptotic decay of correlations in liquids and their mixtures,” *J. Chem. Phys.*, vol. 100, no. 1, pp. 591–603, 1994.
- [107] M. E. Fisher and B. Widom, “Decay of correlations in linear systems,” *J. Chem. Phys.*, vol. 50, no. 9, pp. 3756–3772, 1969.
- [108] V. S. Mitlin, “Dewetting of solid surface: Analogy with spinodal decomposition,” *J. Colloid Interface Sci.*, vol. 156, no. 2, pp. 491–497, 1993.
- [109] C. L. M. H. Navier, “Mémoire sur les lois du mouvement des fluides,” *Mémoires de l’Académie Royale des Sciences de l’Institut de France*, vol. 6, pp. 389–440, 1823.
- [110] A. Münch, B. A. Wagner, and T. P. Witelski, “Lubrication models with small to large slip lengths,” *J. Eng. Math.*, vol. 53, no. 3-4, pp. 359–383, 2005.



- [111] U. Thiele, M. G. Velarde, K. Neuffer, and Y. Pomeau, “Film rupture in the diffuse interface model coupled to hydrodynamics,” *Phys. Rev. E*, vol. 64, p. 031602, 2001.
- [112] D. N. Sibley, A. Nold, and S. Kalliadasis, “The asymptotics of the moving contact line: cracking an old nut,” *J. Fluid. Mech.*, vol. 764, pp. 445–462, 2015.
- [113] P. J. Haley and M. J. Miksis, “The effect of the contact line on droplet spreading,” *J. Fluid. Mech.*, vol. 223, pp. 57–81, 1991.
- [114] N. Savva and S. Kalliadasis, “Dynamics of moving contact lines: A comparison between slip and precursor film models,” *EPL*, vol. 94, no. 6, p. 64004, 2011.
- [115] D. N. Sibley, A. Nold, N. Savva, and S. Kalliadasis, “A comparison of slip, disjoining pressure, and interface formation models for contact line motion through asymptotic analysis of thin two-dimensional droplet spreading,” *J. Eng. Math.*, vol. 94, no. 1, pp. 19–41, 2015.
- [116] A. Yochelis and L. M. Pismen, “Droplet motion driven by surface freezing or melting: A mesoscopic hydrodynamic approach,” *Phys. Rev. E*, vol. 72, no. 2, p. 025301, 2005.
- [117] M. N. Popescu, G. Oshanin, S. Dietrich, and A. M. Cazabat, “Precursor films in wetting phenomena,” *J. Phys.: Condens. Matter*, vol. 24, no. 24, p. 243102, 2012.
- [118] C. Honisch, T.-S. Lin, A. Heuer, U. Thiele, and S. V. Gurevich, “Instabilities of layers of deposited molecules on chemically stripe patterned substrates: Ridges versus drops,” *Langmuir*, vol. 31, no. 38, pp. 10618–10631, 2015.
- [119] N. V. Churaev, “Contact angles and surface forces,” *Adv. Colloid Interface Sci.*, vol. 58, no. 2, pp. 87–118, 1995.

- [120] N. Savva and S. Kalliadasis, “Two-dimensional droplet spreading over topographical substrates,” *Phys. Fluids*, vol. 21, no. 9, p. 092102, 2009.
- [121] D. T. Wasan and A. D. Nikolov, “Spreading of nanofluids on solids,” *Nature*, vol. 423, pp. 156–159, 2003.
- [122] A. Chengara, A. D. Nikolov, D. T. Wasan, A. Trokhymchuk, and D. Henderson, “Spreading of nanofluids driven by the structural disjoining pressure gradient,” *J. Colloid Interface Sci.*, vol. 280, pp. 192–201, 2004.
- [123] O. K. Matar, R. V. Craster, and K. Sefiane, “Dynamic spreading of droplets containing nanoparticles,” *Phys. Rev. E*, vol. 76, no. 5, p. 056315, 2007.
- [124] G.-H. Hu, “Influences of oscillatory structural forces on dewetting of nanoparticle-laden ultra-thin films,” *Acta Mech. Sin.*, vol. 28, no. 3, pp. 737–745, 2012.
- [125] U. Thiele, A. J. Archer, and M. Plapp, “Thermodynamically consistent description of the hydrodynamics of free surfaces covered by insoluble surfactants of high concentration,” *Phys. Fluids*, vol. 24, p. 102107, 2012.
- [126] U. Thiele, D. V. Todorova, and H. Lopez, “Gradient dynamics description for films of mixtures and suspensions: Dewetting triggered by coupled film height and concentration fluctuations,” *Phys. Rev. Lett.*, vol. 111, p. 117801, 2013.
- [127] U. Thiele, A. J. Archer, and L. M. Pismen, “Gradient dynamics models for liquid films with soluble surfactant,” *Phys. Rev. Fluids*, 2016. (at press).
- [128] L. H. Tanner, “The spreading of silicone oil drops on horizontal surfaces,” *J. Phys. D: Appl. Phys.*, vol. 12, no. 9, p. 1473, 1979.

- [129] S. Engelnkemper, M. Wilczek, S. V. Gurevich, and U. Thiele, “Morphological transitions of sliding drops - dynamics and bifurcations,” *Phys. Rev. Fluids*, vol. 1, p. 073901, 2016.